COMPUTATIONAL INVESTIGATIONS ON THE AERODYNAMICS OF A GENERIC CAR MODEL IN PROXIMITY TO A SIDE WALL

by

Srivatsa Mallapragada

A thesis submitted to the faculty of
The University of North Carolina at Charlotte
in partial fulfillment of the requirements
for the degree of Master of Science in
Mechanical Engineering

Charlotte

2017

Approved by:

_____
Dr. Mesbah Uddin

_____
Dr. Saiful Bari

_____
Dr. Christopher Vermillion

ABSTRACT

SRIVATSA MALLAPRAGADA. Computational investigations on the aerodynamics of a generic car model in proximity to a side wall. (Under the direction of DR. MESBAH UDDIN)

A moving road vehicle is subjected to many fluid interferences caused by a number of external agents apart from the vehicle itself. Vehicles moving in proximity to a side wall is an interesting aspect that has been little investigated in the literature. This is of great interest in motorsports, more specifically in NASCAR racing. The aim of this thesis is to develop a Computational Fluid Dynamics (CFD) model that can simulate the motion of a race car moving close to a side wall with an objective of understanding the influence of this side barrier on the overall aerodynamic characteristics of the vehicle, like the force and moment coefficients. Additionally, flow visualization tools are used to gain insights into the flow field and to explain the causes of the observed aerodynamic characteristics of the vehicle. This is accomplished by using a generic car model, a 25° slant angle Ahmed Body, in proximity to a side wall in a virtual wind tunnel where the vehicle body is allowed to move at constant velocity. This methodology is different from the traditional CFD approach where the air is blown over a stationary vehicle. The simulation process used in this thesis requires the use of a recently developed meshing methodology called the Overset mesh. All simulations were run using a commercial finite volume CFD code called StarCCM+ where the Unsteady Reynolds Averaged Navier-Stokes URANS fluid flow solver was used to model turbulence. However, the existing literature suggests that no URANS model can correctly predict the flow field around a 25-degree slant Ahmed body model; all models under-predict turbulence in the initial separated shear layer and over-predict the separation region. Subsequently, the first phase of this thesis involved the determination of a modeling methodology that can accurately predict the flow-field over a 25-degree Ahmed body. Two two-equation eddy-viscosity turbulence models, the

AKN and SST preferred by many researchers for CFD simulations of massively separated flows, were tested. It turned out that only the latter with modified model coefficients was capable of reproducing the experimental results with a reasonable accuracy. Compared to the eddy viscosity CFD simulations of an isolated 25-degree slant angle Ahmed body seen in existing literature, the results presented in this thesis show significantly better correlations with experiments. The wall proximity studies show a strong influence of the presence of the wall on the overall aerodynamic characteristics of the vehicle body. When compared with the experimental studies, although both show similar trends, however, there exists a significant difference between the experimental and CFD predicted results which tend to worsen as one approaches the wall. These differences can be attributed to fact that the CFD emulation of the flow around the side-wall is more realistic compared to the experimental implementation.

DEDICATION

I would like to dedicate this thesis to my Parents, brother and my fiance for their support throughout this process

ACKNOWLEDGEMENTS

I would like to express my gratitude by thanking my advisor, Dr. Mesbah Uddin, for his constructive criticism and thoughtful insights about my way of approach and my capabilities which allowed me to know my restrictions and reach the final point in this thesis. I would also like to thank Dr. Saiful Bari and Dr. Christopher Vermillion for taking time to review my thesis and provide me their perceptions to make it better. I'm grateful to my colleagues at this research laboratory, specially Brett Peters, Chen fu, Adit Misar and Chunhui Zhang who aided me in understanding the usage of overset mesh during the initial stages of this thesis. Ultimately, I would like to thank the Mechanical Engineering department of UNCC, and the College of Engineering as a whole for the immense support and accepting me to use their resources of Sidewinder HPC to finish my research.

TABLE OF CONTENTS

LIST OF FIGURES

LIST OF TABLES

CHAPTER 1: INTRODUCTION

1.1 Strength of CFD

Vehicle Aerodynamics gives a deep insight into the performance and problems of the cars with respect to the shape of the vehicle. Experimental procedures result in more accurate predictions but experimentally emulating every situation in a race is costly and sometimes impossible to implement. Moreover, the reason for certain observations is unexplained as three-dimensional non-invasive measurements of most of the aerodynamic parameters are beyond the capability of the state of the art experiential techniques. Computational Fluid Dynamics (CFD) tools have emerged as an affordable and reliable complementary. Intricate geometries, complicated flow structures, and subtle fluid motions can be analyzed using CFD. It plays a vital role from designing a race car with least drag and highest performance to understanding the behavior of a minuscule particle in a fluid when excited.

Aerodynamic research using CFD evolved through 5 decades with an aspect of investigating the turbulence and vortex structures in it. Since then major changes took place in research capabilities of CFD involving fluid flow around a simple bluff body to a most detailed and intricate geometry. Recent developments in computing power aids in analyzing the interaction of multiple objects in a fluid flow. Apart from the race teams, automotive manufacturers are using this as a powerful tool in designing the exterior body of cars.

1.2 Motivation

A vehicle which is involved in racing or maneuvering on roads has a possibility that it might be in a scenario where it needs to move along a side wall. This case

is special in racing as it will destabilize a moving vehicle which is in close proximity to a side wall and such incidents occurred many times in National Association of Stock Car Racing (NASCAR) races. The race vehicle that is in close proximity to a side wall loose its traction in rear wheels and starts to wiggle which is said loose tire in race terminology. This phenomenon is seen in many racing events as the cars tend to move along the side wall. Further investigation was done on this aspect from the literature involving vehicles moving in close proximity to a side wall with various velocities and wall separation distances. The studies on this aspect were very old and less in number, out of which a simplified car body was used to identify this phenomenon using an experimental procedure accompanied with a CFD analysis. This study showed that the force and moment coefficients vary in a regular pattern as the wall separation distance decreases, but beyond a minimum point of separation they tend to diverge asymptotically. This caught the interest of the present author in finding a reason for this peculiarity as the previous studies did not state a clear reason for it. Additionally, the vehicle in the original experiment was not moved in relative to the wall to know the accurate behavior of the flow and the forces acting on the vehicle. This information was taken as an initiative for the present study and the same simplified body is used to replicate the experiment. Later, the body is made to move using a sliding mesh technique called as the "Overset Mesh or Chimera Mesh grid". This was done to understand the flow behavior and measurement of forces more accurately than a stationary vehicle with the wind blowing on it. This allows imitating the real life incident where the vehicle is in moving condition relative to the side wall and the surrounding environment.

1.3 Objectives of the Study

To proceed with the above discussed approach of CFD investigation, few objectives are to be duly mentioned before going into further details. While understanding the effect of wall interference with the fluid flow in this study:

- The fluid turbulent behavior and boundary layer separation on the body is to be observed as they are vital in accurate predictions of aerodynamic interest.

- Transverse and longitudinal vortices along the body are to be observed.

- Force and moment coefficients of the body are to be measured and Pressure fluctuations over the rear slant are to be observed.

- Effect of Wake distortion and characteristics of downwash on the body and along the side wall are to be analyzed.

- Peculiarities in the aerodynamic parameters are to be observed and root cause is to be analyzed.

This thesis is developed based on the afore mentioned objectives. Every finding and observation is compared with available experimental results for sanity check. Root cause analysis for certain eccentricities were briefed.

1.4 Organization of Thesis

Chapter 1 notifies a few details of aerodynamics in racing and automotive industry and motivation of this thesis.

Chapter 2 feeds the background of vehicle in close proximity of a side wall and gives a brief introduction of Ahmed body and the choice of it in this thesis.

Chapter 3 provides an insight into the problem of inaccurate prediction of flow over 25° slant angle Ahmed body model by the RANS turbulence models and its remedy. It discusses geometry details, mesh settings, physics setup for the simulations.

Chapter 4 accounts the post processing data and highlights the peculiarities in the flow structure at various separation points of the vehicle to the side wall.

Chapter 5 projects the conclusions made in the previous chapter and discusses the scope of further analysis in this study.

CHAPTER 2: OVERVIEW OF WALL PROXIMITY STUDIES

2.1 Ahmed Bluff Body Model

CFD analysis of flow around simplified vehicle bluff bodies has been a popular and enthusiastic source of study for predominant researchers around the globe. One interesting model which is being used as a resemblance of an automotive ground vehicle is Ahmed model introduced by Ahmed et al. [1] Ahmed body contains primary shape characteristics of a regular ground vehicle to analyze various aerodynamic flow parameters emerged from fluid and body interference. The simplified geometry of Ahmed body is the primary reason to choose for this thesis with the consideration of economical usage of computing power during the simulation. Although the model is a bluff body, it contains a slant angle on the rear end which generates necessary flow phenomenon similar to a real car model. For a moving ground vehicle, the primary contribution of the Total drag is the Pressure drag which occurs from the wake and the reattached flow over the slant angle and this was focused on the model. Considering the above the qualities, a primary step for the wall proximity studies is made with this model. Additionally, an experimental analysis is found in the literature to support the present study.

2.2 A Few Experiments on Ahmed Body

Ahmed et al. conducted experiments on Ahmed body with stilts in a wind tunnel containing a stationary ground to analyze the outcomes of changing the rear slant angle (φ) within a range of 0 to 40 degrees. They found that almost 85% of the drag obtained from the rear end of the body is in the form of pressure drag. Various types of vortices were observed along the body line and on the surface. The most dominant

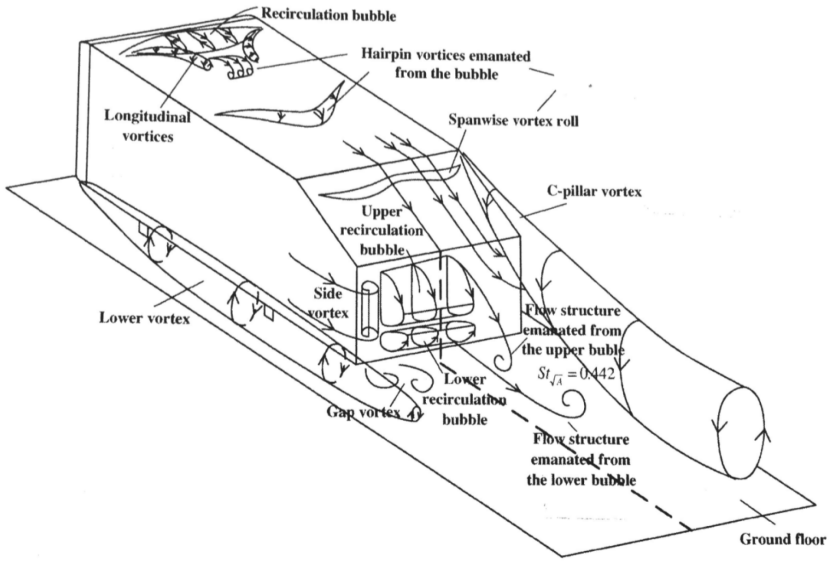

Figure 2.1: Schematic Diagram of Ahmed Body [2]

vortices are horseshoe vortices occurred on the upper surface. Vortex shedding from the body edges, the recirculation zone within the wake and the reattaching flows on the body are the primary contributors of drag to the total vehicle drag as afore mentioned and a schematic of this is shown in Figure 2.1. Moreover, these flow complications are very difficult to predict by using eddy viscosity turbulence model based CFD simulations. For specific slant angles, it is always a debatable aspect between the turbulence models in their prediction capabilities.

A plot of the drag coefficients associated with various slant angles is shown in Figure 2.2. The pressure and force measurements were collected by connecting the model to a strain gauge below the ground. As the rear slant angle was increased from 0 to 40 degrees, a critical angle of 30 degrees was spotted with an instant increase of drag coefficient to a maximum of 0.378 before the flow separation at the rear slant and later the C_{D} dropped to 0.260. Although the high drag value was observed from the original body with no adjustments, the low drag was obtained by fixing a splitter plate vertically on the symmetry plane 25 mm behind the model which aided flow separation. The point of discussion was only confined to drag coefficients

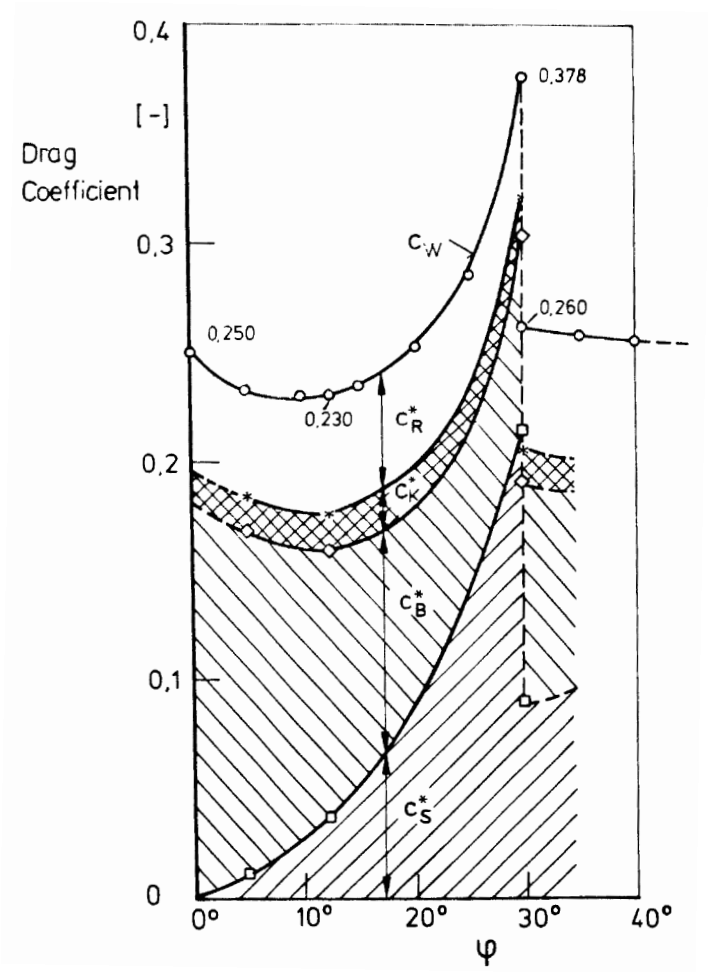

Figure 2.2: C_D Distribution Plot for Original Ahmed Body Experiment[1]

in the initial experiments but later discussions by various authors involved the lift coefficients in understanding the flow characteristics in a better way. Soon after the original experiment was performed, several investigations were conducted in CFD and within the wind tunnel to understand and ascertain the experiments done.

Graysmith et al. [3] performed a similar experiment as Ahmed et al. but with a moving ground and showed a prediction on lift coefficient which was accepted by many and was taken as primary lift value for further investigations. The interesting configurations of the model that are used for most studies were the critical angle ($\varphi =$ 30), sub-critical angle ($\varphi =$25) and super-critical angle ($\varphi = 35$) modifications of rear slant. These modifications in rear slant angles produce an adverse pressure gradient at the start of the rear slant and the sides of it. As a result, the turbulent kinetic energy in the flow gets energized and creates a complex flow pattern. This aids in creating a high or low value at the critical angle, flow separation and reattachment over the rear slant at the sub-critical angle and complete flow separation at the super-critical angle. Most turbulence models struggle to analyze the flow pattern of sub-critical angle configuration as the reattachment of flow is extremely tough to predict and this model is the point of interest further down the line of this thesis.

A few important studies were to be discussed at this point which are well acclaimed and accepted investigations from the literature. Lienhart & Becker [4, 5, 6] performed experimental procedures on Ahmed body (with stilts) model and projected the flow patterns very clearly but didn't comment on the drag values.They had conducted Laser Doppler Anemometry (LDA), Particle Image Velocimetry (PIV) and Hot Wire Anemometer experiments in a stationary ground wind tunnel on the sub and super critical angle models. The Reynolds number was comparable to the experiment conducted by Ahmed et al. and they argued that it would not considerably affect the flow physics of the problem, but the bulk flow velocity did not match the original experiment.

Bayraktar et al.[7] performed experimental and CFD investigations on a full-scale Ahmed body (with stilts) model at various slant angles and at various yaw angles. They had used a stationary ground wind tunnel for his experiments. Although he had conducted all the experiments on a wide range of Reynolds numbers, he used a mathematical equation consisting the drag values of a model with various yaw angles to find the wind averaged drag. His drag and lift values were comparable with his experimental results and previous studies and he gave a brief insight of the vortex shedding and asymmetry of the flow around the body.

Strachan et al.[8] conducted an LDA experiment in a moving ground wind tunnel with a wide range of slant angle models. Even though they had used an Ahmed body without stilts model, an aerodynamic strut from the roof of the wind tunnel was added to the body which slightly reduced the advantage. They ran the experiments at a higher Reynolds number of 1.7×10^6 to avoid Reynolds number effects, but the strut added some amount of drag to the body which the authors neglected to discuss. They have stated that the strut caused some discrepancies to the flow and aided to burst the recirculation bubble emerging from the top edge of the rear slant. This caused the experiments to yield a high C_D value at a lower slant angle configuration, unlike the original experiment. However, they have discussed only the sub-critical angle configuration stating that the strut created a lesser disturbance to the flow at the rear slant, unlike the other investigated configurations. The flow visualizations and velocity profiles were compared to the results of Lienhart et al.[4, 5, 6] LDA experiments and showed a similarity between the velocity profiles.

2.3 Vital CFD Procedures on Ahmed Body

Krajnovic and Davidson[9] conducted a CFD study with Large Eddy Simulation (LES) of flow around an Ahmed body (without stilts) model. They had investigated drag and other flow parameters and showed that the physics model predicts the values accurately, with a lowest possible mesh size, up to a Kolmogorov length scale.

They confirmed that their choice of physics model is accurate in predicting the drag value for this model, but they are unsure about the physics model suitability for other complex geometries. However, Krajnovic and Davidson neglected the Reynolds number dependence with a convenient explanation.

Later, Mingeuz et al.[10] conducted a Large Eddy Simulation with Spectral Vanishing Viscosity Technique (SVV-LES). He specified that the solver is capable of predicting the flow separation and dynamic behavior of the release vortex wake very effectively and so he studied the flow pattern, production, and development of vortices and wake formation with Ahmed body. He understood that SVV-LES solver with near wall treatment accurately predicts the flow and the dynamics of vortices but the drag values were over predicted. The wake of the Ahmed body contains intricate flow patterns which are computationally expensive to predict accurately. So, Kapadia et al.[11] conducted Detached-Eddy Simulations with Spalart Almaras near wall treatment (DES-Spalart Almaras) on sub critical and critical slant angle models of Ahmed body with stilts using the commercial solver Cobalt. They have understood that the average drag value of the body is close to the experimental value, but the drag distribution values were over-predicted at the rear of the body and under-predicted at the front. This was due to the DES–Spalart Almaras model weakening the boundary layer of the flow around the body and allowing an early flow separation causing the discrepancy of the drag coefficient value. Subsequently, it was weakening the vortices in the wake of the body for the 25° slant angle case.

The characteristics of the flow around Ahmed Body were further explored by Serre et al.[12] using DES and LES models for their CFD simulations. In their investigation, the LES method agreed with the experimental results at low Reynolds numbers but couldn't cope up with higher Reynolds numbers due to an unresolved boundary layer over the top of the Ahmed body. The experimental C_{D} value was 0.298 but the LES predicted values were in a range of 0.317 to 0.431 at the chosen Reynolds number of

7.68×10^5.

In considering the studies made on Ahmed body with the LES and DES turbulence models, it is understood that a finer grid is needed to resolve the discrepancies created during the wake predictions and predictions of aerodynamic coefficients by LES models. But expensive computational power is inevitable with the LES simulations.On the flip side, DES simulations can bargain with computational power but cannot attain the accuracy of LES in predicting the aerodynamic coefficients, wake, and vortex developments.

Guilmineau[13] investigated the flow around the Ahmed body using Reynolds Averaged Navier–Stokes (RANS) equations, and a range of eddy viscosity based turbulence models. He couldn't match the drag coefficient value to the available experimental results and stated this as a result of separated flow not reattaching to the slope of the rear slant angle. However, the simulations for the 35° slant angle matched extremely well with the experimental values and showed that RANS model can depict the flow in the wake appropriately and so it can be used as a powerful tool for flow visualizations.

2.4 Wall Proximity Studies

Understanding Ahmed body aerodynamic characteristics without the interference of adjacent objects give out the insights of the flow effected by the body and it is absolutely possible in experimentation and computer simulations. However, the real life incidents are to be considered for the further enlightenment when using these type of models and hence imitating the tangible situations on road and in racing are of great advantage. Such situations aid in designing a model which is suitable in various on road conditions. One scenario was found to be of a great interest which leads to a further research on race cars in close proximity to a side wall. As to the best of author's knowledge, much literature isn't available in this case but a few interesting investigations are discussed further in this thesis.

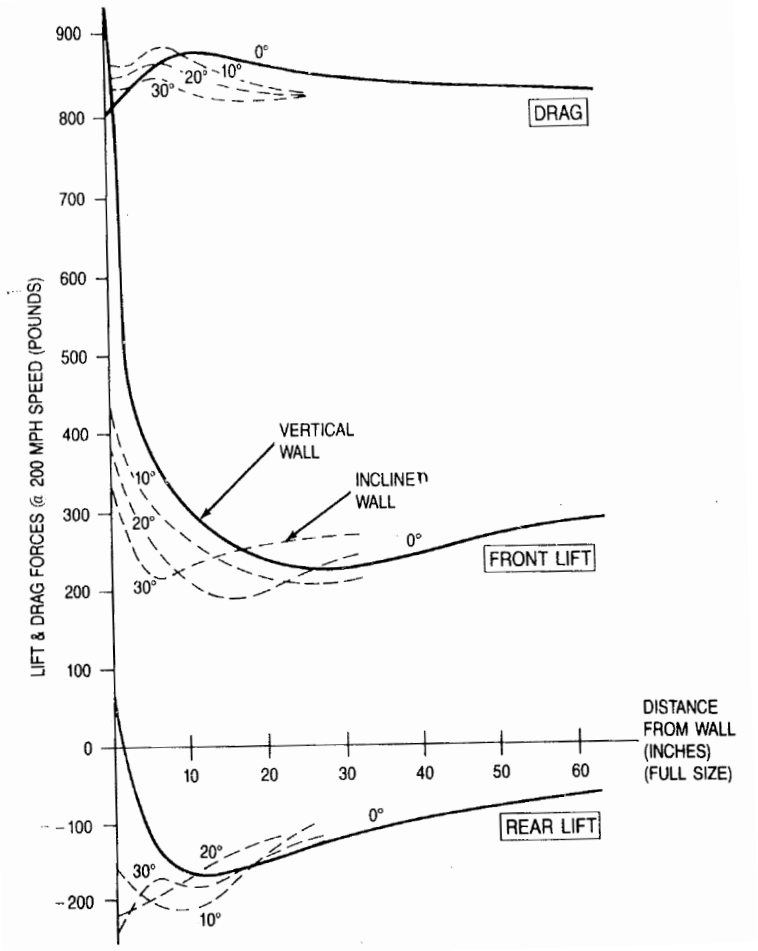

Figure 2.3: Effect of Wall Interference on Vehicle Lift and Drag[14]

Wallis and Quinlan [14] in 1988 conducted experiments on a 3/8 scale generic NASCAR model in the proximity of a 1.37 m height side wall. The entire experiment was conducted in a closed section wind tunnel with no moving ground and no boundary layer control over the ground and side wall. In Figure 2.3, a peculiar pattern of the drag and lift forces of the car is observed with decreasing wall separation distance and these patterns were later shown by Brown [15] in his thesis. The drag force with decreasing wall separation distance shows a particular trend till it reaches a maximum value and beyond a specific wall separation distance it drops asymptotically. A similar behavior is observed in front lift force, it falls to a minimum value before rising almost exponentially as the wall separation tends to zero. The rear lift force shows a similar trend as front lift force where there is a gradual decrease in value before the rapid rise. Figure 2.4 shows the effect of yaw angle over the vehicle drag and lift, but the primary observation is that the positive yaw of the vehicle induces low lift and high drag forces over the vehicle. This yaw data cannot be compared with any other authors' data as none had yawed the model in their investigation.

A CFD study was made by Advantage CFD [16] in 2001 with only one configuration of wall separation distance from the model and the separation distance is $1/4^{\text{th}}$ of the car's overall width. The car was $1/4^{\text{th}}$ of original NASCAR length and the side wall is 1.28m ($0.27L$) height. This data was compared with the results obtained by simulating an isolated model. The change in the static pressure on the near wall side of the car is shown in Figure 2.5. Apart from the pressure scenes, there was no quantitative data presented but they stated that the overall drag and downforce had a slight increase. They also stated that front end lift was increased when compared with isolated case, but the rear end lift was decreased when compared with the isolated case. The separation between the car and wall was close enough that the simulation showed that there was an attracting force acting on the model towards the wall creating a Yaw moment. This is evidently understood from the Figure 2.5 that

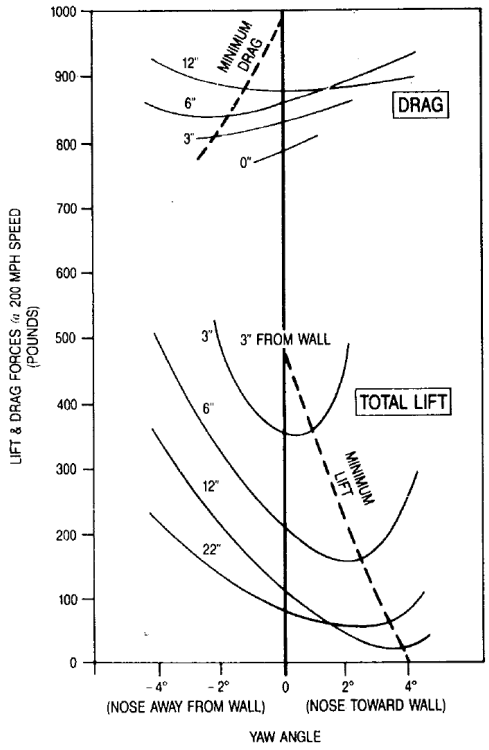

Figure 2.4: Effect of Wall proximity and vehicle Yaw angle on Vehicle Lift and Drag[14]

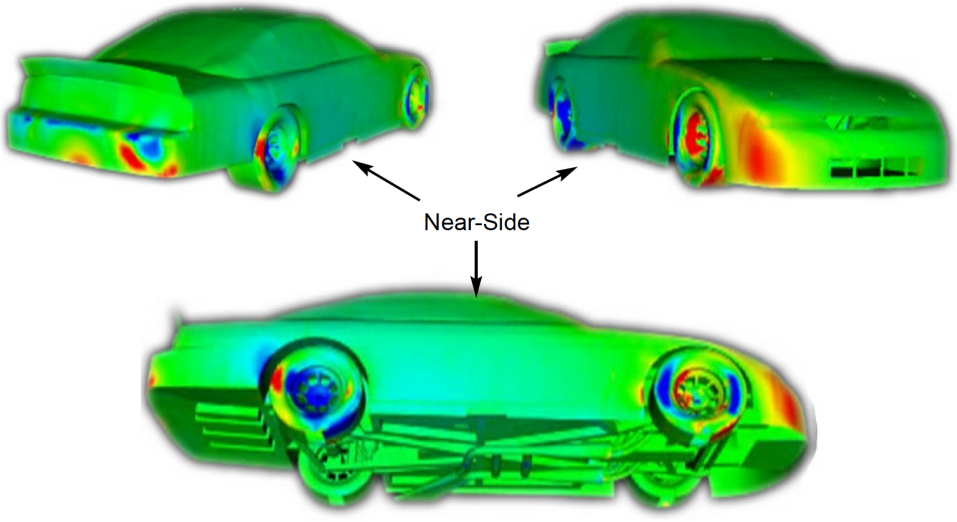

Figure 2.5: Δ C_P scalar scene of an isolated and wall proximity NASCAR. Yellow and red refer to a rise in ΔC_P, blue to fall in ΔC_P and green is no change in ΔC_P [16]

there is a pressure drop on the near wall side. This data, when compared with Wallis et al. [14], we can understand that the near wall case at $Z_{\mathrm{W}}/L = 0.1$ shows an increase in rear downforce, decrease in front downforce, and a slight increase in overall drag. The front end lift was predicted in the simulation while the experiments predicted the drop. However, the increase in rear end downforce and rise in overall drag were true in computational and experimental studies. Although few predictions were true, accounting the discrepancies from the CFD study when compared with the experimental study, this data is not much of a use for further investigations.

Brown[15] experimented on a Type C race car model, the schematic diagram can be seen in Figure 2.6, for the close wall proximity studies in a closed section wind tunnel. The model is a simplified geometry of a race car with a front splitter plate, rear wing and underbody diffuser contributing a significant downforce. There was no boundary layer control on the side wall but it was present for the rolling road of the wind tunnel as a part of the ground simulation. A suction at the upstream of the rolling road leading edge was used to remove the tunnel boundary layer. The experiment was accomplished after conducting the tests on the model with a combination of a range of side wall separations distances ($Z_{\mathrm{w}} = 0.14L$ to $Z_{\mathrm{w}} = 0.01L$), a range of ride heights and various rear wing angles of attack with a range of Reynolds numbers. The author has contributed a decent analysis about the Lift coefficient, Pressure coefficient, and other Force coefficient patterns and all show a similar trend as the wall separation between the model and the side wall decreases. Although the author experimented with various rear wing angles along with other configurations, they didn't have a significant effect on the results. Nevertheless, the 2° rear wing angle showed a considerable rise in results when compared with a 0-degree rear wing angle.

Figure 2.7(a) shows a rapid increase in Front Lift Coefficient (C_{Lf}) as the wall separation falls below a certain point. This rapid increase can be observed in all cases

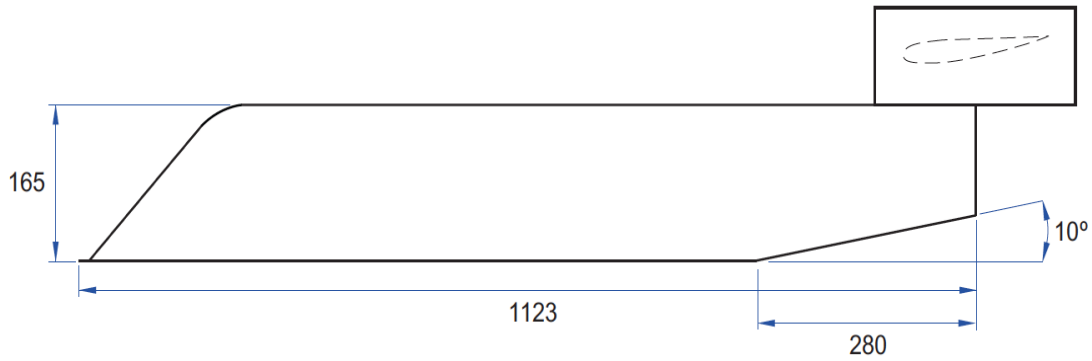

Figure 2.6: Type C Race Car Model (dimensions in mm)[15]

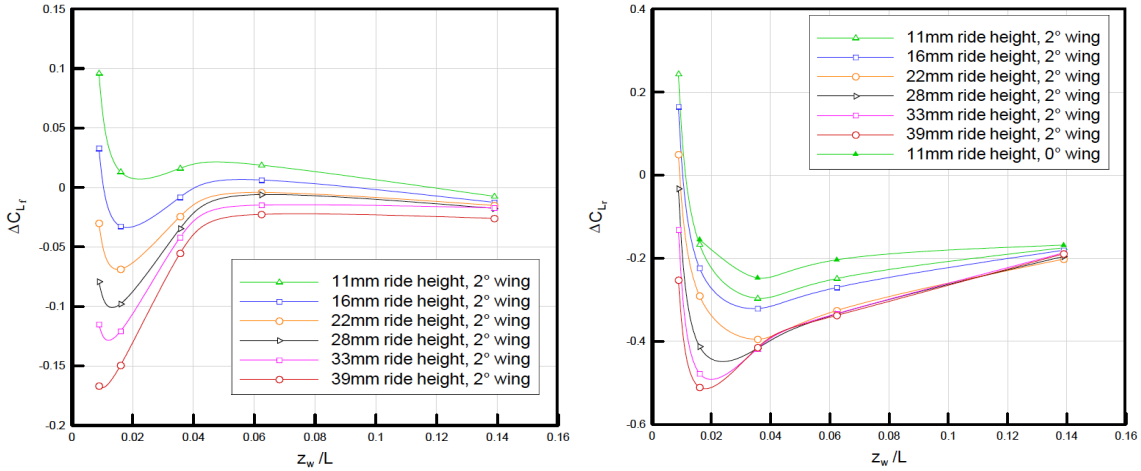

(a) (b)

Figure 2.7: a)Change in Front C_L vs Wall Separation from Brown's[15] data b)Change in Rear C_L vs Wall Separation from Brown's[15] Data

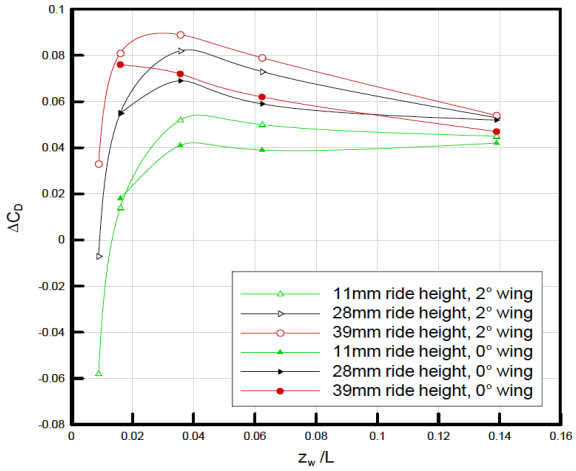

Figure 2.8: Change in C_D with wall separation[15]

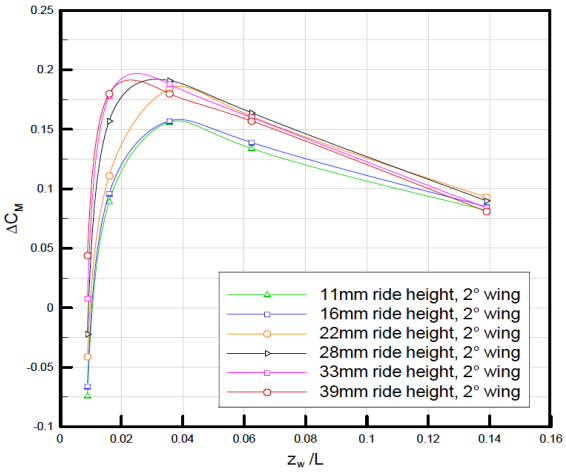

Figure 2.9: Change in Pitching Moment with wall separation[15]

except the 39mm ride height. This trend in values is similar in Rear Lift Coefficient (C_{Lr}) plot in Figure 2.7(b) and the 39 mm ride height also shows the same pattern as others. In Figure 2.8, the C_{D} plot shows a similar pattern as other plots and the 39mm ride height case shows a rise in the maximum value at minimum separation distance unlike the other cases. Figure 2.9 plots the change in pitching moment with wall distance and this is similar to C_{Lr} plot where the value of C_{M} falls down after a specific wall separation distance after a considerable rise in the value with the decreasing wall separation. In Figure 2.10 the side force increases till a specific point of wall separation distance is reached and then it decreases similar to the other plots but the 39mm ride height values are lower that 33mm ride height. The reason for the eccentric behavior of all the force and moment coefficients beyond a specific wall separation distance was not clearly described by the author. However, he described the affect of 39mm ride height on the coefficients as the effect of development of a vortex from the front splitter plate at those ride heights. The yawing moment coefficient plot in Figure 2.11 shows that the value at the eccentric point is lowest and from the side force coefficient plot it is understood that the side force is highest at this same point. Beyond this point, the separation is further decreased and the yawing moment is highest which means the nose of the body is pulled towards the wall and the point is the safest point to keep the vehicle in a stable condition. The author didn't discuss the cause of this eccentricity in detail but stated that there is a strong vortex causing this effect.

Another computational and experimental investigation was performed by Strachan et al. [17] with Ahmed body which is the motivational article for this thesis. They started their experimentation on Ahmed body in the proximity of a wall using an LDA setup which is visible in the Figure 2.12. The experimentation was performed in an open jet closed return wind tunnel attached with two component Laser Doppler anemometer and time averaged measurements were made. Initial experiments on

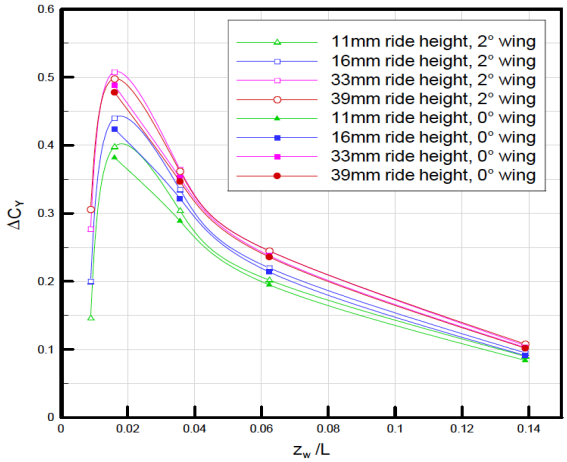

Figure 2.10: Change in Side Force with wall separation[15]

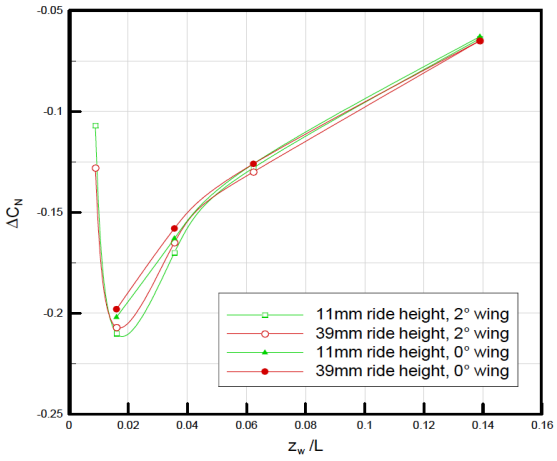

Figure 2.11: Change in Yawing Moment with wall separation[15]

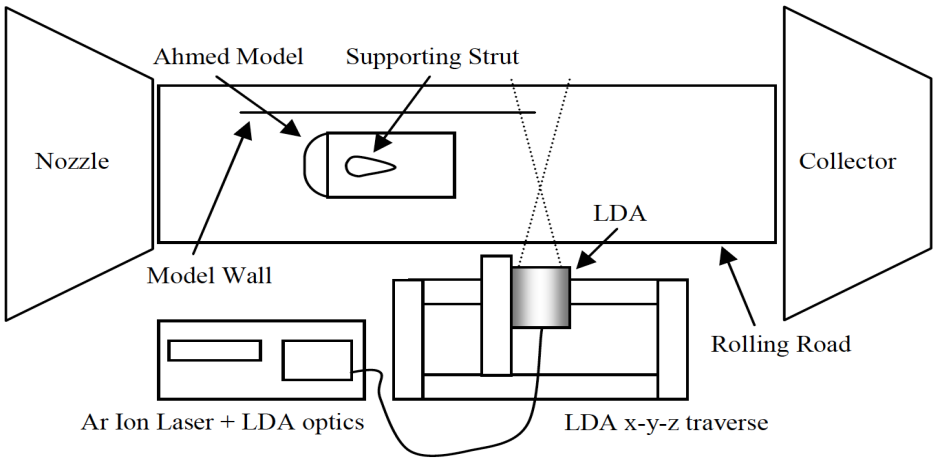

Figure 2.12: Schematic Diagram of Wall Proximity Experiment conducted with LDA Setup [17]

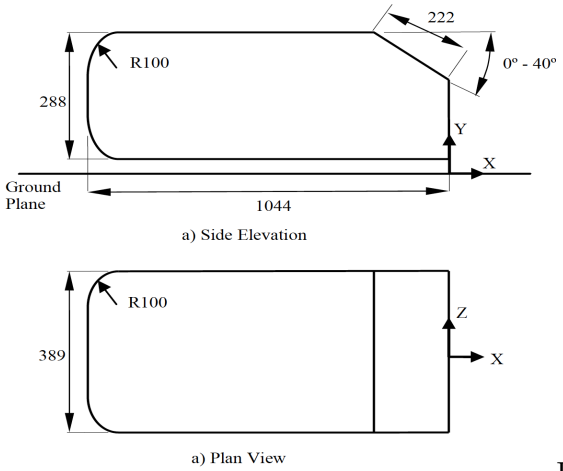

Figure 2.13: Axis format used by Strachan to represent his work[17]

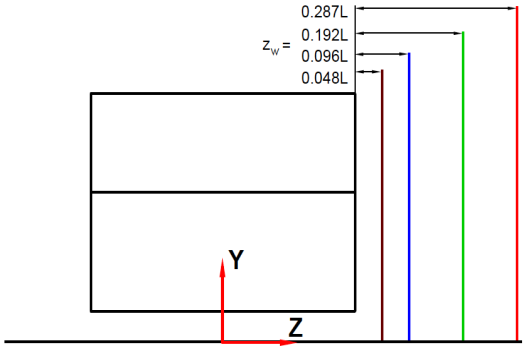

Figure 2.14: Wall Separations used by Strachan for Experimentation[17]

isolated Ahmed body case were performed with variation in rear slant angles ranging from 0 to 40 degrees with 5 degrees difference between each case. However, they had considered only 10, 40 and 25 degrees angles for wall proximity experiments and the results of (φ=25°) were highlighted than the other two. The side wall is used as a perspex wall to project the laser beam back to the anemometer. The experimental results were compared with CFD analysis of the same issue using $k-\epsilon$ RNG model and Reynolds Stress models. The authors had discussed on the change in the force coefficients and Pressure coefficients experienced by the model which was later compared with Brown's[15] Type C race car model. They emphasized more on the vortex structure change and change in pressure coefficient on the front face near to the wall and on the rear slant of the body. During the course of experimentation, he had observed that the velocity of the flow slightly increased as the wall separation decreased but the pressure changes are noticeable.

In Figures 2.15(a) and (b), change in C_{P} were well depicted on the front face and for a better understanding these changes were visually represented in Figures 2.16(a),(b) and (c) using CFD as a tool. A similar trend was observed on the rear slant of the Ahmed body where the change in pressure is highest on the near side

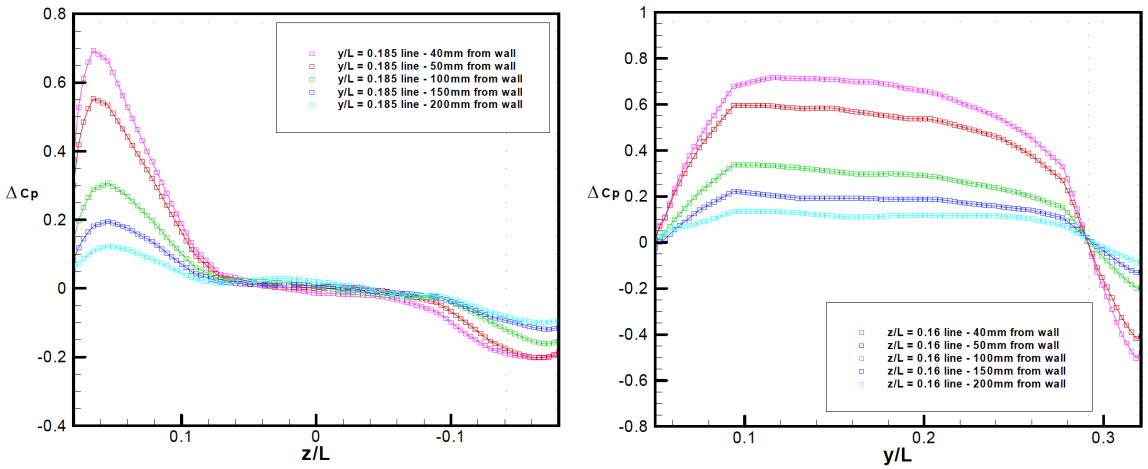

(a) $Y/L = 0.185$ (0.193m) (b) $Z/L = 0.16$ (0.167m)

Figure 2.15: Change in C_P at two locations with wall separations from Strachan's Experiment

of rear slant when the wall separation is at its minimum and the authors had used CFD to represent the change. In Figures 2.17(a) and (b), the change in C_{P} is clearly shown and by this it is understood that the lift generated at the near side of the body is higher than the off side causing a rolling moment. The longitudinal vortex that is generated from the near side of the rear slant is restricted by the wall and has weaker strength than the off side vortex. Apart these observations, the change in drag and lift coefficients are significant and followed the same trend as of the other authors' analysis from the literature. In Figure 2.24, the Change in C_{L} shows the pattern of the lift shown in Figure 2.9 which was the initial analysis of Wallis et al.[14] and the change in C_{D} value seems to be in good agreement with the previous studies. However, the side force, Pitching moment, Rolling moment and Yawing moment forces were all following a similar trend as shown by Brown. For further details, the author's thesis [18] contains an elaborated discussion on these patterns and flow visualizations which give some more insight on the topic. Although the author presented a detailed analysis of the phenomenon, he neglected the cause of the sudden rise in the values after a separation point like the previous studies in the literature. This analysis and

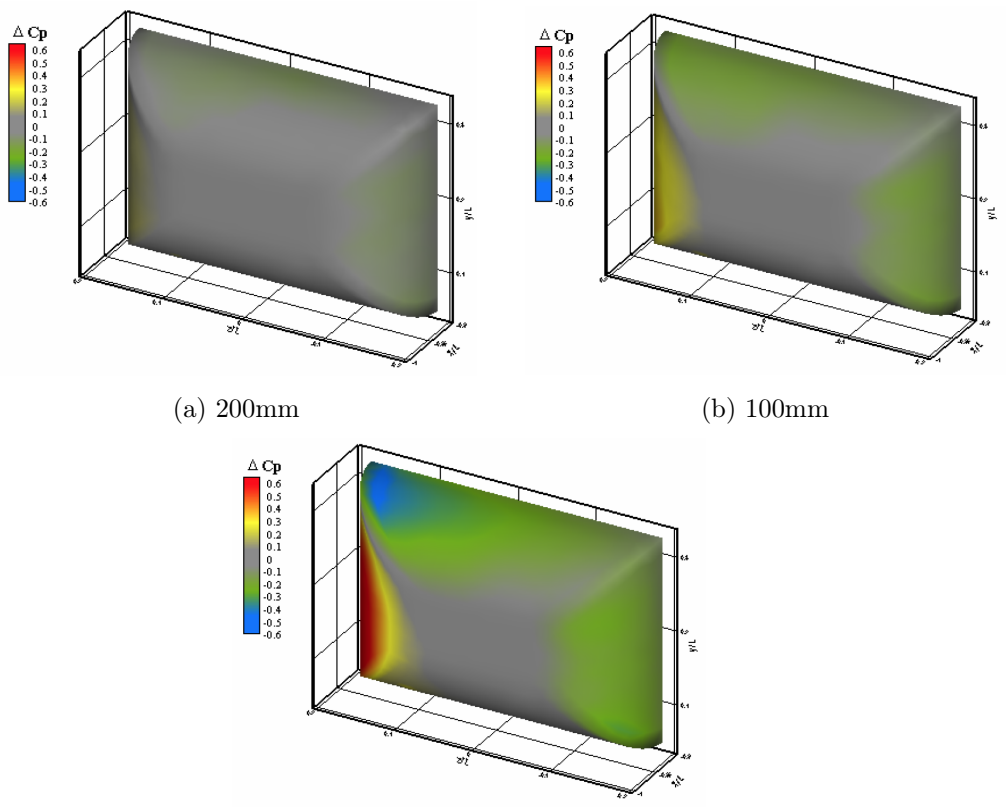

(a) 200mm

(b) 100mm

(c) 40mm

Figure 2.16: Scalar Scenes of Change in C_P on the Face at three Wall Separation Distances from Strachan's CFD data[17]

reason for the anomaly are discussed in this thesis with few more details and flow visualizations.

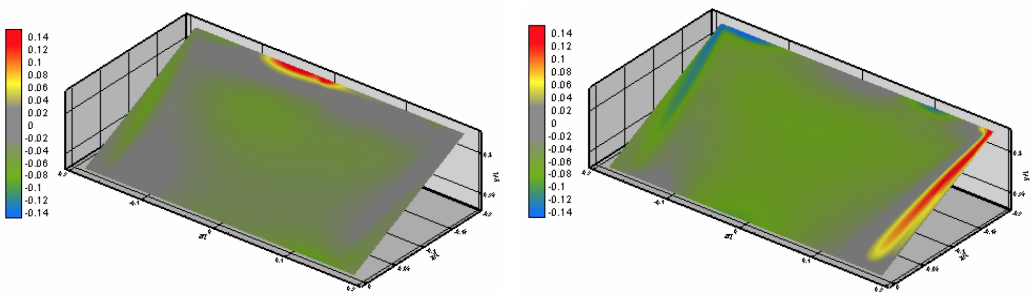

(a) 200mm (b) 40mm

Figure 2.17: Scalar Scenes of Change in C_{P} on the Slant Angle at two Wall Separations from Strachan's CFD data[17]

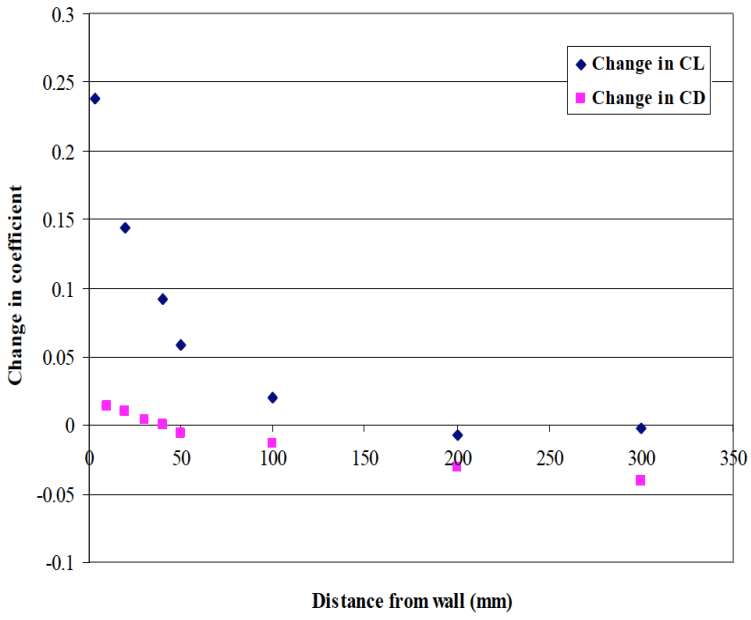

Figure 2.18: Change in C_{D} and C_{L} on Ahmed Body vs Wall Separation Distance-Experimental data [17]

CHAPTER 3: SIMULATION SETUP

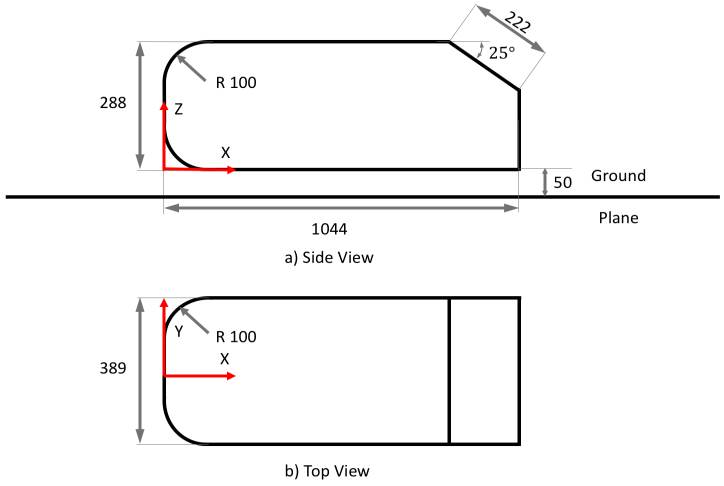

Figure 3.1: Ahmed body used in this thesis with axis (dimensions are in mm)

The Ahmed bluff body model that was used in this thesis is available in Figure 3.1 and this figure shows the axis system that was used in the entire analysis. This body is used in a large virtual wind tunnel with a length of 300 meters, a width of 30 meters and a height of 15 meters. The wind tunnel contained a side wall at various separation distances from the Ahmed body. The motion of the body along the wall and approaching near to the wall is complex and hence the research was done to use a sophisticated meshing technique called the Overset Mesh. In addition, a well-defined physics setup is equally significant as the selection of mesh and this results in an appropriate and an accurate simulation. Further down the line, this chapter explains the primary importance of using overset mesh, an overview of the selected physics model and details of the setup of the simulation.

3.1 Coordinates System

Figure 3.1 shows the coordinates system used in representing the results of the CFD simulations in this thesis. This system is slightly modified from the coordinate system used by Strachan. He had used the origin point from the center of the ground exactly down the trailing edge. For this thesis, the origin point was shifted to the center of the body, starting from the face. In, Strachan's work, the vertical axis from the ground is Y, the horizontal axis is Z and longitudinal axis is X. For this thesis, the longitudinal axis is same as Strachan's but the vertical is Z axis and horizontal is the Y axis. The movement of the body along the side wall in the CFD simulations is along the negative X axis. This change of axis system is suggested to understand the wall separation distance between the body and the wall in a convenient way from the Top view using $X$and Y axis for measuring the distance traveled by the body and the wall separation distance. All the measurements of the experimental studies used for the comparisons are modified to the present coordinates system to avoid confusion.

3.2 Mesh Techniques and Choice of Mesh

A number of meshing techniques were studied before the use of present Overset Mesh technique[19]. For moving bodies in a fluid, there are three types of grid generation techniques which were developed over two decades. First one is grid deformation technique in which the computational grid around a moving body is adjusted at each time step such that it conforms to the new position of the body. This technique is useful in making the flow solver fully conservative but the extent of the motion of the moving body cannot be large when compared to the length of the body. Although the sliding mesh technique was induced into the grid, the overlapping of the grids is not viable with this technique. The second is the grid re-meshing technique where the grid over the moving body is re-meshed for every time step it moves. This helps in the scale of motion of the body but the re-meshing of the grid for ever time step

is an expensive and time-consuming job. Moreover, the overlapping of the mesh is not possible which is the primary interest in this thesis. Finally, the overlapping grid approach where the mesh is moved in a stationary mesh yielding a greater degree of freedom in utilizing the mesh over the body when compared to the other two models. The grid is locally refined and can be rotated and translated at once. The overlapping of the grids is the primary feature that is advantageous to multiple moving bodies.

In brief, the Overset mesh or Chimera is convenient and economical in the usage of cells in the domain. This method allows the user to generate the required mesh to each individual component of an intuitive allowance of refinement based on the flow around the object. Nevertheless, it still unites individual regions to give a comprehensive result. Since the mesh can be done over each individual component, the expense of computing numerous cells in the unwanted regions is evaded. Each individual region is allowed for local refinement with no dependencies on other regions. Simulating motion to the bodies is simplified, compared to previous meshing techniques. This allows moving the regions as rigid bodies giving a scope to maintain boundary layers and opens a door for intricate motions to each body. The overset mesh calculates a steady solution even in transient simulation by updating the solution with each time step. If there is motion specified to the region, then the cells of the region are moved through the background mesh for each time step and the solution affects the domain globally.

As a part of this thesis and based on the usage of the commercial CFD software, StarCCM+[20] generates overset mesh in a simple way provided clean geometry and properly segregated regions. It also follows the rules of overset by creating a group of cells in the global mesh. This software creates a group of *active*,*inactive* and *acceptor* cells. The *active* cells are the cells inside the overset region used for calculating the flow equations. The *inactive* cells are the cells outside the overset region and no flow equations are solved in those equations. However, the *inactive* cells become active

when they are in contact with the *active* cells using *acceptor* cells. The *acceptor* cells act as a bridge between the flow solving and idle cells in the transformation of data through various interpolating techniques. Using this methodology, the software constrains the user to have a reasonable solution by enforcing the mesh to create an overlap zone. This zone is used as a mixing zone where the background mesh and the Overset mesh within this zone have a cell size of the same order of magnitude. It recommends the users to create a motion that is limited to one cell per time step. Although this software has many features, as the complexity of the problem increases, various other parameters play an important role along with these rules. The interpolation of the interface of overset region, the intricacy of the geometry, multiple overset regions interaction, interference of background geometry with the overset geometry and a few other meshing irregularities cause a discrepancy in the solution. However, this mesh method gives a reliable solution than the standard way of approach to the same scenario.

3.3 Choice of Physics Model

Choosing an appropriate physics model for a simulation widely depends on the complexity of the flow field, the intricacy of the geometry shape, availability of computational resources and the level of details that are needed to analyze the flow field. From the literature, there are a wide variety of Turbulence models available for each individual use. For steady state, Reynolds Averaged Navier - Stokes (RANS) is used along with a turbulence model to overcome the closure problem. One equation, two equation transport models, and other Reynolds Stress models are a part of the turbulence models available in the literature. For transient simulations, there are Unsteady RANS (URANS), DES, LES, DDES, IDDES, VLES and DNS models. Each model has a different approach in solving the fluid flow equations. Previous studies on Ahmed body show that many authors had used turbulence models based on the geometry type, fluid Reynolds numbers, and availability of computational resources.

Initially, a brief description of the fluid flow equations of Navier - Stokes[21] are to be mentioned to understand the turbulence modeling and its limitations.

$$\frac{\partial \tilde{u}_{\mathrm{i}}}{\partial t} + \tilde{u}_{\mathrm{j}} \frac{\partial \tilde{u}_{\mathrm{i}}}{\partial \tilde{x}_{\mathrm{j}}} = -\frac{1}{\rho} \frac{\partial \tilde{p}}{\partial x_{\mathrm{i}}} + \nu \frac{\partial^2 \tilde{u}}{\partial x_{\mathrm{j}} \partial x_{\mathrm{j}}} \tag{3.1}$$

The Navier-Stokes equation contains the flow features like velocity, pressure, density, time, and location to understand the flow phenomenon analytically. However, solving the flow equation to resolve the flow features at every location in a computational domain is not a feasible approach. An alternate approach was established using Reynolds decomposition called Reynolds Averaged Navier-Stokes equation:

$$\frac{\partial \tilde{u}_{\mathrm{i}}}{\partial t} + \tilde{u}_{\mathrm{j}} \frac{\partial \tilde{u}_{\mathrm{i}}}{\partial \tilde{x}_{\mathrm{j}}} = \frac{1}{\rho} \frac{\partial}{\partial x_{\mathrm{j}}} \tilde{\sigma_{\mathrm{ij}}} \tag{3.2}$$

$$\frac{\partial \tilde{u}_{\mathrm{i}}}{\partial \tilde{x}_{\mathrm{i}}} = 0 \tag{3.3}$$

In equation 3.2, $\tilde{\sigma_{\mathrm{ij}}}$ is stress tensor and it is a combination of $\tilde{p}$ (hydrodynamic pressure), μ (dynamic viscosity) and $\tilde{s_{\mathrm{ij}}}$ (rate of strain):

$$\tilde{\sigma_{\mathrm{ij}}} = -\tilde{p}\delta_{\mathrm{ij}} + 2\mu \tilde{s_{\mathrm{ij}}} \tag{3.4}$$

$$\tilde{s_{\mathrm{ij}}} = \frac{1}{2} \left(\frac{\partial \tilde{u}_{\mathrm{i}}}{\partial x_{\mathrm{j}}} + \frac{\partial \tilde{u}_{\mathrm{j}}}{\partial x_{\mathrm{i}}} \right) \tag{3.5}$$

The physics model that was chosen in this thesis is a two equation model but the choice of the model is based on the inabilities and discrepancies of other similar models. A recent article by Argyropoulos and Markatos[22] gave a deep insight into the standard and improved models of turbulence modeling in CFD. They stated that $k - \epsilon$ turbulence model is reliable for predicting the turbulent shear flows but have

shortcomings in detecting the adverse pressure gradients, near wall boundary layer formation and resultant strains which are predominantly seen in flow field around Ahmed body.This model is basically recommended for gross estimation of a flow field. The $k-\omega$ model is slightly superior to $k-\epsilon$ model with higher accuracy for boundary layers with pressure gradients and it can be easily integrated to viscous sublayer. This model is inaccurate when applied to flow with free stream boundaries which is the downside when compared to $k-\epsilon$ turbulence model. The combination of both the models is Shear Stress Transport (SST) model by Menter[23]. It has the combination of the advantages of the $k-\epsilon$ model and $k-\omega$model. This model had been validated with many applications with good results. The SST model is most prominent and industrially used turbulence model but it has some short comings on adverse pressure gradients and tends to separate early due to the calibration of eddy viscosity term which is susceptible with the slant angle (φ=25°) of Ahmed body. The base line equations that are used in SST turbulence model are as follows:

$$\frac{\partial \rho k}{\partial t}+\frac{\partial \rho u_{\mathrm{j}} k}{\partial x_{\mathrm{j}}}=P-\beta^{*} \rho \omega k+\frac{\partial}{\partial x_{\mathrm{j}}}\left[\left(\mu+\sigma_{\mathrm{k}} \mu_{\mathrm{t}}\right) \frac{\partial k}{\partial x_{\mathrm{j}}}\right] \tag{3.6}$$

$$\frac{\partial \rho \omega}{\partial t}+\frac{\partial \rho u_{\mathrm{j}} \omega}{\partial x_{\mathrm{j}}}=\frac{\gamma}{\nu_{\mathrm{t}}} P-\beta \rho \omega^{2}+\frac{\partial}{\partial x_{\mathrm{j}}}\left[\left(\mu+\sigma_{\omega} \mu_{\mathrm{t}}\right) \frac{\partial \omega}{\partial x_{\mathrm{j}}}\right]+2\left(1-F_{1}\right) \frac{\rho \sigma_{\omega^{2}}}{\omega} \frac{\partial k}{\partial x_{\mathrm{j}}} \frac{\partial \omega}{\partial x_{\mathrm{j}}} \tag{3.7}$$

$$P=\tau_{\mathrm{ij}} \frac{\partial u_{\mathrm{i}}}{\partial x_{\mathrm{j}}} \tag{3.8}$$

$$\tau_{\mathrm{ij}}=\mu_{\mathrm{t}}\left(2 S_{\mathrm{ij}}-\frac{2}{3} \frac{\partial u_{\mathrm{k}}}{\partial x_{\mathrm{k}}}\right)-\frac{2}{3} \rho k \delta i j \tag{3.9}$$

$$S_{\mathrm{ij}}=\frac{1}{2}\left(\frac{\partial u_{\mathrm{i}}}{\partial x_{\mathrm{j}}}+\frac{\partial u_{\mathrm{j}}}{\partial x_{\mathrm{i}}}\right) \tag{3.10}$$

$$\mu_{\mathrm{t}} = \frac{\rho a_1 k}{\max(a_1\omega, \Omega F_2)} \tag{3.11}$$

From the Equations (3.6) to (3.11) there is a production term P, a dissipation term τ_{ij}, a shear stress S_{ij} and eddy viscosity equation μ_{t} and these are a combination of $k-\omega$ and $k-\epsilon$ turbulence models. To overcome the short comings of early separation of adverse pressure gradient flows, the constant a_1 is to be adjusted to delay the separation and for some other cases, the turbulent Schmidt number based model constants are adjusted to predict the flow accurately in the reattached and recirculating flows[24]. The turbulent Schmidt number based model constants are slightly focused at this point. The SST model hindered the process of predicting the actual flow over the Ahmed body with 25° backlight angle. The model constants that are originally proposed by Menter et al.[23] were changed in the flow solver. The values of the model constants were used from the literature proposed by various authors and only one set of values proposed by Bredberg et al.[25] were utilized in this thesis. Bredberg et al. used a new formulation derived from original formulation of Wilcox[26] $k-\omega$ and Launder and Spalding's[27] $k-\epsilon$. He considered SST menter's[23] turbulent cross diffusion term, $k-\epsilon$ viscous cross-diffusion term and $k-\omega$ pressure-diffusion process for his new formulation. However he had used the turbulent Schmidt numbers proposed by Launder and Spalding[27] $\sigma_{\mathrm{k}} = 1.0$ in his formulation and a slightly tweaked value ofσ_{ω} from 2.0 to 1.8. He optimized the wall distance free damping function based on the DNS data of fully developed channel flow. Below equations are the final formulation of this model with the model constants that are used in this thesis for predicting the flow over the slant angle of Ahmed Body.

$$\frac{\mathrm{D}k}{\mathrm{D}t} = P_{\mathrm{k}} - C_{\mathrm{k}} k\omega + \frac{\partial}{\partial x_{\mathrm{j}}}\left[\left(\nu + \frac{\nu_{\mathrm{t}}}{\sigma_{\mathrm{k}}}\right)\frac{\partial k}{\partial x_{\mathrm{j}}}\right] \tag{3.12}$$

$$\frac{\mathrm{D}\omega}{\mathrm{D}t} = C_{\omega 1}\frac{\omega}{k}{}_{\mathrm{k}} - C_{\omega 2}\omega^2 + C_{\omega}\left(\frac{\nu}{k} + \frac{\nu_{\mathrm{t}}}{k}\right)\frac{\partial k}{\partial x_{\mathrm{j}}}\frac{\partial \omega}{\partial x_{\mathrm{j}}} + \frac{\partial}{\partial x_{\mathrm{j}}}\left[\left(\nu + \frac{\nu_{\mathrm{t}}}{\sigma_{\omega}}\right)\frac{\partial \omega}{\partial x_{\mathrm{j}}}\right] \tag{3.13}$$

The turbulent viscosity is given below

$$\nu_{\mathrm{t}} = C_{\mu} f_{\mu} \frac{k}{\omega} \tag{3.14}$$

$$f_{\mu} = 0.09 + \left(0.91 + \frac{1}{{R_{\mathrm{t}}}^3}\right)\left[1 - \exp\left\{-\left(\frac{R_{\mathrm{t}}}{25}\right)^{2.75}\right\}\right] \tag{3.15}$$

The turbulence Reynolds number is defined as $R_{\mathrm{t}}{=}k/(\omega\nu)$ and the constants in the model are $C_{\mathrm{k}} = 0.09, \quad C_{\mu} = 1, \quad C_{\omega} = 1.1, \quad C_{\omega 1} = 0.49, \quad C_{\omega 2} = 0.072, \quad \sigma_{\mathrm{k}} = 1, \sigma_{\omega} = 1.8$

For large computational domain and well-refined meshes, computing power should be adequate to simulate the flow in reasonable time. As a part of the thesis, each simulation was run over 96 computers and dual 8 core processors with parallel processing. This is effective in reducing the computing time but the CFD code is not accurate in predicting the transitional boundary layer flow. For this reason, the $\gamma - Re_{\theta}$ transitional model is used to predict the flow in the transitional layer. This model was first implemented by Menter et al.[28] for unstructured grids and massive parallel computing. However, this model was not gained wide acceptance by the CFD audience and this model is based on local variables such as momentum thickness or boundary layer edge location. This was proposed due to the unreliability of Low-Re models which are basically used for damping the turbulence in viscous sub-layer. This model was a novel approach that was evolved to avoid the need for non - local information in correlations based models. Menter et al.[28] with held few correlation terms on a

proprietary basis and published only two terms so that independent researchers can develop their own formula with these parameters. Later Suluksna and Juntasaro[29] used this frame work of $\gamma - Re_\theta$ model and developed correlation terms for transitional boundary layer flows and they calibrated[30] their model with various practical applications in CFD using the commercial code StarCCM+. They have used F_{length} (function to control transition onset location to specify the free stream edge), $Re_{\theta c}$ (momentum thickness Reynolds number where the intermittency starts to increase) and $\tilde{Re_{\theta t}}$ (transported variable for $Re_{\theta t}$) to calibrate the model. This model is being used in this thesis as an accurate prediction of the transitional boundary layer is essential for fluid separation on the rear slant of Ahmed Body which indeed gives accurate drag and lift values. To understand the effectiveness and accuracy of SST $\gamma - Re_\theta$ Transition Model, another on par leading turbulence model was chosen.

Realizable $k-\epsilon$ model is a reliable turbulence model for initial guesses and overview of the scenario, but many other $k-\epsilon$ models which are developed in the recent times give in depth insights of flow phenomenon based on their formulation. In research of those models, AKN $k-\epsilon$ with Low-Re damping function is found to have great significance in the literature and was first formulated by Abe et al.[31]. It is an improved model to original NT Low-Re model where the original model used friction velocity μ_τ as a velocity scale to predict the separating and reattaching flows. The new AKN model replaces friction velocity with Kolmogorov velocity scale u_η to avoid the singularity of the velocity at the separation points and reattaching points like the former. The governing equations those are solved are the continuity equation, ensemble averaged Navier-Stokes equation, the equations of turbulent kinetic energy k and its dissipation rate ϵ. The original NT Low-Re model solves the above equations and uses modified model functions which reflect multiple length scales involved in shear flows and also to satisfy the requirements for the near-wall limiting behavior of

turbulence. Apart from the above equations, the model functions that were used by Nagano and Tagawa[32][33] in their model were:

$$f_\mu = \left\{1 - exp\left(-\frac{y^+}{26}\right)\right\}^2 \left(1 + \frac{4.1}{R_t{}^{\frac{3}{4}}}\right) \tag{3.16}$$

$$f_\epsilon = \left\{1 - exp\left(-\frac{y^+}{6}\right)\right\}^2 \left[1 - 0.3exp\left\{-\left(\frac{R_t}{6.5}\right)^2\right\}\right] \tag{3.17}$$

The y^+ value in the equations 3.12 and 3.13 is $u_\tau y/\nu$ and $R_t{=}k^2/\nu\epsilon$ where u_τ is friction velocity. The improved model has same equations to solve but the model functions are introduced with Kolmogorov Velocity scale u_η and the equations are:

$$f_\mu = \left\{1 - exp\left(-\frac{y^*}{14}\right)\right\}^2 \left[1 + \frac{5}{R_t{}^{\frac{3}{4}}} exp\left\{-\left(\frac{R_t}{200}\right)^2\right\}\right] \tag{3.18}$$

$$f_\epsilon = \left\{1 - exp\left(-\frac{y^*}{3.1}\right)\right\}^2 \left[1 - 0.3exp\left\{-\left(\frac{R_t}{6.5}\right)^2\right\}\right] \tag{3.19}$$

where $y^* = u_\epsilon y/\nu$. This AKN Low-Re $k - \epsilon$ model was proposed to avoid the discrepancies created by the wall functions employed in the separating region. This model is also used in the thesis to identify the best turbulence model that predicts the flow accurately over the Ahmed body in an isolated case. Further, the chosen one is used for the wall proximity cases to identify the flow in comparison to the experimental data of Strachan et al.[17]. However, the primary goal of choosing the turbulence model is to identify the flow accurately for this specific case and comments are made on either of the turbulence models for their efficiency and accuracy.

3.4 Hierarchy of the Simulation Settings

Abundant studies that were made on the Ahmed body enabled me to understand the CFD simulation setup. Starting from the geometry import, the Ahmed body

without the stilts model shown in Figure 3.1 was designed in SolidWorks and later imported it into StarCCM+ as a CAD file. A virtual wind tunnel domain was prepared with the dimensions of $150L \times 50L \times 25L$ m^3, which is sufficient for isolated Ahmed body and Wall proximity cases. The dimensions of the overset region which was around the body are $6L \times 3L \times 3L$ m^3 and the wake refinement was sufficiently placed inside the region. For wall proximity cases, the dimensions of the side wall ($60L \times 0.75L \times 1L$ m^3) were modified from the dimensions of side wall used by Strachan as the procedure of emulating the flow in CFD is different from the experiment. The side wall was placed at the first separation point which is the maximum separation distance between the wall and body. After the meshing, for every other separation distance, the Overset region was conveniently moved to the required position before running the simulation. This is another advantage of Overset mesh over the standard meshing approach. In Figures 3.2 and 3.3 the meshing pattern and the refinement around the moving geometry are clearly shown. The flow around the geometry was known to have adverse pressure gradients and hence the wake refinement was added to the geometry. The prism layers are in an ascending order and the side wall contains a few prism layers to identify the boundary layer development as the body approaches near to the wall. The mesh settings for the overset region are shown in Table 3.1. The mesh size used in the overset region for both the isolated and wall proximity cases was 25 million.

The boundaries of a case are vital for the simulation to initiate the solution. In this simulation, the face opposite to Ahmed body's face was used as velocity inlet with 0 m/sec velocity through out the simulation, the face opposite to the back of Ahmed body was used as pressure outlet to remove the pressure fluctuations caused by the movement of overset region, the ground was used as no slip moving wall (the ground with respective to the fluid is considered stationary) and all other faces of the domain were used as symmetry walls where the velocity gradient adjacent to the wall

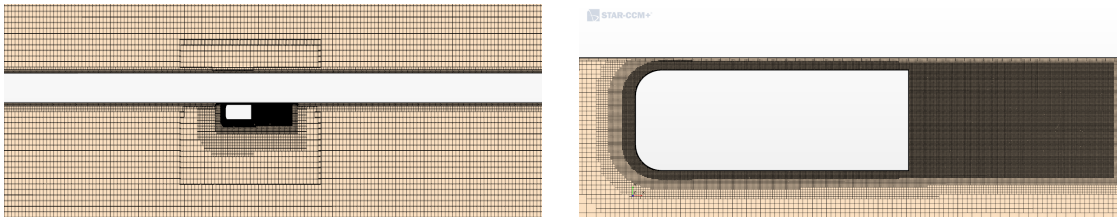

(a) Distant View (b) Close View

Figure 3.2: Mesh Scenes of the Domain and Ahmed body over a plane normal to $Z/L = 0.186$ Plane

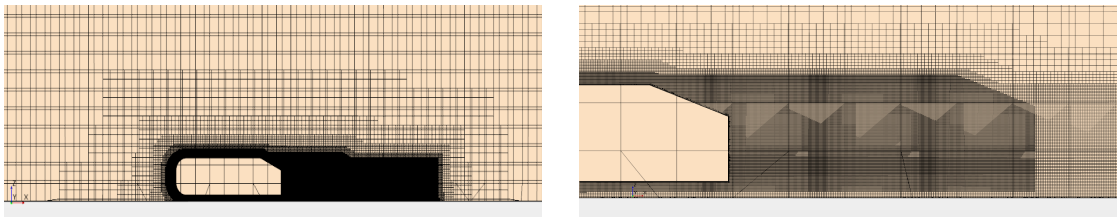

(a) Distant View (b) Close View

Figure 3.3: Mesh Scenes of the Domain and Ahmed body over a plane normal to $Y/L = 0$ Plane

is continued over the wall. The fluid properties in the domain were properties of air at mean sea level (ρ= 1.205 kg/m^3, μ = 1.82 x 10^{-5}N.s/m^2). However, for initialization of the solution, a velocity of 25 m/sec was used and this velocity was taken after Strachan's [8] experiment on Ahmed body. Each simulation was ran for 2 physical seconds time with a time step of 0.00025 seconds which in turn results in a CFL number of 2.5. A 1st order temporal discretization with an implicit unsteady solver is used to run the simulation with less computing power and reliable accuracy. Prior to the start of the simulation, the reports of force coefficients and Moment coefficients were activated to analyze the solution convergence and to observe the values during the simulation.

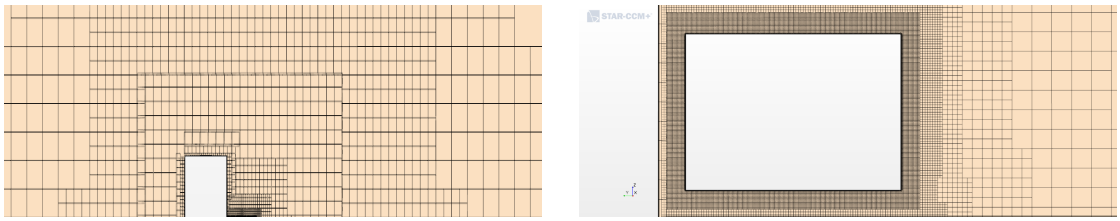

(a) Distant View (b) Close View

Figure 3.4: Mesh Scenes of the Domain and Ahmed body over a plane normal to $X/L = 0.5$ Plane

Table 3.1: Values of the Mesh Parameters.

Mesh Parameters	Value
Base Size	20 mm
Minimum Trimmed Cell Size	2.25 mm
No.of Prism Layers	15
Prism Layer Thickness	3 mm
Prism Layer Last Node Thickness	0.001 mm

CHAPTER 4: RESULTS AND DISUCSSIONS

After the completion of mesh and physics setup, isolated Ahmed body simulations were allowed to run followed by wall proximity simulations with a chosen turbulence model for a prescribed time and the initial convergence of the solution was monitored through the C_{D} and C_{L} values. Post-completion of the simulations, all the force and moment coefficient values were gathered, normalized velocity profiles of the flow over various parts of the body were plotted for further validation process. This chapter begins with the discussion of the requirement of modified $k-\omega$ SST turbulence model (here after mentioned as SST) over standard SST model. Later, discussions were made on the results obtained from Isolated Ahmed body with the selected mesh and physics models in comparison to the experimental results of Strachan et al[8]. Later the choice of turbulence model to use in the wall proximity simulations is justified with the level of accuracy in the results attained by previous isolated case studies. Further, the results of all wall proximity simulations were gathered and compared with the isolated Ahmed body simulation results. Finally, this section concludes by highlighting the changes occurred in each case and effects of the wall proximity over the body are deduced from the analysis previously made.

4.1 Isolated Ahmed Body

The isolated Ahmed body simulation was first run with a standard $k-\omega$ SST turbulence model including the $\gamma - Re_{\theta}$ Transition model in order to identify the base mesh size that is optimum to approach a good converged C_{D} value. As discussed earlier, the standard SST model has drawbacks in predicting accurate flow phenomenon comprising of adverse pressure gradients and reattaching flows. This was experienced

in the initial run of the isolated Ahmed body case. To understand the inability of standard RANS eddy viscosity based turbulence models in accurately predicting the flow over the 25° slant angle Ahmed body model, few other investigations conducted by various authors from the literature are mentioned at this point. Ashish et al.[34] showed that the Realizable $k - \epsilon$ model failed to accurately predict the flow over the 25° slant angle Ahmed body model which is shown in Figure 4.1 (a). Ashton et al.[35] commented that the RANS turbulence models can be used for grow estimation of flow over the 25° slant angle Ahmed body but RANS-LES and hybrid RANS-LES models predict the flow accurately over the rear slant. They also stated that the RANS turbulence models under predict the turbulent kinetic energy beyond the flow separation point which results in under prediction of separation bubble over the rear slant angle. The RANS turbulence models doesn't predict the reattachment point after the separation bubble leading to a full flow separation and this can be seen in Figure 4.1(b) where they used URANS-SST turbulence model for the flow prediction. Guilmineau et al.[36] discussed about the inabilities of the RANS turbulence models based on the numerical results obtained in predicting the flow phenomenon over the 25° slant angle Ahmed body model. They stated that the RANS turbulence models are incapable of accurately predicting the separation bubble over the rear slant angle and the flow reattachment over the rear slant after the separation bubble. These significantly effect the wake of the body. They used both SST and EARSM (Explicitly Algebraic Reynolds Stress Model) turbulence models to show the comparisons of flow predictions which are seen in Figure 4.1(c) and (d). From the studies made through the available literature, it is understood that the RANS turbulence models fail to accurately predict the flow features over the 25-degree slant angle Ahmed body model.

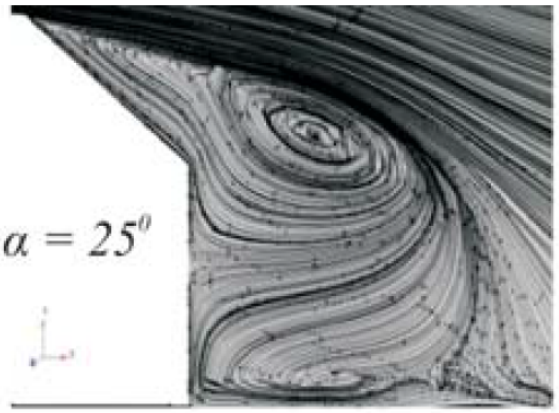

(a) RANS-Realizable $k - \epsilon$

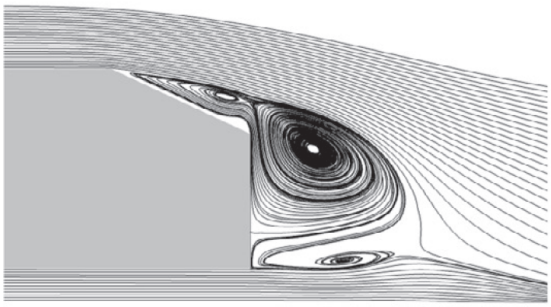

(b) URANS-SST

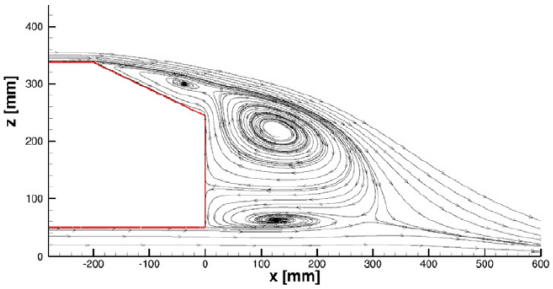

(c) RANS-SST

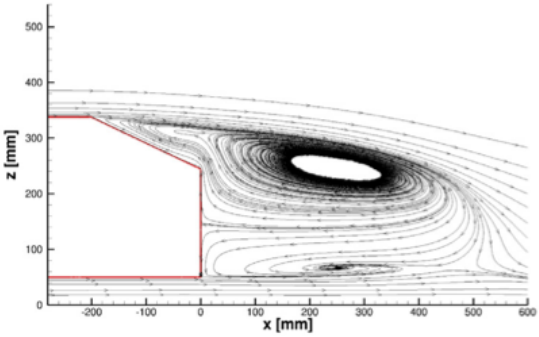

(d) RANS - EARSM

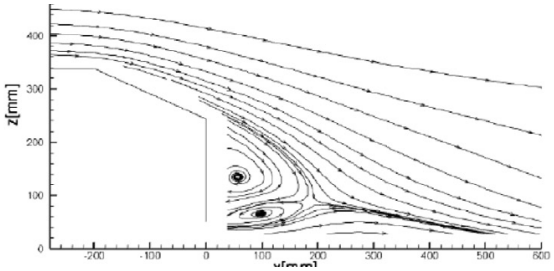

(e) Experiments

Figure 4.1: Comparison of flow predictions assessed by various turbulence models from the CFD studies conducted by a) Ashish et al.[34] b) Ashton et al.[35] c) and d) Guilmineau et al.[36] and e)Lienhart et al.[6] along $Y/L = 0$ symmetry plane

As an alternative approach, the model constants in the original SST formulation were changed based on available improved analytical formulations of $k-\omega$ turbulence model but only the Schmidt number constants used in an improved $k-\omega$ turbulence model formulated by Bredberg et al.[25] gave accurate predictions of flow over the

body, velocity and vorticity magnitudes when compared with the experimental data. The model constants aided the turbulence model to overcome the discrepancy of complete separation of flow at the top edge of the rear slant. The standard SST model predicts high pressure difference at the top edge of the rear slant that energizes the turbulent kinetic energy in the flow field. This process predicts complete separation of flow beyond the top edge resulting in a lower drag value than the experimental value. To suppress the turbulent kinetic energy in the flow at the adverse pressure point, the Schmidt number constants were changed from the original values to the prescribed values as mentioned in the previous chapter. This modification in the turbulence model resulted in a drag value closer to the experimental and the flow was not separated till it reached the lower edge of rear slant.

Figures 4.2(a) and (b) show the differences of wake prediction between the Original SST model and the modified SST model. These figures clearly show the accuracy of the modified SST model in the prediction of the flow over the rear slant. To have a clear understanding of the effect of the modified SST model in the predictions, the turbulence mixing regions are to be identified in the wake region and the contour plots in Figures 4.3(a) and (b) represent the turbulent kinetic energy of the flow over the rear slant and in the wake of the body. These contour plots suggest that the flow predicted by original SST model contains high turbulent mixing of the fluid over the rear slant which was the effect of adverse pressure gradient over the top edge. But the modified SST model shows an accurate prediction of turbulent kinetic energy over the rear slant and it shows maximum turbulent mixing in the wake which is considered as an accurate prediction based on the previous studies. These plots clearly justify the above arguments made for modifying the original SST model.

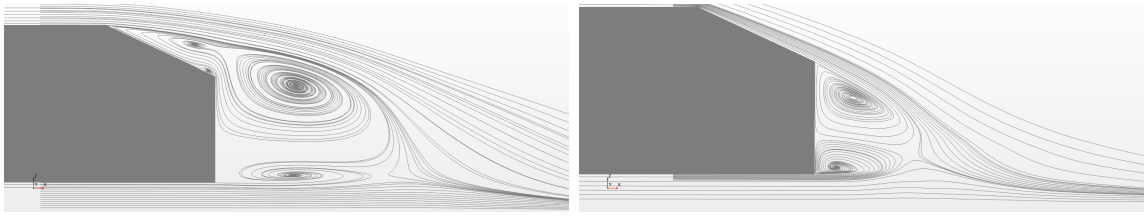

(a) (b)

Figure 4.2: Comparison of Velocity Streamlines along $Y/L = 0$ symmetry plane for the wake of the Ahmed body a) Original SST model) Modified SST model

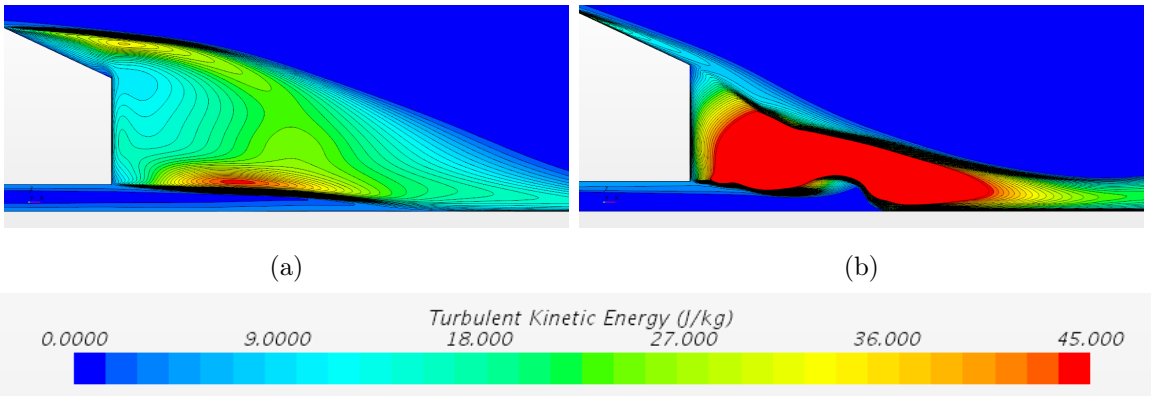

(a) (b)

Figure 4.3: Comparison of Turbulent Kinetic Energy between the original SST model and Modified SST model along $Y/L = 0$ symmetry plane. a) Contour Plot from Original SST model) Contour Plot from modified SST model

Based on the modified SST turbulence model, a mesh sensitivity analysis was conducted to utilize an optimum mesh for further simulations. Many mesh sizes were tested and mesh sensitivity effect was evaded after reaching the highest mesh size of 50 million cells in the overset region. However, on the basis of economical usage of computational resources a mesh size of 25 million cells in the overset region was used for further simulations. This decision was made over the comparison of converged C_{D} and C_{L} values of three tested mesh sizes and a few velocity profiles of flow around the body. In Table 4.1 the 25 million mesh size simulation shows a closer match of drag value to 50 million cases than the 40 million case. Figures 4.4(a) and (b) show the plots of streamwise and vertical velocity profiles of the flow at $X/L = -0.02, Y/L = 0$ line probe for three mesh resolutions in Overset region. These plots show that the three

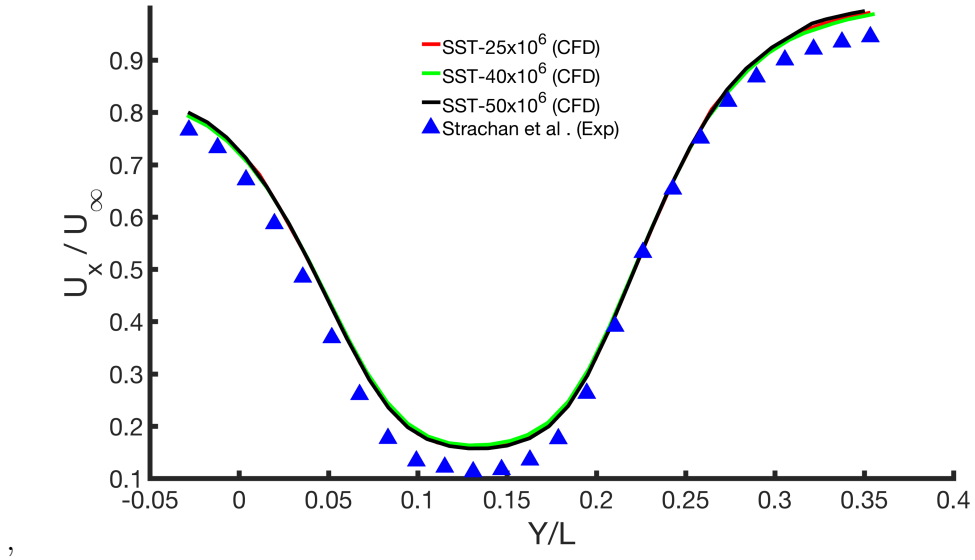

,

(a)

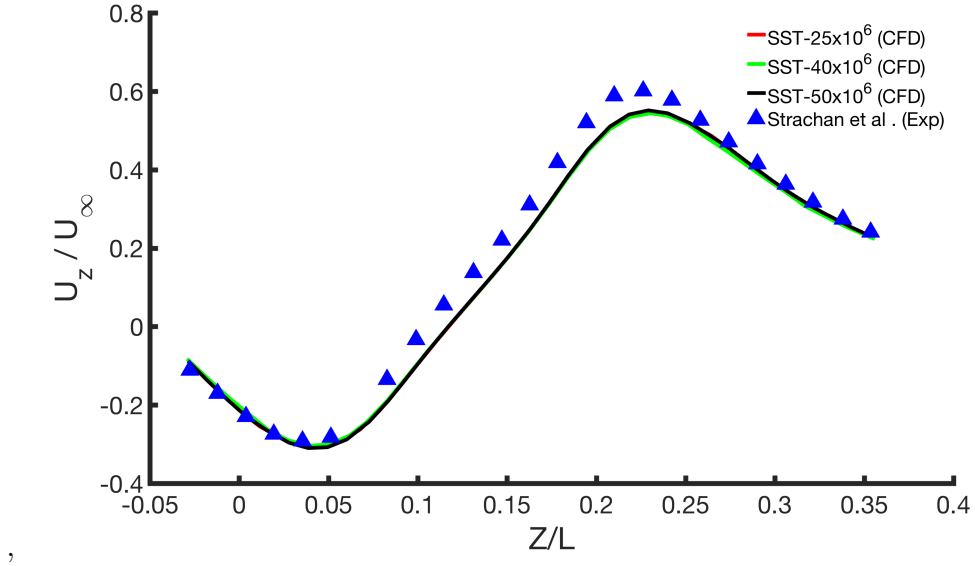

,

(b)

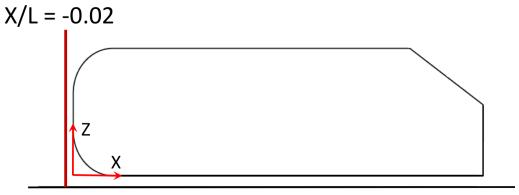

(c)

Figure 4.4: Normalized Velocity Profiles from CFD data for three mesh sizes, $X/L = -0.02, Y/L = 0$ probe location, are compared with Strachan's Data a) Normalized Streamwise Velocity ($U(x)/U_\infty$) profiles b) Normalized Vertical Velocity ($U(z)/U_\infty$) profiles c) Schematic of Line Probe

Table 4.1: Mesh Sensitivity Analysis for URANS simulations with three levels of mesh resolution in the Overset Region

Minimum Trimmed Cell Size	Mesh Size $\times 10^6$	C_{D}	C_{L}
1.875 mm	50	0.309	0.280
2 mm	40	0.312	0.273
2.25 mm	25	0.307	0.276

mesh resolutions were successful in accurately predicting the velocity of the flow in front of the body and 25 million case best matches with the 50 million mesh resolution case. Figures 4.5(a) and (b) show the precise difference between the three mesh cases and these plots show the streamwise and vertical velocity profiles over the lower edge of the rear slant of Ahmed body. The 25 million case best matches with the 50 million case, but there is a slight offset of the streamwise velocity values predicted by the 25 million case at the central zone of the plots. This offset is observed in the streamwise velocity plot shown in Figure 4.6(a), but the magnitude of vorticity predicted by the 25 million case is in good agreement with the 50 million case. Considering the above results, the 25 million mesh size case was chosen as the optimum mesh for further simulations on the basis of economical computational power usage, the comparison of the turbulence models with the experimental results were made. The obtained C_{D} and C_{L} values from the SST and AKN turbulence models are listed in Table 4.2 and 4.3 given below.

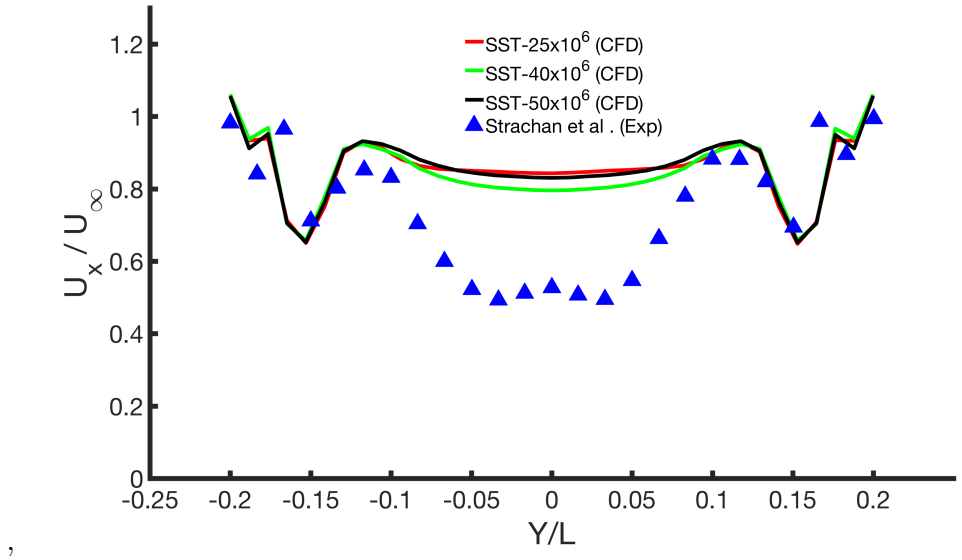

(a)

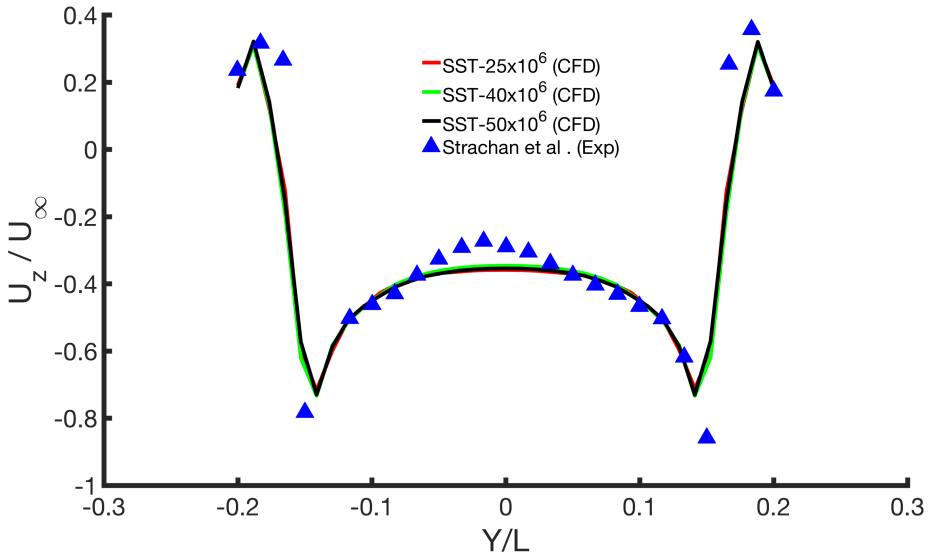

(b)

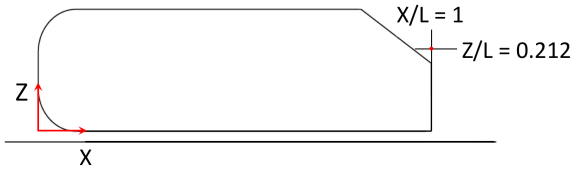

(c)

Figure 4.5: Normalized Velocity Profiles from CFD data for three mesh sizes, $X/L = 1, Z/L = 0.212$ probe location, are compared with Strachan's Data a) Normalized Streamwise Velocity ($U(x)/U_\infty$) profile b) Normalized Vertical Velocity ($U(z)/U_\infty$) profile c) Schematic of Line Probe

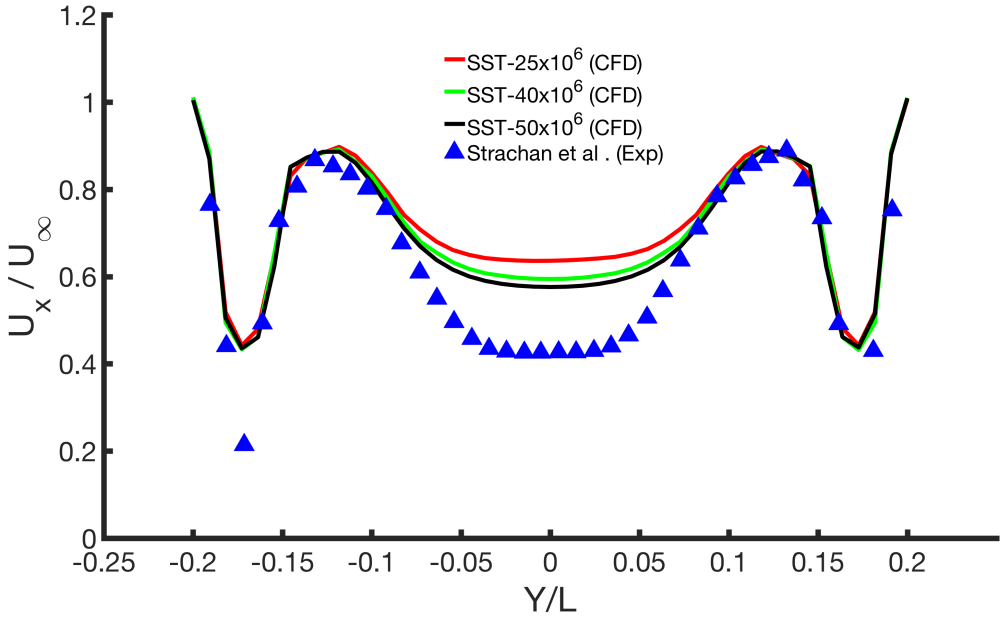

(a)

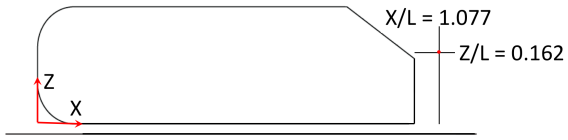

(b)

Figure 4.6: a) Normalized Streamwise Velocity ($U(x)/U_\infty$) profiles from CFD data of three mesh sizes , $X/L = 1.077, Z/L = 0.162$ probe location, are compared with Strachan's Data b) Schematic of Line Probe

Table 4.2: C_D Comparisons Between Current and Previous Studies

Authors	Procedure Used	Reynolds Number	C_D
Strachan et al.[8]	Wind Tunnel Experiment	1.7×10^6	0.300
Strachan et al.[18]	CFD - RNG $k-\epsilon$ Model	1.7×10^6	0.440
Krajnovic and Davidson[9]	CFD - Large Eddy Simulation (LES) Model	0.768×10^6	0.292
Guilmineau[13]	CFD-RANS-SST Model	0.768×10^6	0.307
Current	CFD-URANS-SST with $\gamma - Re_\theta$ Transition Model	1.7×10^6	0.307
Current	CFD-URANS-AKN $k-\epsilon$	1.7×10^6	0.357

Table 4.3: C_{L} Comparisons Between Current and Previous Studies

Authors	Procedure Used	Reynolds Number	C_{L}
Strachan et al.[8]	Wind Tunnel Experiment	1.7×10^6	0.280
Current	CFD-URANS-SST with $\gamma - Re_\theta$ Transition Model	1.7×10^6	0.276
Current	CFD-URANS-AKN $k - \epsilon$	1.7×10^6	0.272

Observing the listed C_{D} and C_{L} values, it is understood that the SST turbulence model predicts the drag and lift values closer to previous experiments and CFD studies. Additionally, the velocity profiles and contour plots of the flow in front of the body, in wake and vortices developed from the shape characteristics of the body are arranged from the gathered data to evaluate the accuracy of both the turbulence models when compared to the available experimental data.

In Figures 4.7(a) and (b), the velocity profiles along the line probe at $Z/L = 0.3021$ are plotted with Strachan's[18] experimental data. Figure 4.7(a) shows that the SST model predicts the streamwise velocity in a similar pattern as of the experimental data but the AKN model fails beyond a certain point. The SST model predicts higher magnitude than the experimental value but the AKN model predicted accurate value till $X/L = 0$. The inaccuracy in the AKN model is due to the over prediction of recirculation bubble over the top surface of the body. This over prediction resulted in offsetting the velocity profile from the regular pattern. This phenomenon is the primary interest of placing a line probe at that location. In accordance with this anomaly, Figure 4.7(b) shows a vertical velocity profile over the same line probe. This shows a good agreement of the SST with the experimental data over the AKN model. As afore mentioned, the over prediction of the recirculation bubble by the AKN model resulted in a similar offset of the vertical velocity profile as seen in Figure 4.7(a).

In validating the above argument, the accuracy attained by the turbulence models

underneath the body when there is no recirculating flow is shown in Figures 4.8(a) and (b). The streamwise and vertical velocity profiles of flow underneath the Ahmed body at $Z/L = -0.0249, Y/L = 0$ predicted by both the turbulence models are in good agreement with the experimental data unlike the predictions in Figures 4.7(a) and (b). The turbulence models were able to capture the flow velocity very effectively as there was no recirculation zone present at that location. The offset of the magnitudes of the streamwise and vertical velocities in the plot conveys a fact that the CFD predictions over predict the velocities when there is an accelerated flow. The rise in the velocities convey a fact that the flow is converged between the surface of the body and the ground creating an accelerated flow.

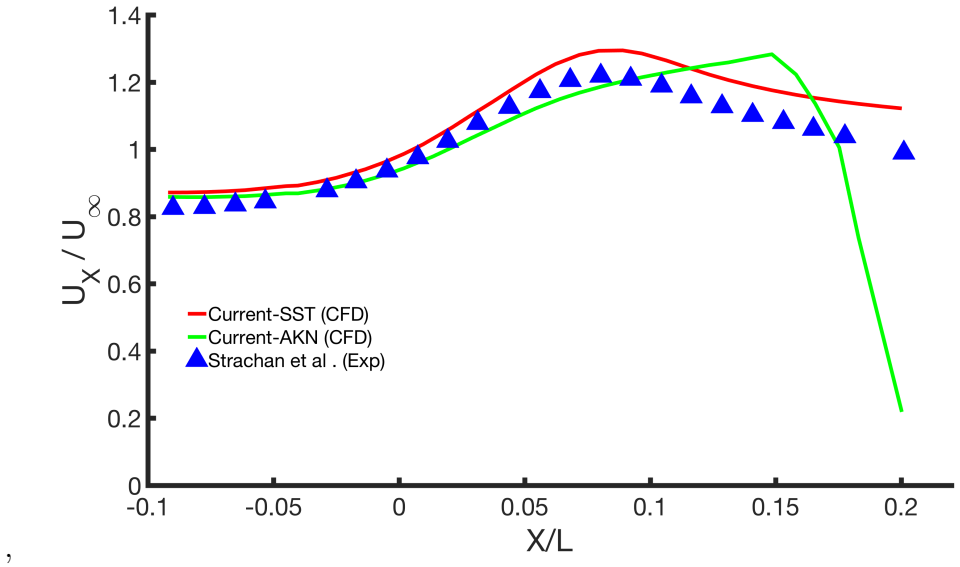

,

(a)

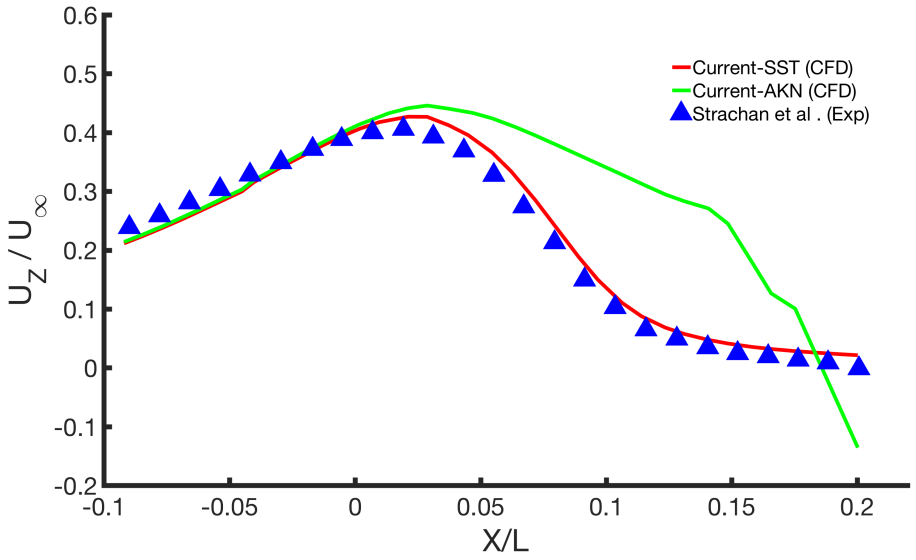

,

(b)

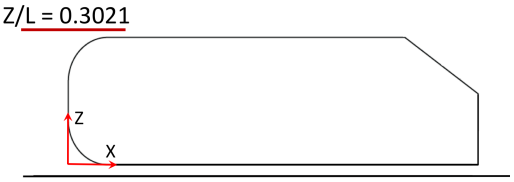

(c)

Figure 4.7: Normalized Velocity Profiles from CFD data, $Z/L = 0.3021, Y/L = 0$ probe location, are compared with Strachan's Data a) Normalized Streamwise Velocity $(U(x)/U_\infty)$ profile b) Normalized Vertical Velocity $(U(Z)/U_\infty)$ profile c) Schematic of Line Probe

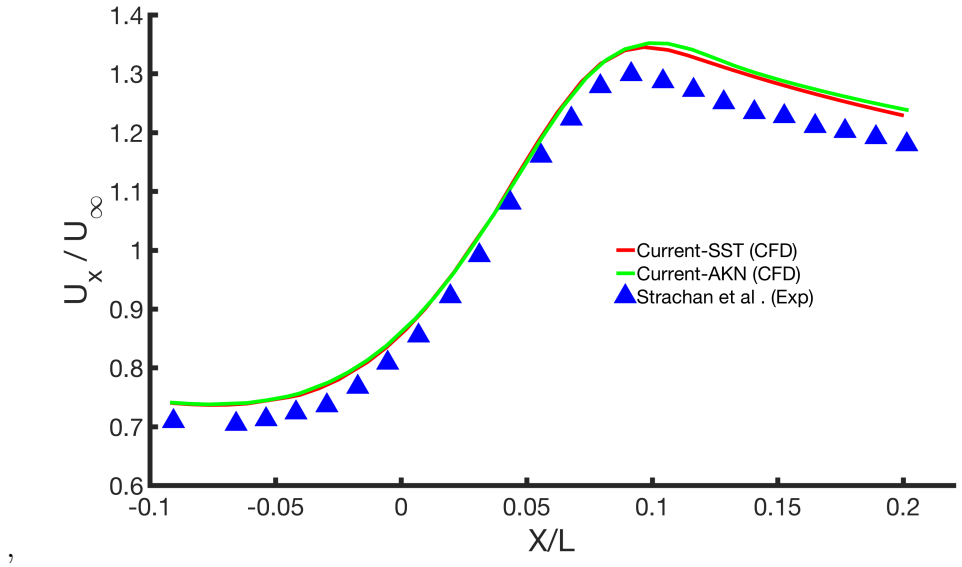

,

(a)

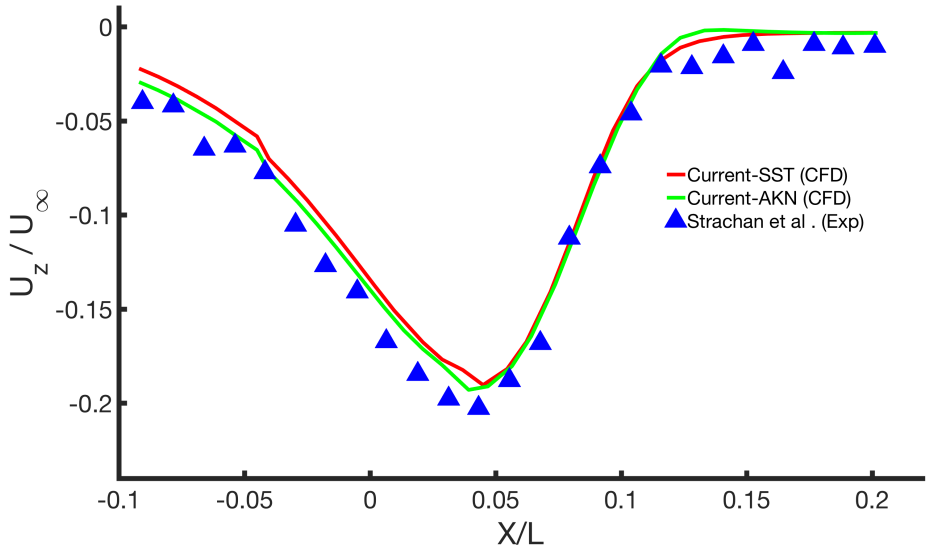

,

(b)

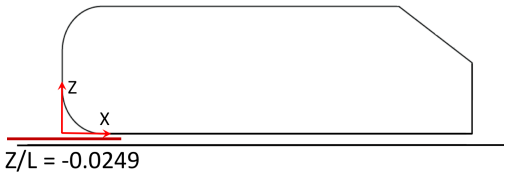

(c)

Figure 4.8: Normalized Velocity Profiles from CFD data, $Z/L = -0.0249, Y/L = 0$ probe location, are compared with Strachan's Data a) Normalized Streamwise Velocity ($U(x)/U_\infty$) profile b) Normalized Vertical Velocity ($U(z)/U_\infty$) profile c) Schematic of Line Probe

In Figures 4.9(a) and (b), the streamwise and vertical velocity profiles show that the SST model matches accurately with Lienhart et al.[5] data. Although Strachan's data show an offset in the velocity values, it depicts a similar pattern as of Lienhart's data. AKN model is also in good agreement with the experimental values and it averages between the two experimental results. However, these plots are used to ascertain the velocity of the flow field predicted by the turbulence models when compared with the experimental results.

Flow field around the Ahmed body is greatly affected by the movement of the body, but the prediction of the affected flow by the turbulence models is the ultimate challenge faced in this thesis. The wake behind the body influences the pressure drag of the vehicle. During the study of CFD validation cases of Ahmed body, it was found that the prediction of reattaching flow on the rear slant is a challenging task for the two turbulence models. In accordance with the literature, the trailing edge of the Ahmed body was also observed and velocity profiles of the vortex regions developed from edges are plotted. In Figure 4.10(a), the normalized streamwise velocity profile of the flow is plotted over the trailing edge at $Z/L = 0.212$. The SST model moderately predicts the streamwise velocity over the trailing edge which is explicitly understood from the plot, but the AKN model followed the trend of the data resulting in a good match with the extremes of vorticity, but there are considerable discrepancies at the center. However, Figure 4.10(b) shows the vertical velocity profiles where the SST model is in well agreement with the experimental data but AKN has discrepancies in the central zone of the trailing edge. These discrepancies are the result of the Skin Friction coefficient that is used in the AKN formulation where it energizes the boundary layer to change the flow into a turbulent flow.

Acknowledging the significance of wake, the flow beyond the wake is also considered for this analysis. As a part of it, the downwash of the vortices is of primary importance. The velocity profiles of the downwash were observed along the stream-

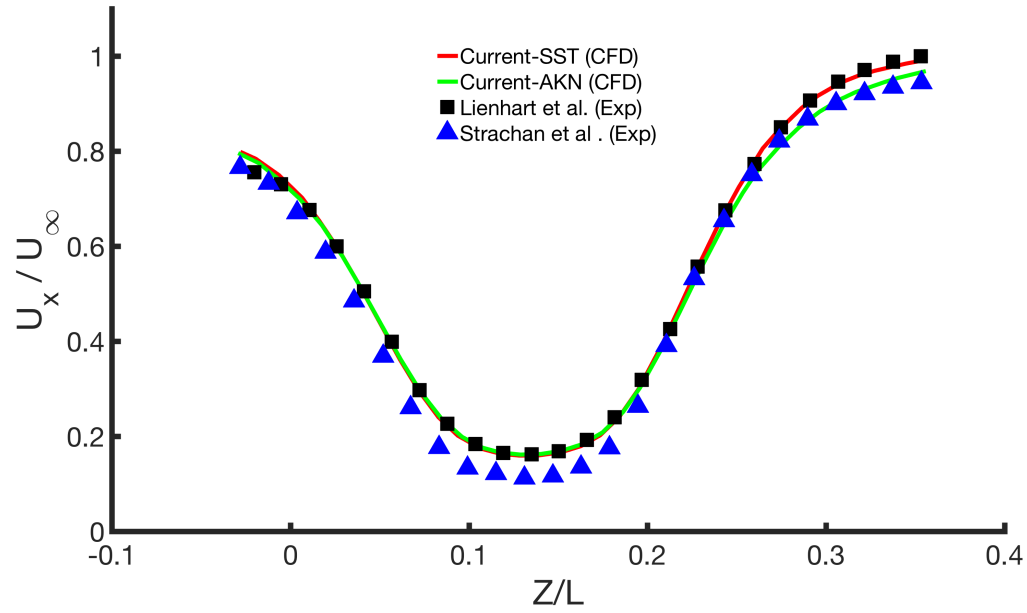

(a)

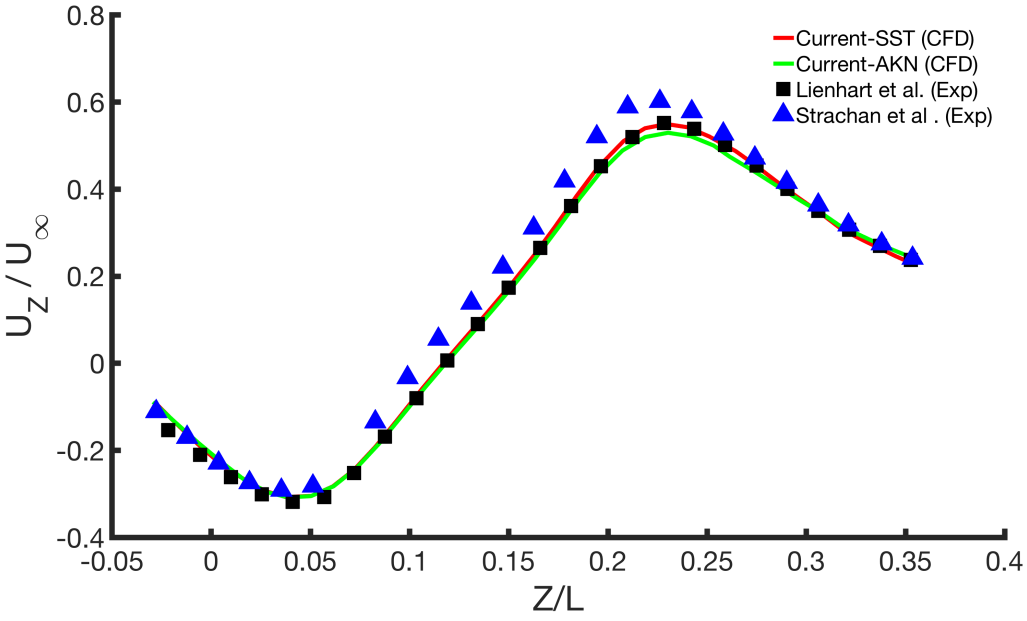

(b)

Figure 4.9: Normalized Velocity Profiles from CFD data, $X/L = -0.02, Y/L = 0$ probe location, are compared with Strachan's Data a) Normalized Streamwise Velocity ($U(x)/U_\infty$) profile b) Normalized Vertical Velocity ($U(z)/U_\infty$) profile c) Schematic of Line Probe

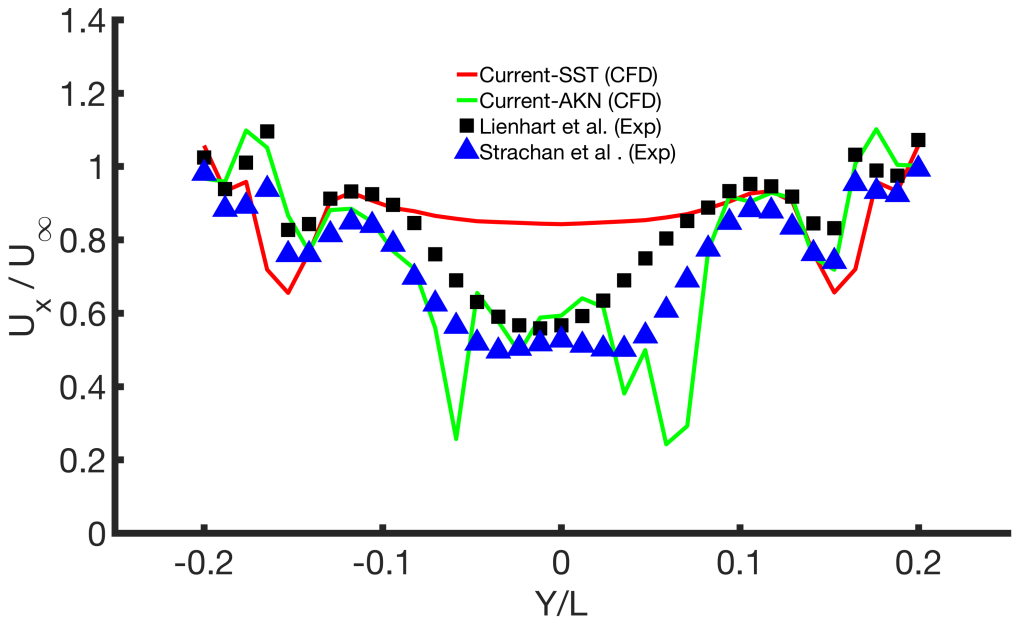

(a)

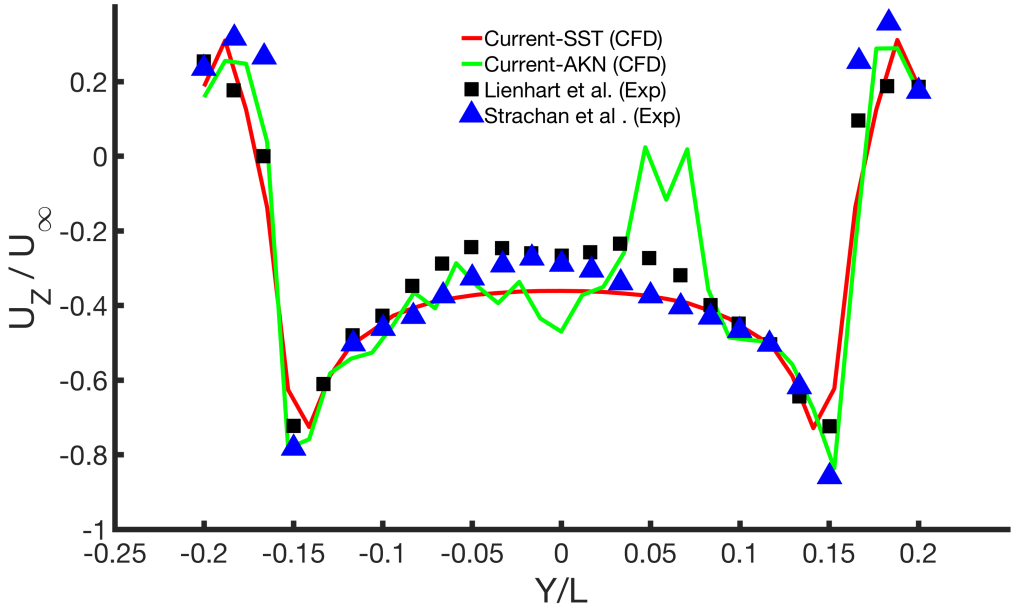

(b)

Figure 4.10: Normalized Velocity Profiles from CFD data, $X/L = 1, Z/L = 0.212$ probe location, are compared with Strachan's Data a) Normalized Streamwise Velocity ($U(x)/U_\infty$) profile b) Normalized Vertical Velocity ($U(z)/U_\infty$) profile c) Schematic of Line Probe

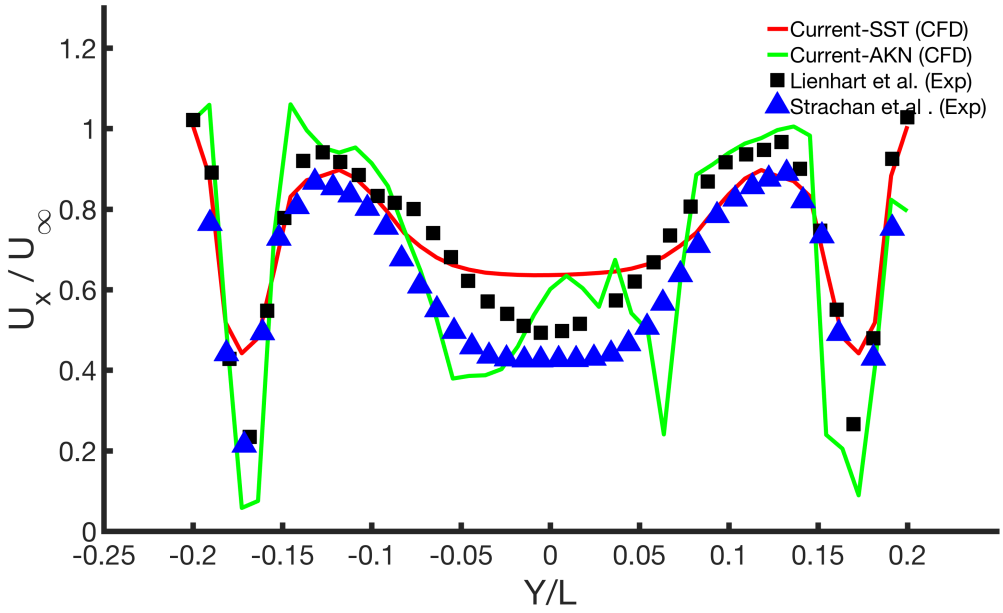

(a)

Figure 4.11: a) Normalized Streamwise Velocity ($U(x)/U_\infty$) profiles from CFD data, $X/L = 1.077, Z/L = 0.162$ probe location, are compared with Strachan's Data b) Schematic of Line Probe

wise direction to have an insight about the flow in the downwash of the wake and to understand the extent of predicting capability of the turbulence models. Normalized streamwise velocity profile of the trailing edge vortex downwash is plotted against the experimental values in Figure 4.11 and this plot reveals the accuracy of SST turbulence model over the AKN model. However, the SST model is predicting a lower magnitude of the velocity in the vortex region when compared to AKN and this inability of SST model is also observed from above results which shows the limitation of SST model for recirculating flows. Although the AKN model predictions of velocity profiles around the body were acceptable, the predictions made by the model in the wake and downwash are inconsistent.

In Figure 4.12, vertical velocity profiles of the far wake at a distance of half car length from the trailing edge ($X/L = 1.48$) were plotted. The plot shows the large vortex region where SST model is in good agreement with the experimental data

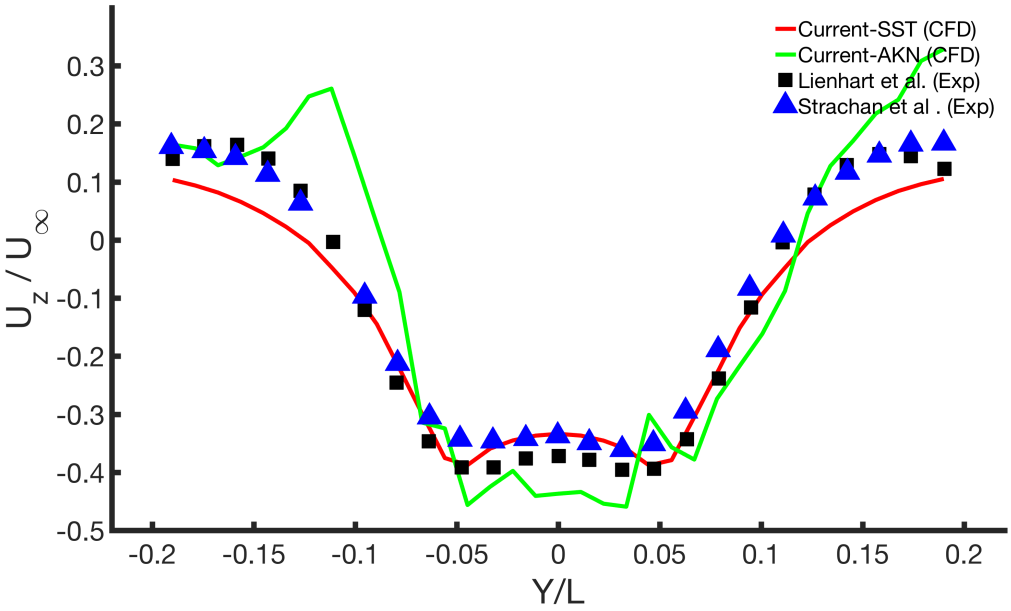

(a)

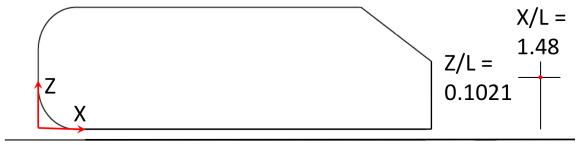

(b)

Figure 4.12: a) Normalized Vertical Velocity ($U(z)/U_\infty$) profiles from CFD data, $X/L = 1.5, Z/L = 0.102$ probe location, are compared with Strachan's Data b) Schematic of Line Probe

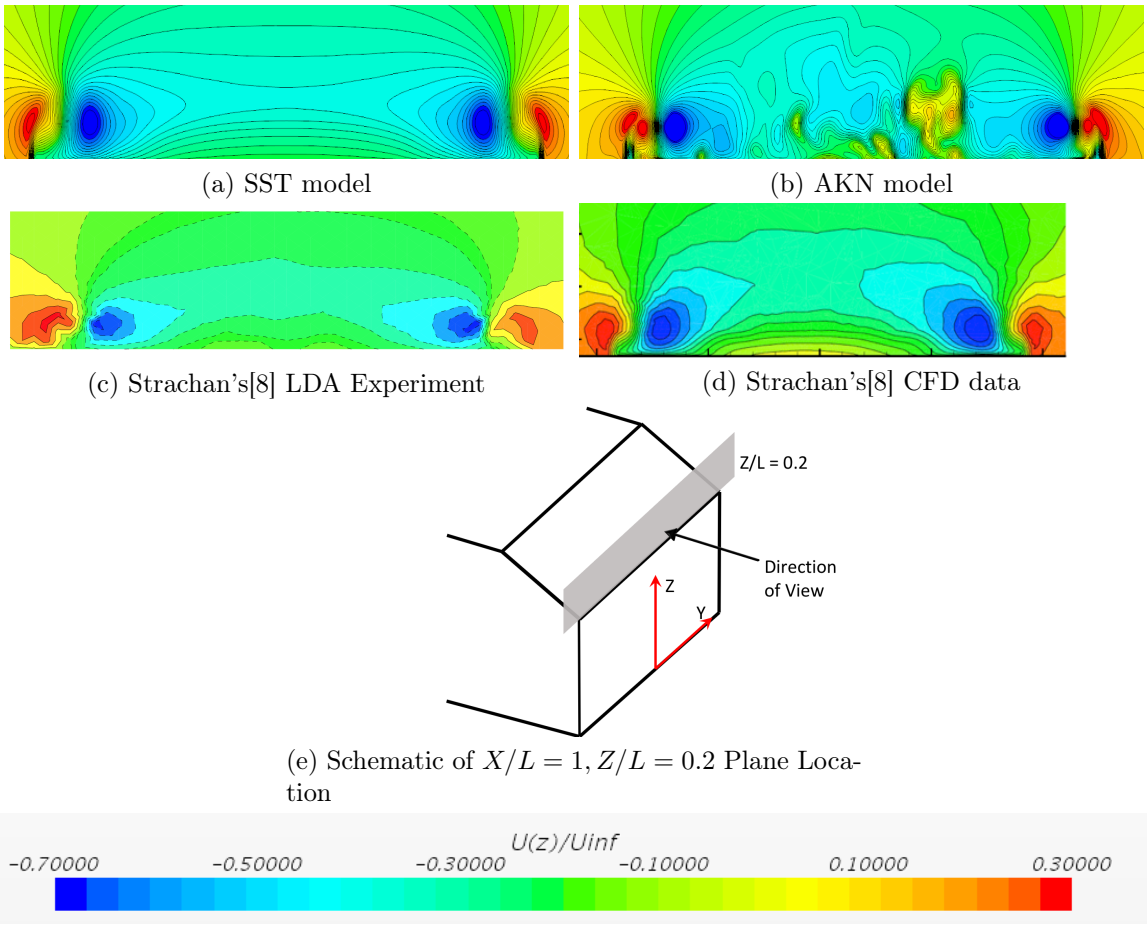

(a) SST model

(b) AKN model

(c) Strachan's[8] LDA Experiment

(d) Strachan's[8] CFD data

(e) Schematic of $X/L = 1, Z/L = 0.2$ Plane Location

Figure 4.13: Normalized Vertical Velocity ($U(z)/U_\infty$) Profiles from CFD data, $X/L = 1$, above$Z/L = 0.2$ plane location, are compared with Strachan's Data

than the AKN turbulence model. The SST model predictions are very accurate over the AKN model but the extremities of the vorticity were under predicted by the SST model. The AKN model failed in predicting the flow showing unacceptable discrepancies and creating an unnecessary confusion.

In addition to the profile plots, the velocity and pressure contour plots give a detailed understanding of the flow field around the body. In Figure 4.13, the vertical velocity contour plots projects the development and mixing of the vortices from the edges. These plots are compared with experimental and CFD results of Strachan et al.[8]. The SST model is an accurate match with the experimental result which is evidently understood from Figures 4.13(a) and 4.13(c). This conclusion was ascertained

by keen observation of high velocity over the surface in the contour plots predicted by the AKN model and CFD data of Strachan[8]. Although the vortex structure predicted by the SST model is slightly weaker than the vortex structure obtained from experiment, the extent of vortex stretching predicted by the SST model is in good agreement with the experimental result. Hence this is one primary reason to choose a different turbulence model over the Strachan's CFD model.

From the Figures 4.14(a) and 4.14(c), it is evidently understood that the SST model predicts accurate flow pattern over the rear slant than the AKN model as shown in Figure 4.14(b). The fluid was separated at the top edge of the slant angle in the AKN model showing a recirculation zone on the surface and hence the low velocity is observed in Figure 4.14(b), but the recirculation zone was not shown clearly in Figure 4.14(a) which is the downside of the SST model. The predicting capabilities of the SST model are very low for weak recirculation zones and this might be the effect of the change in model constants from the original SST model which was done to suppress the turbulent kinetic energy in the flow. Considering the transverse sections of velocity contour plots on the rear slant along the Y-axis gives a deeper insight about the recirculation and reattachment zones in the flow field and accuracy of the turbulence models in predicting the flow.

In Figures 4.15(a) to 4.15(f), the velocity scalar scenes at various transverse sections on the slant angle show the development of vortices from the edges. The streamwise velocity contour plots show the vortices that are elongated along the rear slant creating a downwash of the vortices. The SST model predictions in Figures 4.15(a) and 4.15(b) are in good agreement with the experimental data. However, the SST model predicts a delayed development of the vortex when compared with the experimental work. AKN is similar to SST model but the recirculation flow over the surface is one discrepancy that is to be noticed.

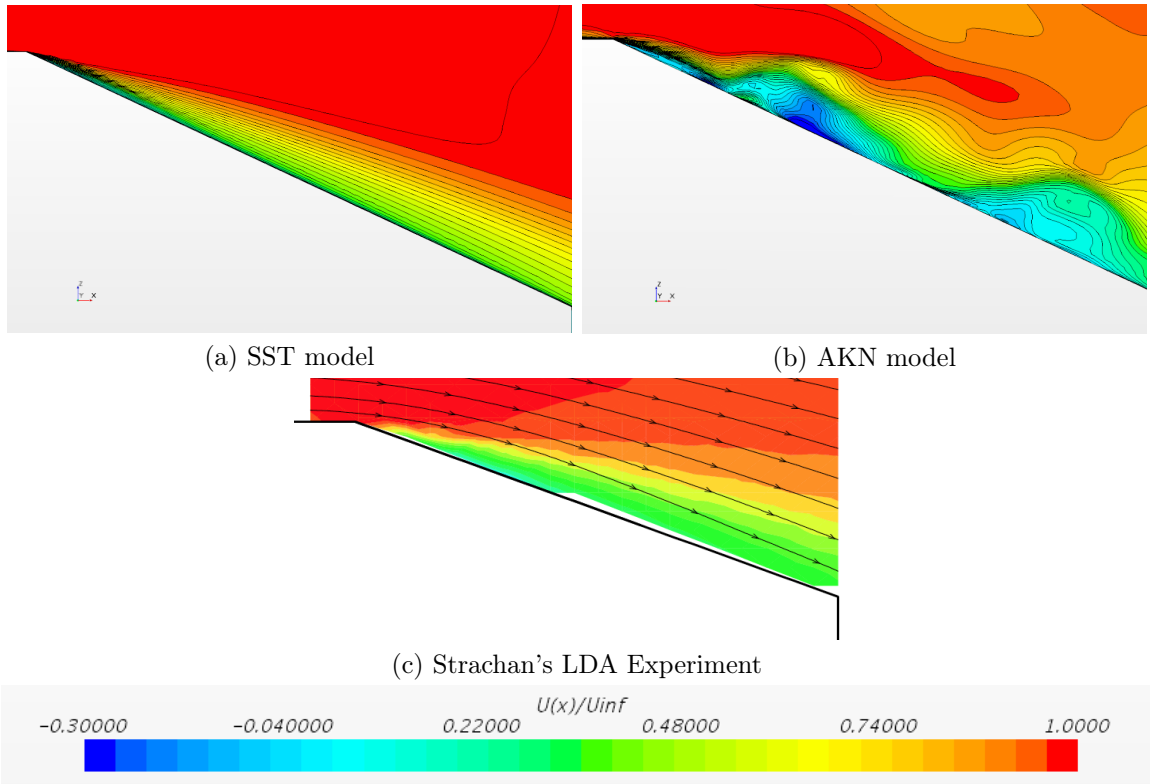

(a) SST model

(b) AKN model

(c) Strachan's LDA Experiment

Figure 4.14: Normalized Streamwise Velocity ($U(x)/U_\infty$) Contour Plots from CFD data, $Y/L = 0$ plane location, are compared with Strachan's LDA Data

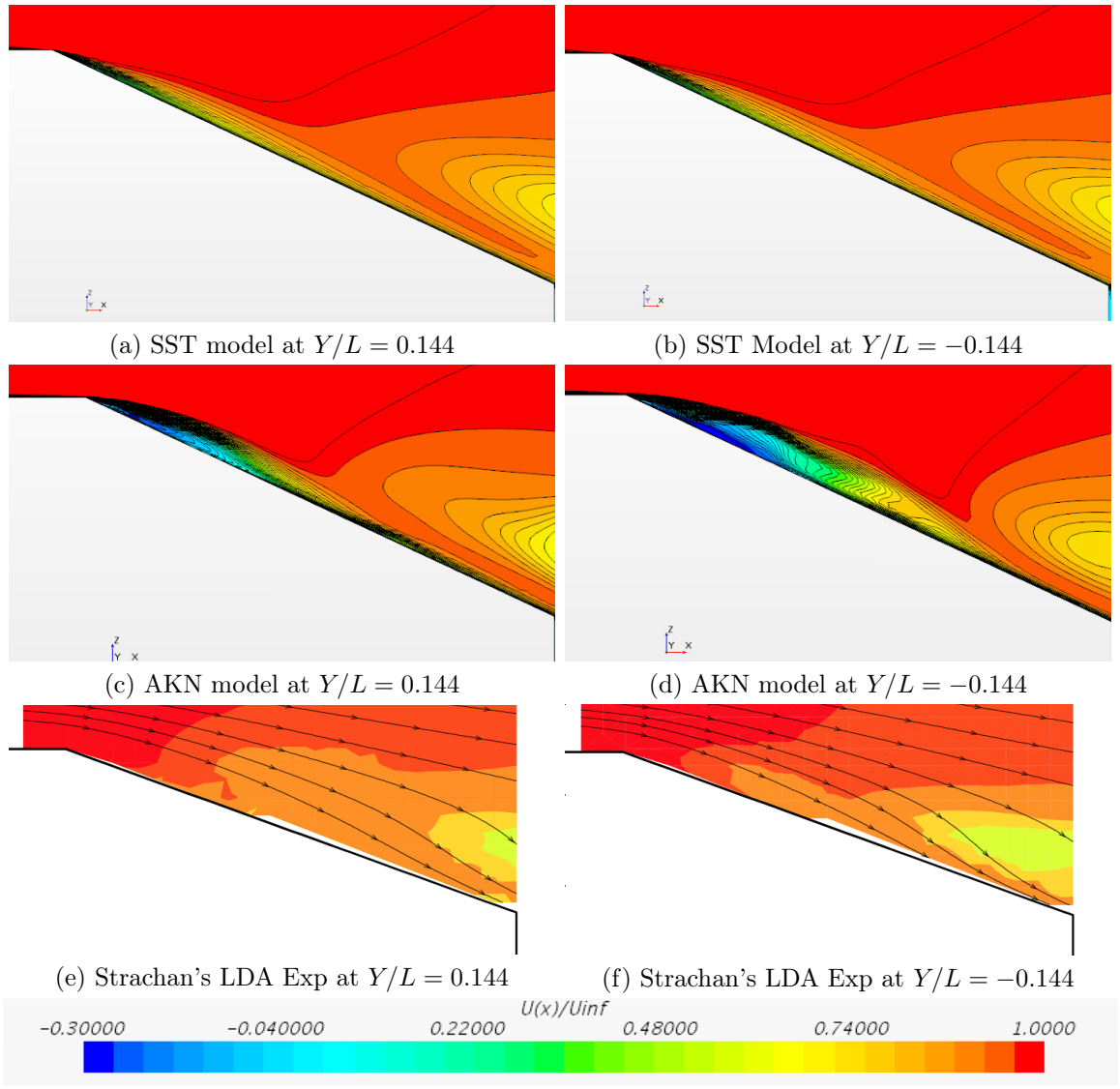

(a) SST model at $Y/L = 0.144$

(b) SST Model at $Y/L = -0.144$

(c) AKN model at $Y/L = 0.144$

(d) AKN model at $Y/L = -0.144$

(e) Strachan's LDA Exp at $Y/L = 0.144$

(f) Strachan's LDA Exp at $Y/L = -0.144$

Figure 4.15: Normalized Streamwise Velocity $(U(x)/U_\infty)$ Contour Plots from CFD data at two plane locations are compared with Strachan's LDA Data

From Figures 4.16(a) to 4.16(b), the line integration convolution plots are depicting the vortex centers and reattachment position of wake vortices. The blue outlined square marks are the vortex centers and red outlined square marks shows the reattachment position of the flow to the surface. The prediction of the vortices and the recirculation zones in the plots by SST model is more convincing than the AKN model. However, the CFD results are not up to the mark when compared with experimental data. These plots are more informative than the colored contours and this ascertains the fact that resolving the wake accurately gives appropriate results. The predicted drag value is primarily based on the wake prediction and the wake significantly accounts a majority of drag value to the pressure drag of the Ahmed Body. From the wake predicted by the SST model, it is understood that the vortex centers were not predicted accurately and the distance between the body and the centers is less than experimental results showed in Figures 4.16(c) and (d). The upper vortex is near to the lower edge of slant angle in the SST model causing a smaller wake and strong recirculation than the experimental wake. The wake predicted by the AKN model is distorted and the distance between the body and the vortex centers is less than the experimental results. The lower vortex in the wake is closer to the body in the SST model which gives an error of 4.1% in the position of the vortex center when compared with Strachan's LDA data. Moreover, the lower vortex is moderately distributed along X-axis in AKN model with an error of 4.3% in the position of the vortex center when compared with Strachan's data. The experimental vortices in the wake are considerably far from the body surface which are not shown in any of the turbulence models, but the choice of using the SST model for further Wall proximity investigations is based on the previous analysis of the results.

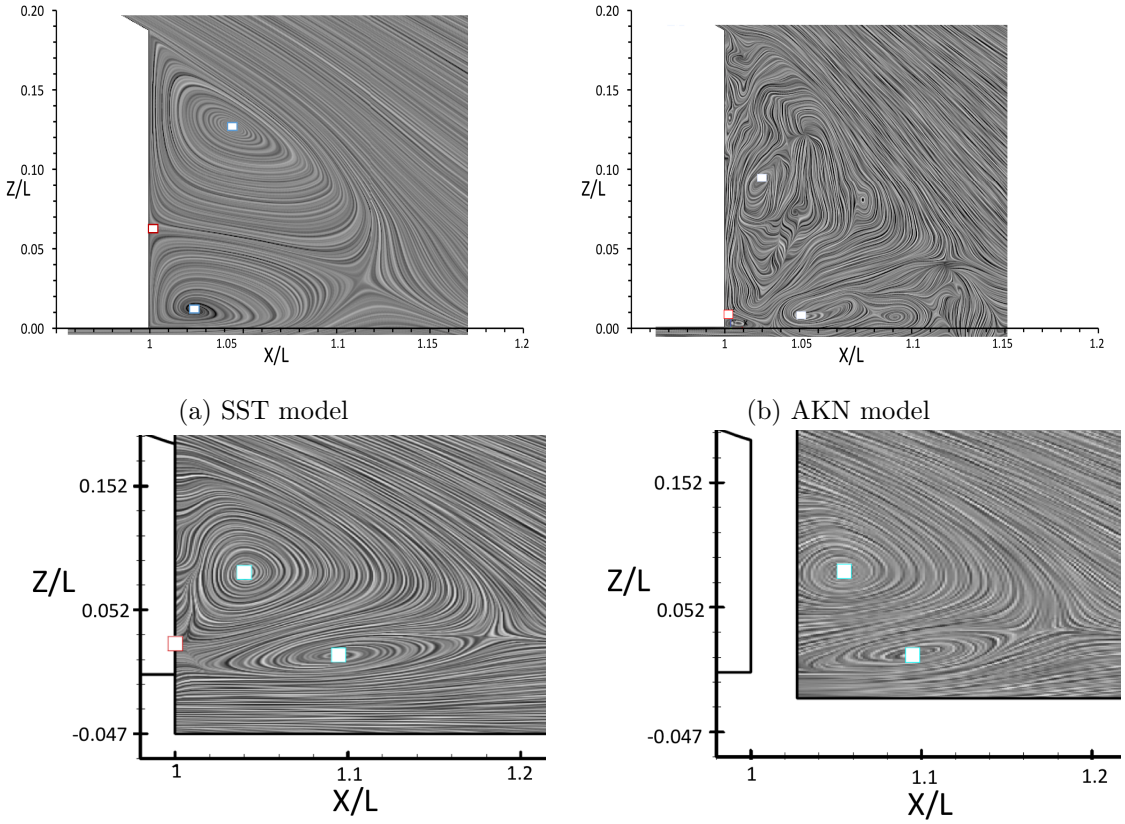

(a) SST model

(b) AKN model

(c) Strachan's LDA Experiment

(d) Lienhart's LDA Experiment

Figure 4.16: Line Integral Convolution Plots of Velocity in the Wake from CFD data compared with Strachan's[18] LDA data and Lienhart's[4] LDA data. Blue outline squares show vortex centers and red outline squares show flow reattachment position

From the Figures 4.17(a) and 4.17(b), the C_{P} values are suggesting that the negative pressure is at the upper edge of the slant angle and at vortex creating corners on the Slant Angle. This CFD data is compared with experimental results and these pressure plots are consistent with the velocity data of the flow field over the slant angle. The SST model predicted maximum low pressure at the upper edge of rear slant which is not predominantly seen in the experimental results, but the AKN model is in good agreement with Strachan's data with respective to pressure prediction on the upper edge. The flow field is continuous over the surface of the slant angle creating a high velocity at the edge for the SST model and so the lower pressure at the upper edge is justified. In fact, AKN model predicted a separation at the upper edge and reattachment down the slant angle which is similar in the experimental case but the flow features were inconsistent when compared with the experimental results. This reveals that the C_{P} data is justifying the flow pattern over the slant angle and it allows the authors to understand the relation between velocity and pressure. Based on the above results and analysis, a choice is made on the turbulence models to continue the wall proximity studies. The SST Menter $\gamma - Re_{\theta}$ Transition model is used over the AKN model for the later part of this thesis. This choice is made based on the observations of this specific case and more study needs to be done on AKN model formulation in varying the constants involving Schmidt numbers and the friction coefficient for future research.

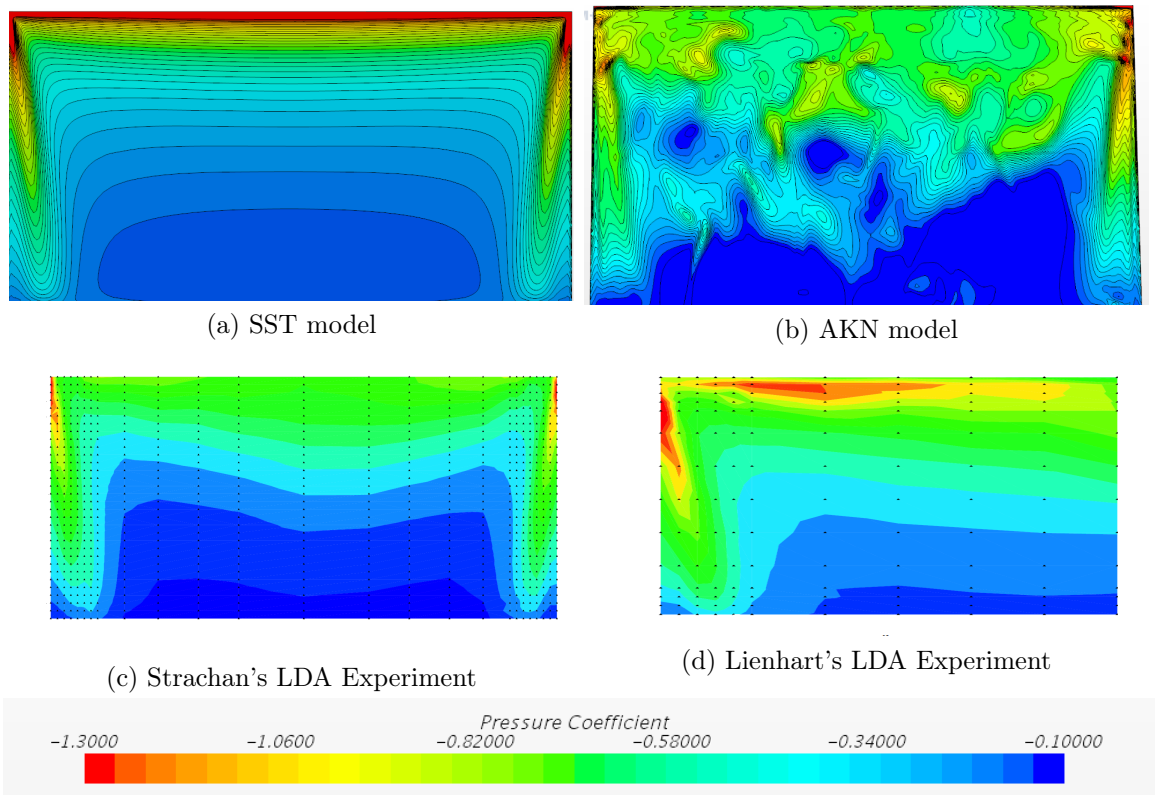

(a) SST model

(b) AKN model

(c) Strachan's LDA Experiment

(d) Lienhart's LDA Experiment

Figure 4.17: C_P Contour Plots of Backlight Area from CFD are compared with Strachan's[18] LDA Data and Lienhart's[4] LDA data

4.2 Wall Proximity Studies of Ahmed Body

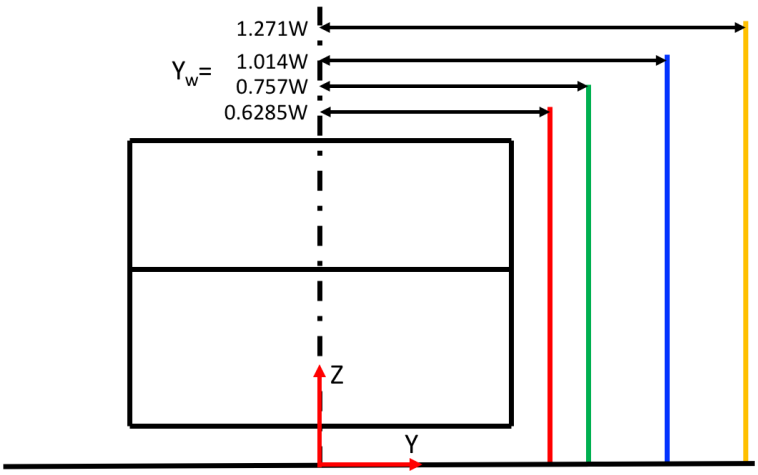

Figure 4.18: Schematic Representation of Wall Separation with respective to Ahmed body width from the center line of the body

Side Wall Proximity Studies were conducted on four wall separation distances based on the experiments conducted by Strachan et al.[17] on Ahmed body in the proximity of a side wall. Same wall separation distances which were used by Strachan et al. in their study were used in this thesis but they are represented with respective to the Ahmed body width from the center of the body (Figure 4.18). This choice of representation is made for better understanding of the wall separation distance. The representation of the separation distance in car length $L = 1.044$m is often confusing to visualize. So a better representation is suggested at this point with respective to the car width $W = 0.389$m. These investigations were performed slightly different than the original experiment, the Ahmed body in the overset region was allowed to move at a constant velocity of 25m/s keeping the fluid flow stationary. As a result, this approach is more realistic than the traditional way of CFD simulation. Nevertheless, some results are compared with standard experimental values using a relative value of each parameter. The isolated case was validated using a similar approach.

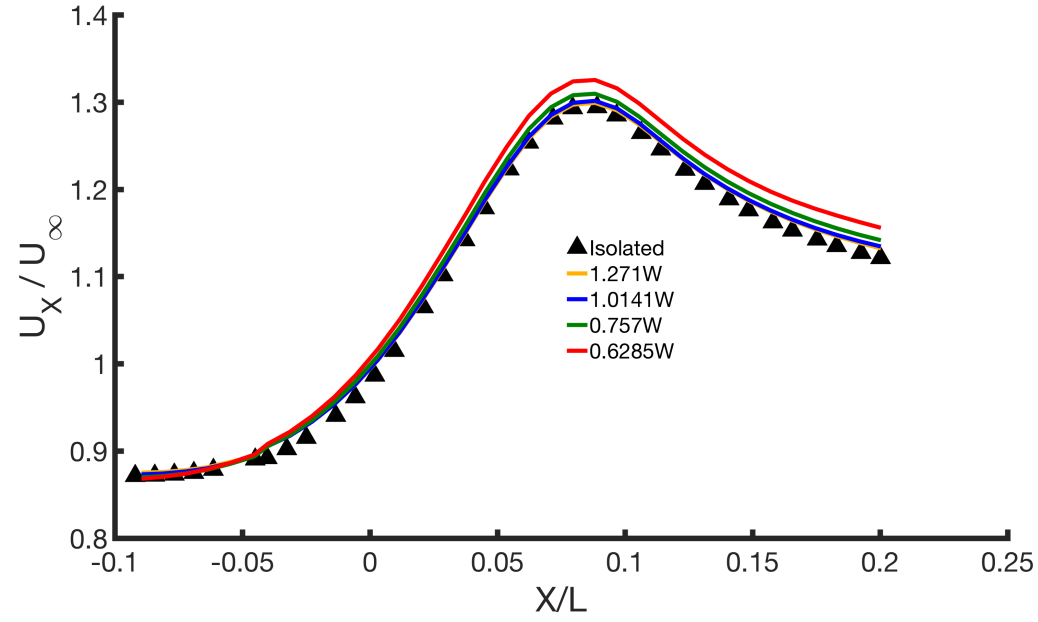

(a)

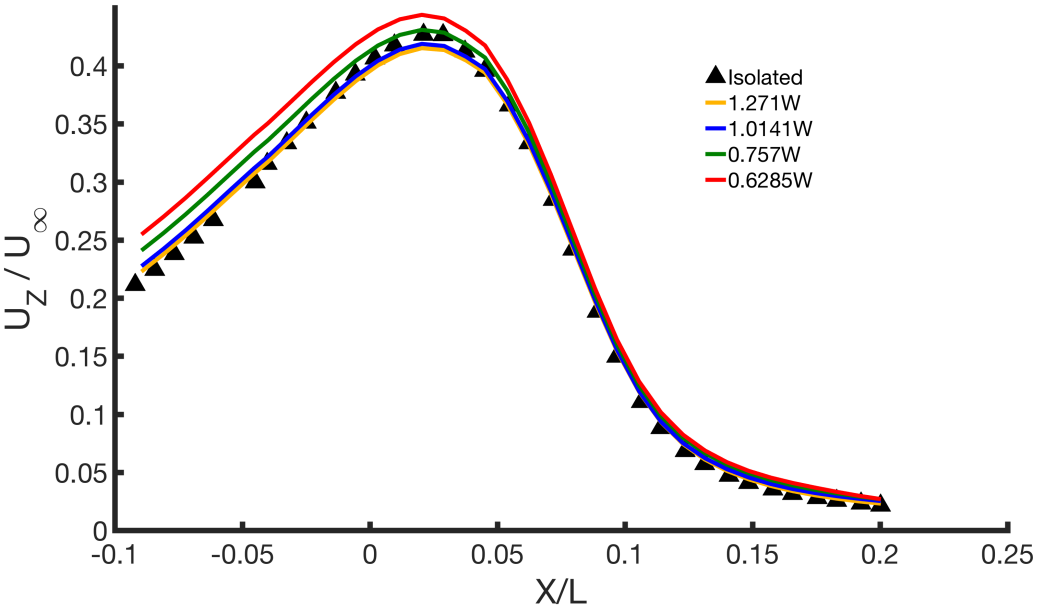

(b)

Figure 4.19: Normalized Velocity Profiles of each Wall Separation cases from CFD data, $Z/L = 0.3021, Y/L = 0$ probe location, are compared with Isolated Case a) Normalized Streamwise Velocity $(U(x)/U_\infty)$ profile b) Normalized Vertical Velocity $(U(z)/U_\infty)$ profile

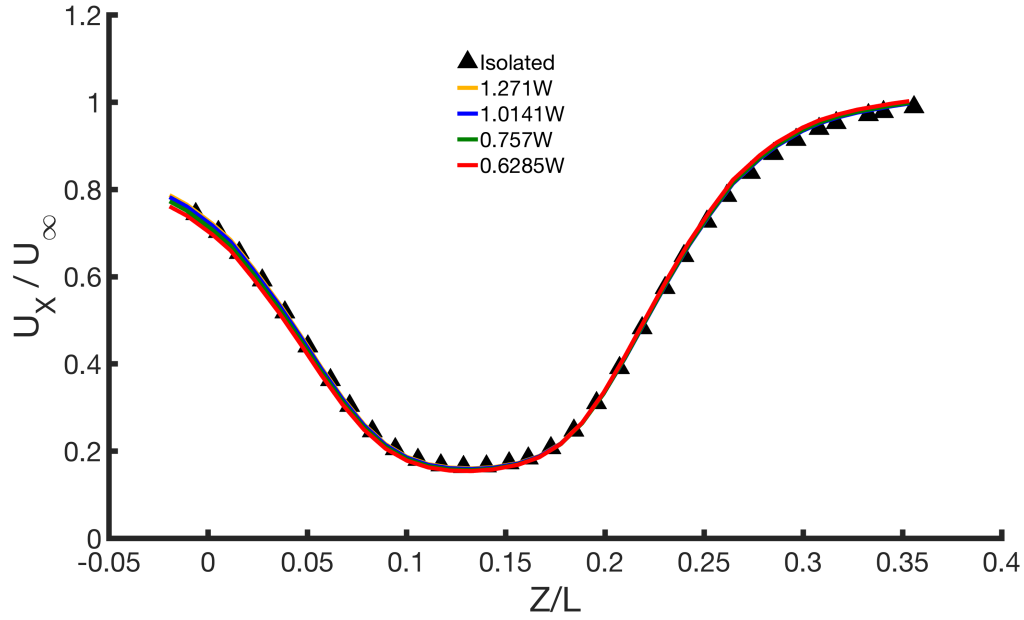

(a)

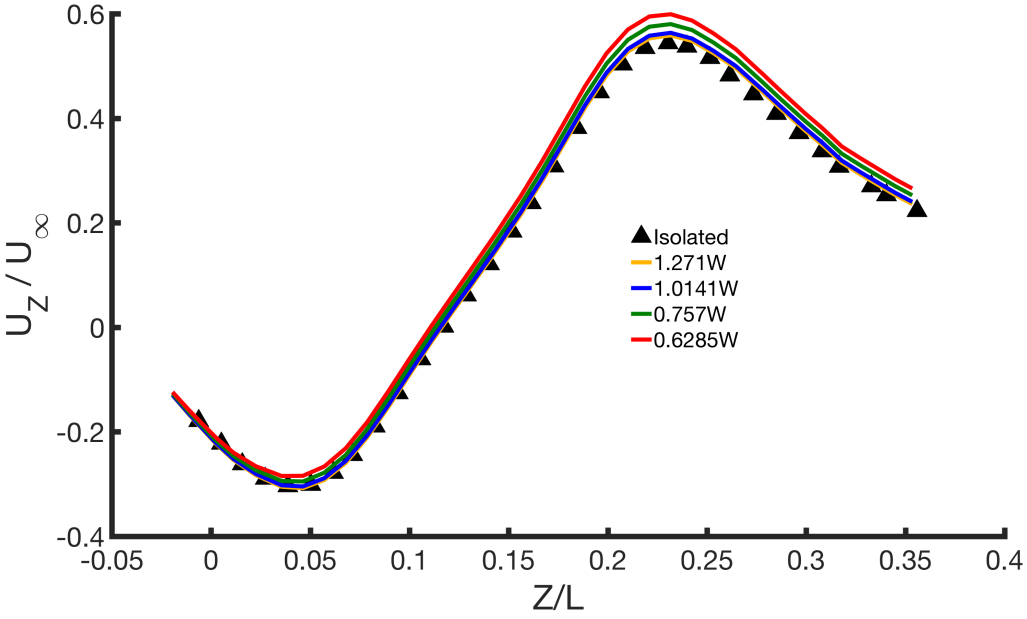

(b)

Figure 4.20: Normalized Velocity Profiles of each Wall Separation cases from CFD data, $X/L = -0.02, Y/L = 0$ probe location, are compared with Isolated Case a) Normalized Streamwise Velocity $(U(x)/U_\infty)$ profile b) Normalized Vertical Velocity $(U(z)/U_\infty)$ profile

The velocity profiles obtained in each wall separation case of the Ahmed body were compared with the isolated case. Figure 4.19(a) depicts the normalized streamwise velocity profiles at $Z/L = 0.3021$. These plots are used to understand the flow behavior over the Ahmed body at the front face. The plots are validated against the isolated case which was already validated with the experimental results. Figure 4.19(b) depicts a similar approach of understanding the flow with the normalized vertical profile but the magnitudes show a difference till the $X/L = -0.05$ probe point and beyond that the difference in the vertical velocities reduce. In contrast, the streamwise velocity differences between each wall separation case shows a significant rise in the magnitude beyond the $X/L = -0.05$ probe point.It is understood that the flow infront of the moving body experiences a considerable in change in vertical velocities with the change in wall separation distances, but the streamwise velocities show no difference. Moreover, the flow over the body experiences considerable rise in streamwise velocities with decreasing wall separation distance and the difference in vertical velocities decrease with the decreasing wall separation distance.

Figures 4.20(a) and 4.20(b) are the velocity profiles for a vertical line probe in front of the body. These plots suggest that the flow in the streamwise direction is lowest at the center and highest at the edges of the face. As a result, the pressure is highest at the center and lowest at the ends of the face. A similar observation is made from vertical velocity profile from Figure 4.20(b), but the flow is highest at the upper end of the Ahmed body (positive end of Z/L value) and lowest at the lower end of the face. This is due to the flow direction along the face is mostly towards the positive Z/L value. Each case shows that the velocities are increasing with decreasing wall separation distance.

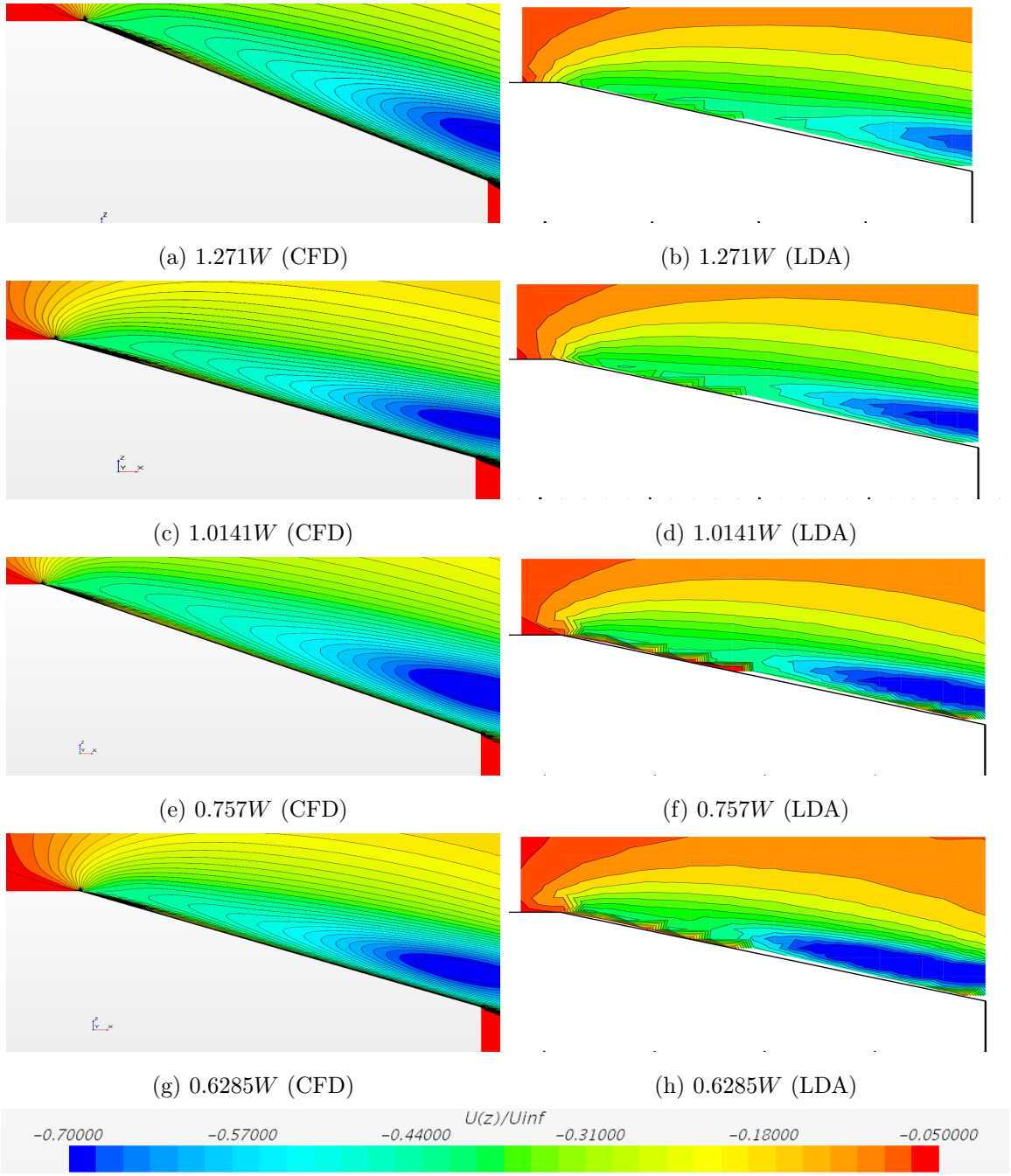

(a) 1.271W (CFD)

(b) 1.271W (LDA)

(c) 1.0141W (CFD)

(d) 1.0141W (LDA)

(e) 0.757W (CFD)

(f) 0.757W (LDA)

(g) 0.6285W (CFD)

(h) 0.6285W (LDA)

Figure 4.21: Normalized Vertical Velocity $U(Z)/U_\infty$ Contour Plots from CFD data, $Y/L = -0.14$ plane location, are compared with Strachan's LDA Data a) c) e) g) SST cases, b) d) f) h) Strachan's LDA Experiment

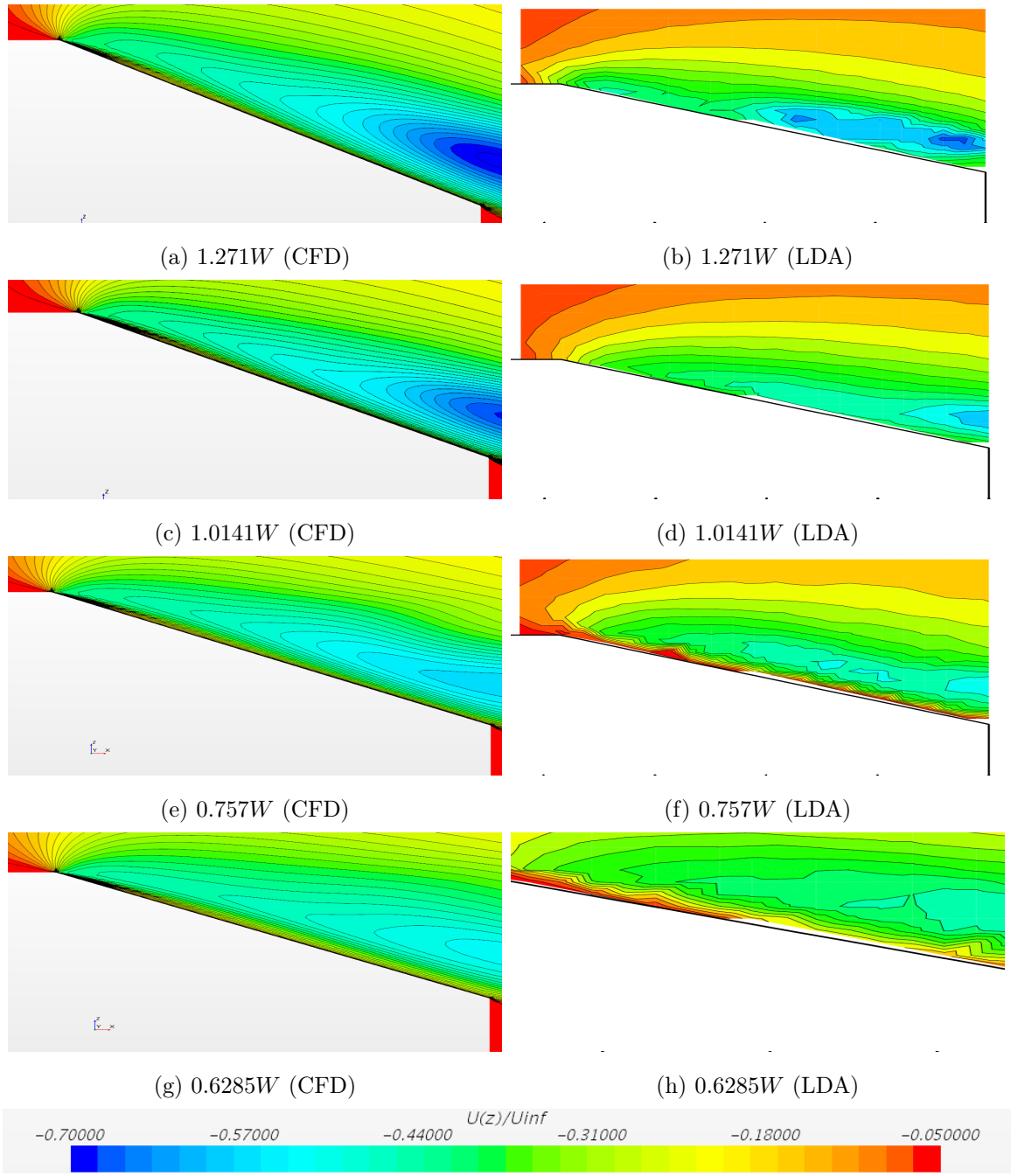

(a) 1.271W (CFD)

(b) 1.271W (LDA)

(c) 1.0141W (CFD)

(d) 1.0141W (LDA)

(e) 0.757W (CFD)

(f) 0.757W (LDA)

(g) 0.6285W (CFD)

(h) 0.6285W (LDA)

Figure 4.22: Normalized Vertical Velocity $U(Z)/U_\infty$ Contour Plots from CFD data, $Y/L = 0.14$ plane location, are compared with Strachan's LDA Data a) c) e) g) SST cases, b) d) f) h) Strachan's LDA Experiment

The flow over the slant angle is an important aspect to consider as the vortex development is identified and the effect of side wall over vortices is clearly understood. Figures 4.21 to 4.22 are the normalized vertical velocity contour plots where each CFD case is compared with the experimental data. Every case shows a decent match with the experimental results. Further analysis of these plots shows a difference between the vortices developed from the edges of the body onto the slant angle. The $1.271W$ case show a minuscule change in the vortex position when the vortex on the near side location ($Y/L = 0.14$) is compared with the vortex on the far side location ($Y/L = -0.14$). As we scroll through the contour plots, the vortex over the slant angle at the near wall side ($Y/L = 0.14$) loses its strength and the vortex location is shifted down towards the wake. The vortex formation is being delayed and carried over by the side wall during the body movement. The downwash of the wake and the vortices for the wall separation cases are longer than the downwash of isolated Ahmed body case. This effect is observed by investigating the trailing edge vortices.

Figure 4.23 describes the normalized vertical velocity contour plots which evidently show that the vortex strength is diminished as the wall separation distance is reduced. The Far side of the vortex contains the same vorticity magnitude for every case unlike

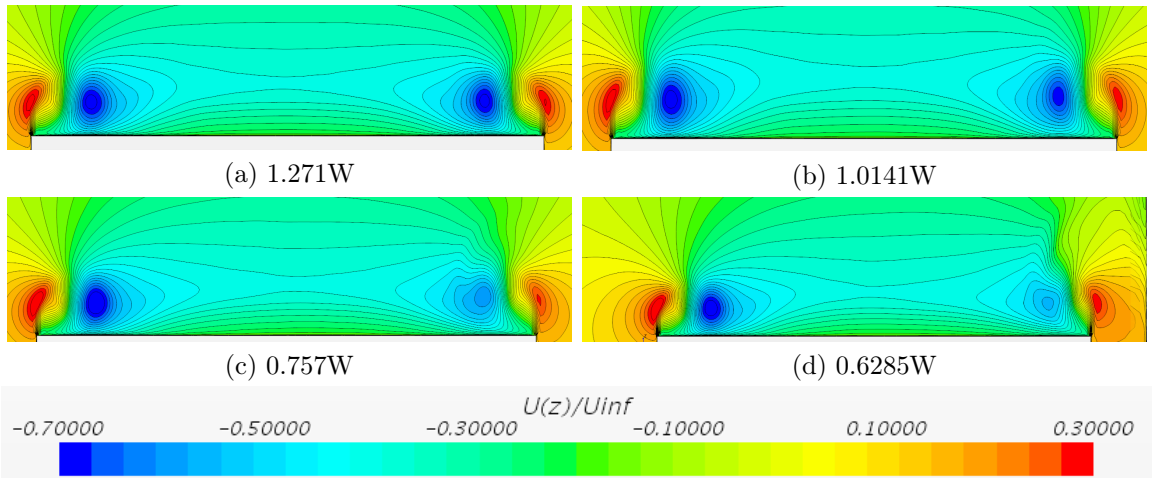

Figure 4.23: Normalized Vertical Velocity $U(Z)/U_\infty$ Profiles from CFD data, $X/L = 1$(above$Z/L = 0.2$) plane location

the vortex on the near wall side. The far side vortex tends to move to the center line of the body where the near side vortex center tends to move up with an increase in distance from the initial position. This phenomenon is a result of suction of the fluid at the frontal region which increases the magnitude of the velocity at the final end of the body. The weaker vortex on the near wall side creates a weaker downwash when compared with the off side vortex generated downwash. These vortex anomalies create a considerable disturbance in the wake which results in irregular force and moment values which are discussed further in the thesis. Figure 4.24 describes the velocity vector direction of the flow with the line integral convolution plots. As discussed previously, the wake of the body predicted by the CFD model shows a change in the vortex centers when compared with the experimental. The point of discussion is to show the variation in the four near wall cases through their wakes and hence the CFD results are used to show the difference between the $1.271W$ case and $0.6285W$ case. The vortex centers in the figures are represented by blue outlined squares. From Figures 4.24(a) and 4.24(b), it is understood that the vortex centers were displaced with the reduction of wall separation. The upper vortex is pushed more upward in the wake for $0.6285W$ case when compared with $1.271W$ case. Similarly, the lower vortex center is displaced closer to the body creating a strong wake. From this, it is understood that the drag of the vehicle is subjected to change and an increase is suspected. However, Strachan's[18] experimental results of the wake showed a similar trend of displacement in the vortex centers but the structure of the vortices in the wake are noticeably different when compared with the present CFD work. This shows that the wake refinement in the CFD model will yield better results.

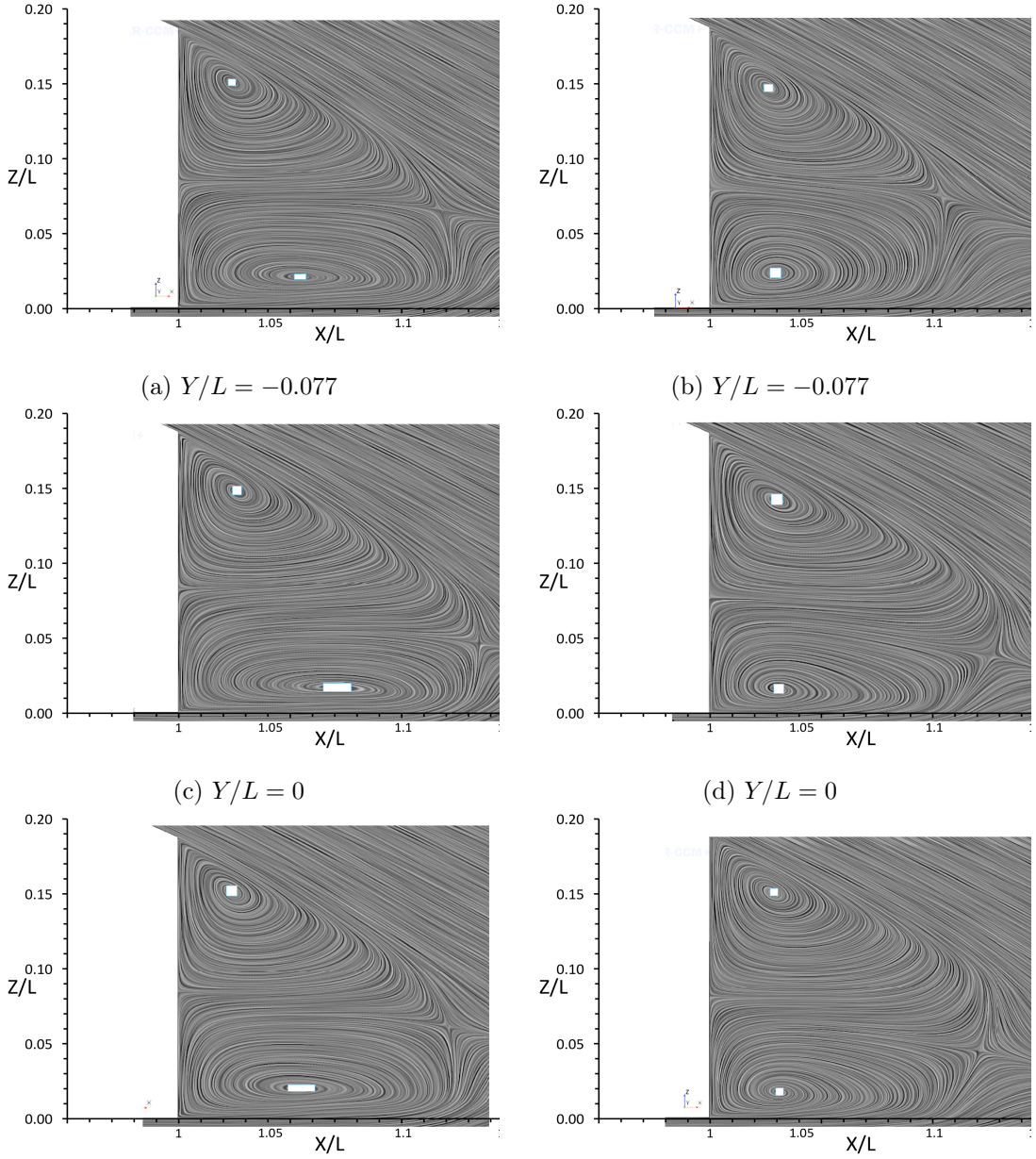

(a) $Y/L = -0.077$

(b) $Y/L = -0.077$

(c) $Y/L = 0$

(d) $Y/L = 0$

(e) $Y/L = 0.077$

(f) $Y/L = 0.077$

Figure 4.24: Comparision of Line Integral Convolution Plots of Velocity Magnitude for a), c), e) 1.271W and b), d), f) 0.6285W Wall Separation Cases

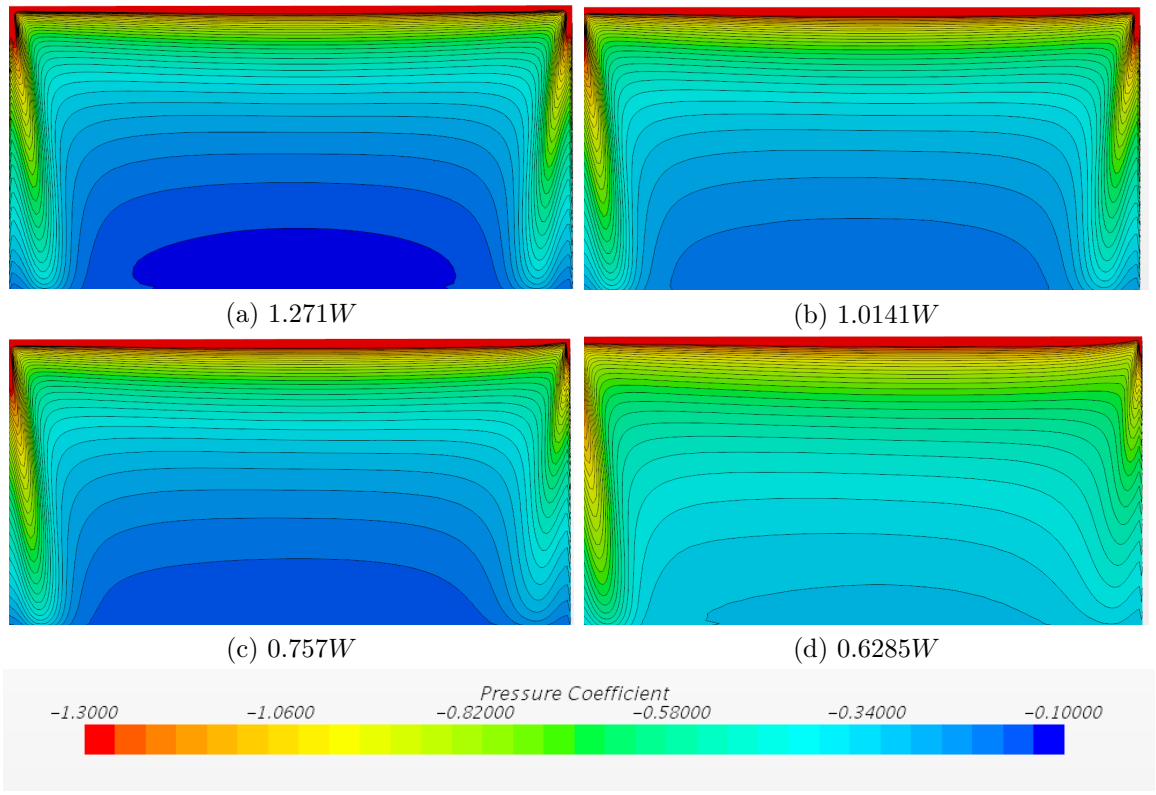

(a) 1.271W (b) 1.0141W

(c) 0.757W (d) 0.6285W

Figure 4.25: C_{P} Contour Plots of Backlight Area from all Wall Separation Cases

From Figure 4.25, the Pressure coefficient Contour plots clearly distinguish the decrease of pressure from case to case. For 0.6285W case, it is explicitly understood that the vortex emerging from the rear slant upper edge is weaker than the vortex emerging from the far side. Higher extent of the pressure difference between two regions cause stronger vortices and this is once again proved with the 0.6285W side wall case. The aerodynamic coefficients will also vary with the change in pressure coefficient on the rear slant that was occurred with the wall separation.

Considering the change in force coefficients and Moment Coefficients with respective to wall separation cases gives an insight of repercussion of the pressure, velocity and vorticity changes of the flow around it. These changes are worth mentioning to have a valid evidence of the analysis that was previously made. Figure 4.26, is a comparison plot between the CFD predicted values and Strachan's[18] Experimental Values. The change in lift shows a great similarity with the experimental results and

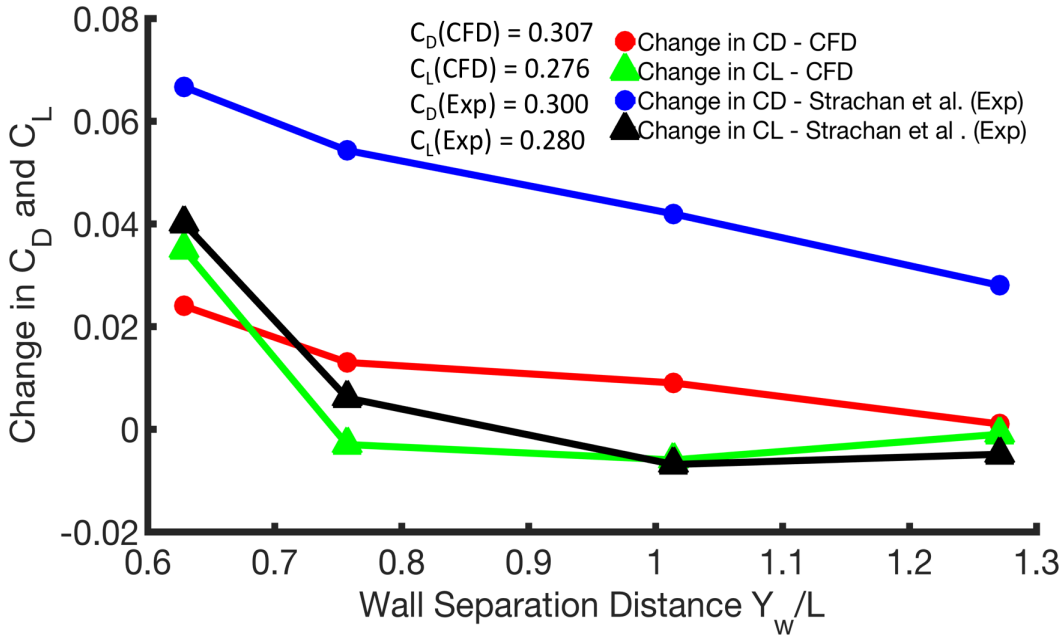

Figure 4.26: Change in C_{D} and C_{L} with Wall separation (Y_{W}/L) Plot

the change in C_{D} follows a similar trend as the experimental values. The difference in the values is of fixed magnitude and it is observed in all force and moment coefficients. This offset in the values of drag are observed because of the difference in emulating the flow in experiment and CFD. The air flow in the experiment creates a boundary layer over the side wall and the body which makes the flow accelerated through the gap, but the flow in CFD simulations is stationary which evades the creation of boundary layer on the side wall and so the air experiences lesser magnitude of acceleration than it experiences in the experiment. However, the flow phenomenon underneath the body in both experiment and CFD simulations is similar and this similarity showed an accuracy in the prediction of lift values by the CFD simulations. Considering the realistic situation, the procedure used in the CFD is more accurate than the procedure used in the experiments. Hence the offset in the force and moments predicted by CFD are acceptable. Moreover, the CFD model predicted the initial values of drag and lift very accurately than the CFD model used by Strachan in his thesis. Looking into the pattern of the plots, the drag is increasing with a decrease in wall separation

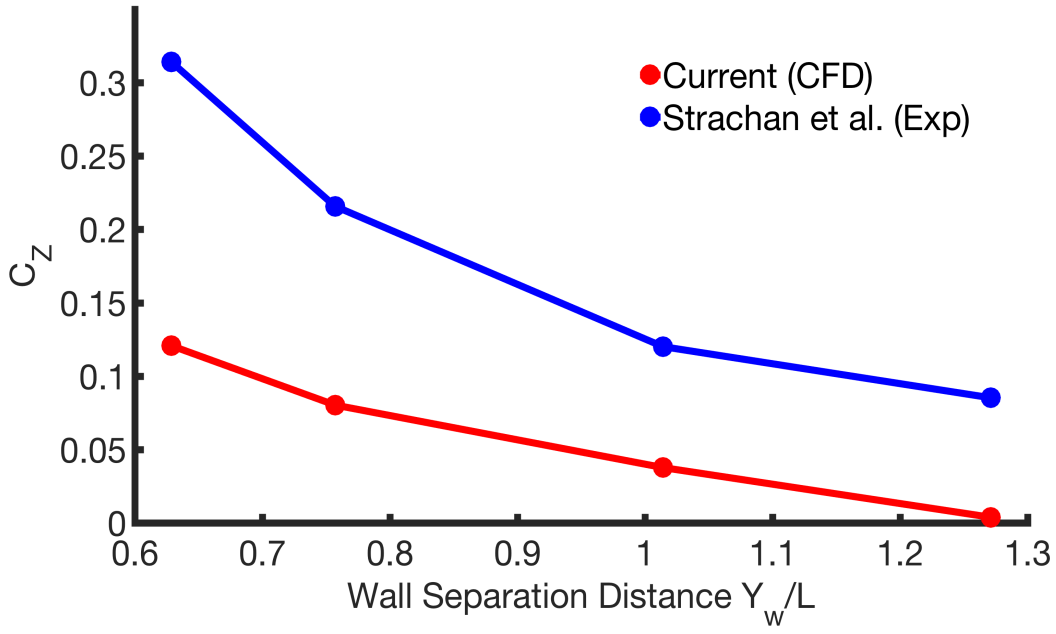

Figure 4.27: Change in Side Force Coefficient C_Z versus Wall Separation (Y_W/L) Plot

distance. This is observed in the lift but the lift predicted by the CFD which is in good agreement with Strachan's experiment has an exponential growth at $0.6285W$ yielding 12.8% of increase. The lift values predicted a drop at $1.0141W$ case which is due to the increase of suction at the front end. Nevertheless, the increased suction over the top of the model dominates the flow in further cases resulting in a gain of lift.

Figure 4.27, shows a similar trend of Strachan's experimental results of the change in side force coefficient but the predicted values were below the experimental values. However, this same trend was observed in the drag values as mentioned previously. On observing the plots of side force, it shows an increase of side force at minimum wall separation distance and this forces acts on the body which results in a strong pushing force away from the side wall.The velocity between the body and the wall is maximum which is evident from the plots and contours. As a result, the pressure between the two surfaces drops creating a suction effect on the face of the body. The

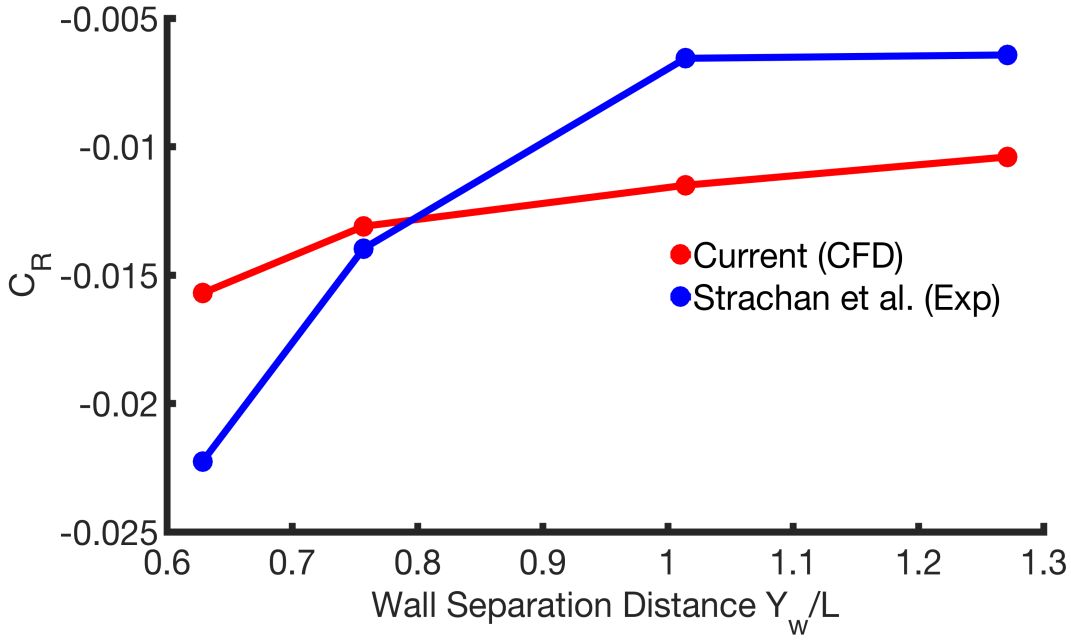

Figure 4.28: Rolling Moment Coefficient C_{Z} versus Wall Separation (Y_{W}/L) Plot

side force acting on the body towards the negative Y axis on the face drastically decreases due to low pressure on the face near to the wall. But, the velocity towards the rear end of the body decreases leading to an increase in pressure on the body which inturn increases the side force acting on the body towards the negative Y axis. This whole scenario increases the side force acting on the body pushing the body away from the side wall. This induces rolling and yawing moments which are plotted in Figures 4.27 and 4.28 respectively.

Figure 4.28, depicts the rolling moment coefficient in the negative values. The negative values suggest that the body is experiencing the rolling moment away from the wall. The trend of the plot predicted by the CFD is similar to the experimental values but the slope of the curve changed only for the $0.6285W$ case. The rolling moment which is induced by the suction effect generates lift in the body with decreasing wall separation distance. The values of rolling moment coefficient are deviated by 10% from the experimental results which is acceptable.

Figure 4.29, shows the variation of yaw moment in the body. Yawing in the body is

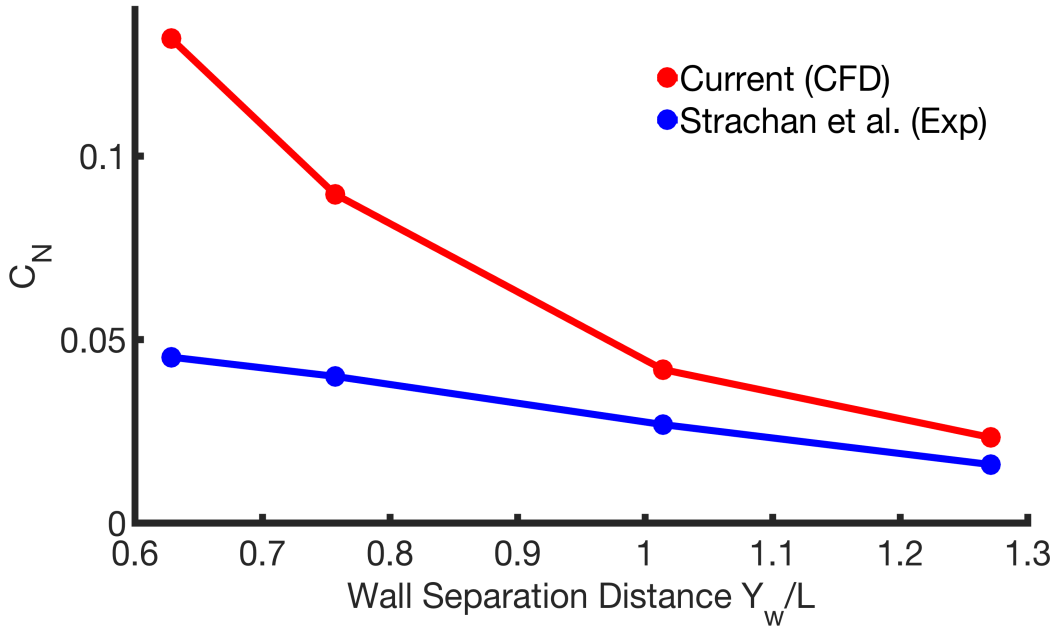

Figure 4.29: Yawing Moment Coefficient C_Z versus Wall Separation (Y_W/L) Plot

purely obtained from the suction and it increases with a decrease in the wall separation distance. The yawing moment coefficient predicted by the CFD simulations shows a trend similar to the experimental results but the slope of the curve formed with CFD predictions is not similar to the experimental curve. However, this change in the CFD predicted values from the experimental values was mentioned previously with a procedural difference explanation. Nevertheless, the CFD predictions still show the rise in the yaw moment with decreasing wall separation distance.

Figure 4.30, the pitching moment is found to increase at every wall separation case but CFD predictions were not projecting a steep curve as the experimental results do. However, the values predicted by the CFD model were consistent and there was roughly 8% increase in every case. The changes of Pitching Moment coefficient are plotted in Figure 4.30 shows that there is a steady rise in the pitching of the body. The increase of lift directly projects the increase of pitching in the body. This is validated with the velocity profile plots, where the flow is higher at the top of the model leading to a pressure drop. The high pressure under the body induces lift and pitching in the

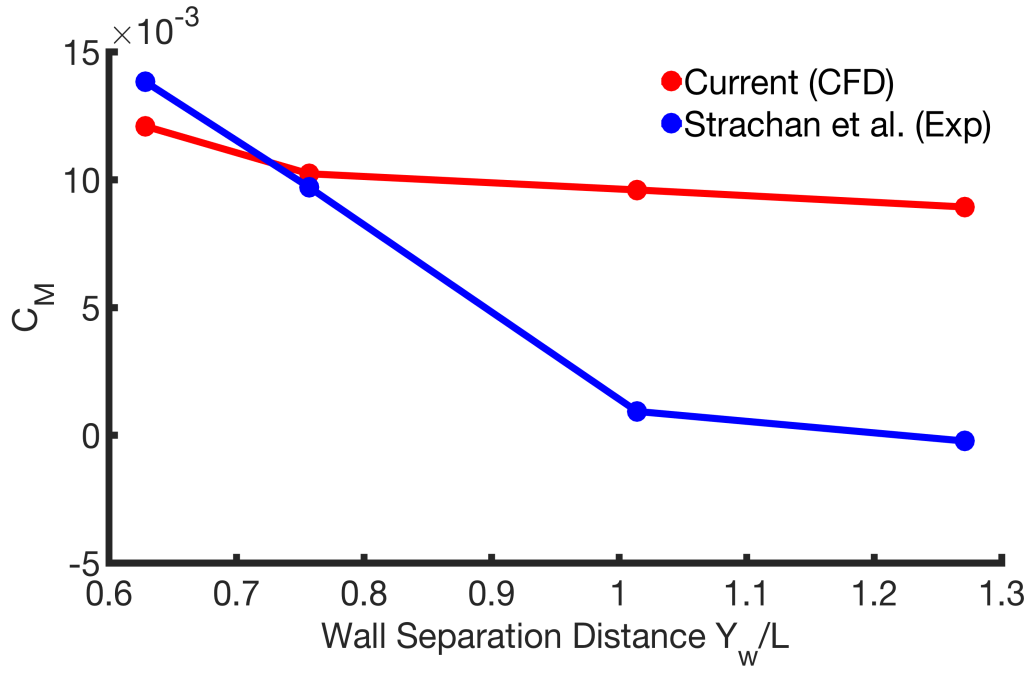

Figure 4.30: Pitching Moment Coefficient C_{M} versus Wall Separation (Y_{W}/L) Plot

body. The values predicted by the CFD follow the trend of the experimental results and the difference in the values is acceptable with the afore mentioned argument. A well-refined mesh between the body and side wall might improve the results and the time step is one more key factor for better results.

Apart from the force coefficients and the moment coefficients, another interesting aspect is found while investigating the vortices that were formed around the body. The suction induced pressure drop between the body and side wall aided the lower longitudinal vortex to slide to the upper edge of the Ahmed body resulting a rolling moment on the body and abnormal lift. This finding is given the high priority for the peculiar behavior of the fluid vortex along the vertical height of the body on the near wall side and it was less discussed in the literature. The evolution of these vortices may not be detected if the Ahmed body contains stilts or an over-hanging strut while experimentation. Figure 4.31 shows the difference between each normalized streamwise velocity contour plot and it clearly conveys the development of vortices with the direction of rotation. On glancing the contour plots, the lower longitudinal

vortex in the $1.271W$ case was forced to slide along the boundary layer of the fluid on the body to reach the top most point and it is evidently understood that decrease of wall separation distance increases the flow velocity in the separation gap. As the flow velocity in the gap increases, the longitudinal vortex emerging from the face of the body is displaced towards the top edge of the body and strong recirculation region is formed due to high pressure difference on the near wall side of the body and the top surface of the body. This vortex is shifted only towards the upper edge of the body because the vertical flow velocity shown in Figure 4.32(d) is high in the gap along with high streamwise flow velocity shown in Figure 4.31(d). The vortex is forced to move up due to this flow phenomenon. The vortex developed at the top edge contains strong recirculation zone created by a huge pressure difference between the near wall side surface of the body and the top surface of the body. Furthermore, the pressure difference created between the surfaces was due to the high velocity flow in the gap. The velocity profiles on the vortex development places were plotted for every case of wall separation for quantifying results in validating the above argument.

Figure 4.32 shows a lucid representation of the strength of the vortex that is developed on the upper edge of the body on the near wall side. The flow in the gap is explicitly represented as high velocity flow that is driving the vortex from the lower edge to the upper edge. This scenario is never stated before and few authors suggested that the pressure is extremely low at the lower edge but couldn't identify the displacement of the vortex. This is assumed as the primary reason for an increase in the rolling moment and lift on the body along with an increase in drag. The velocity profiles at these locations validate my analysis and further research can be done on identifying the causes and advantages of this wall induced vortex displacement.

Figure 4.33 shows the variation of the vortices about the transverse line at $Z/L = 0.2985$ and $Z/L = 0.00862$ respectively. These evidently show the vortex recirculation on the top edge and vortex degradation on the lower edge of the body. The strength

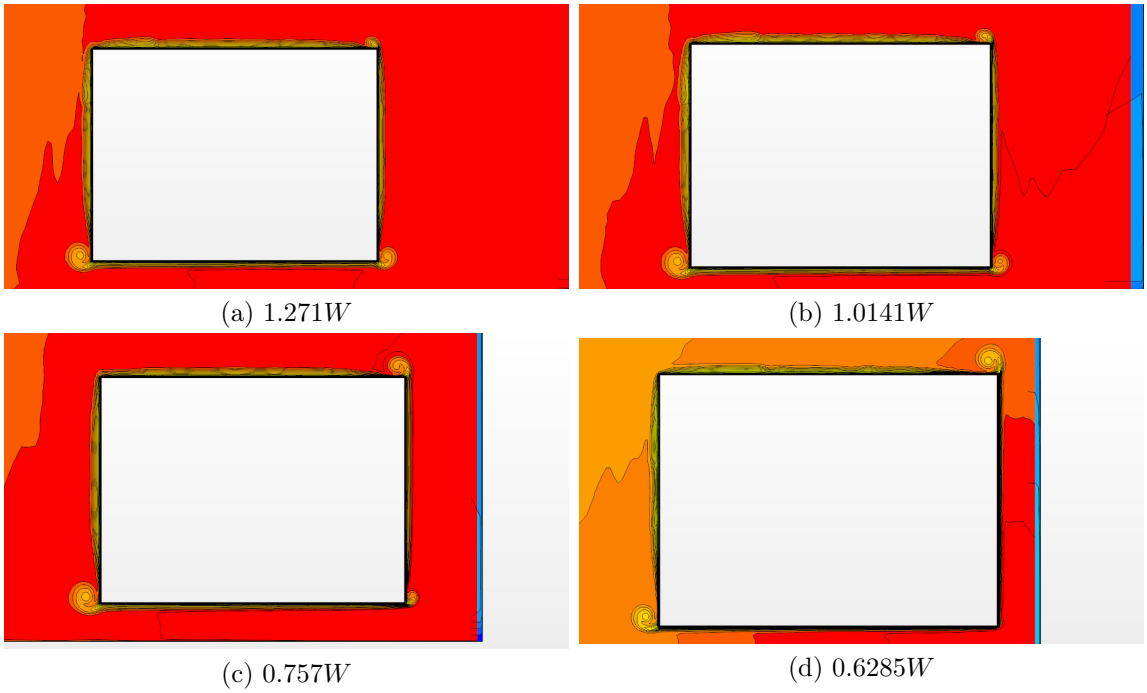

(a) 1.271W

(b) 1.0141W

(c) 0.757W

(d) 0.6285W

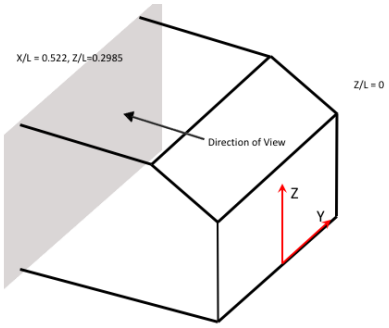

(e) Schematic Location of the Contour Plots

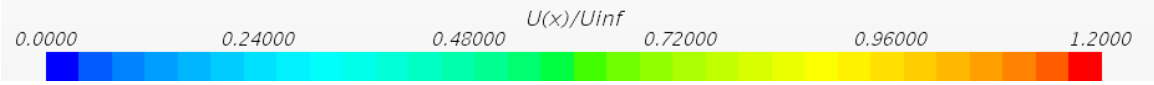

Figure 4.31: Normalized Streamwise Velocity ($U(x)/U_\infty$) Contour Plots of Center Plane at $X/L = 0.5$ from all Wall Separation Cases

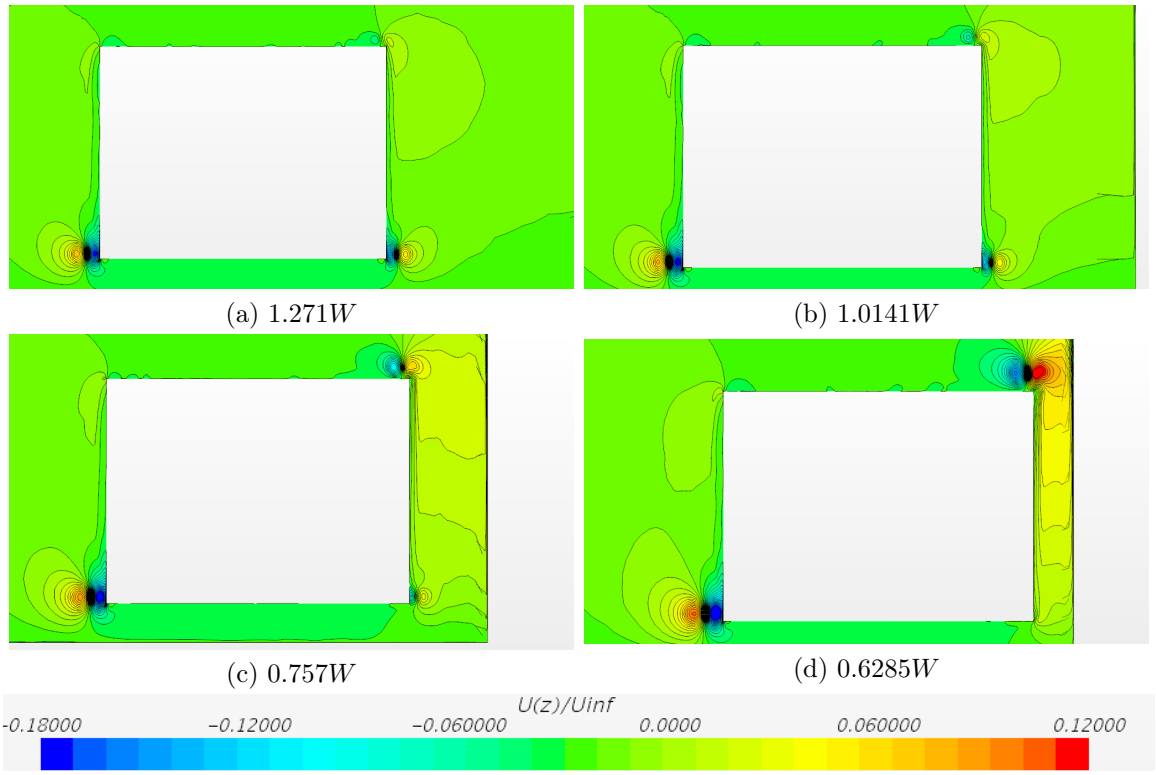

(a) 1.271W (b) 1.0141W

(c) 0.757W (d) 0.6285W

Figure 4.32: Normalized Vertical Velocity $U(z)/U_\infty$ Contour Plots of Center Plane at $X/L = 0.5$ from all Wall Separation Cases

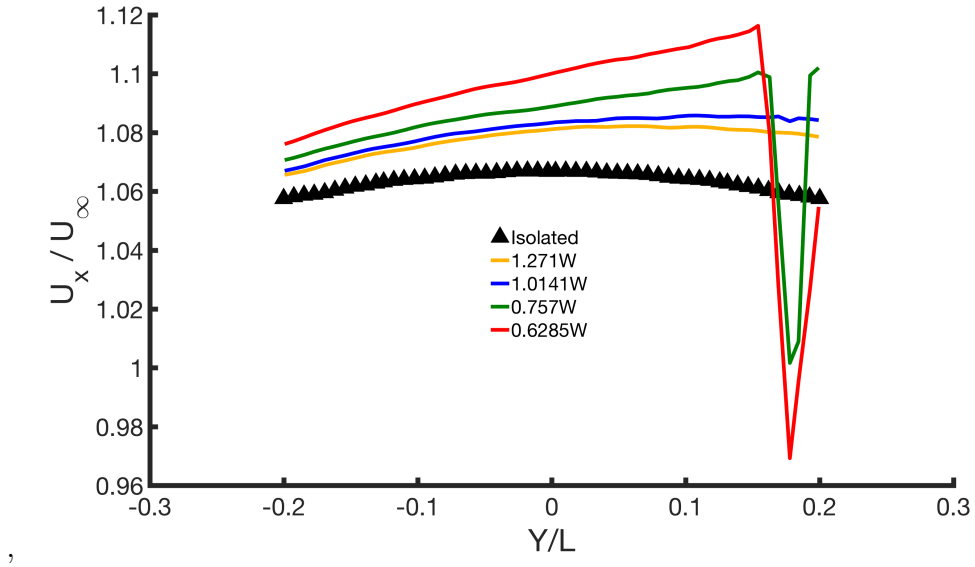

(a)

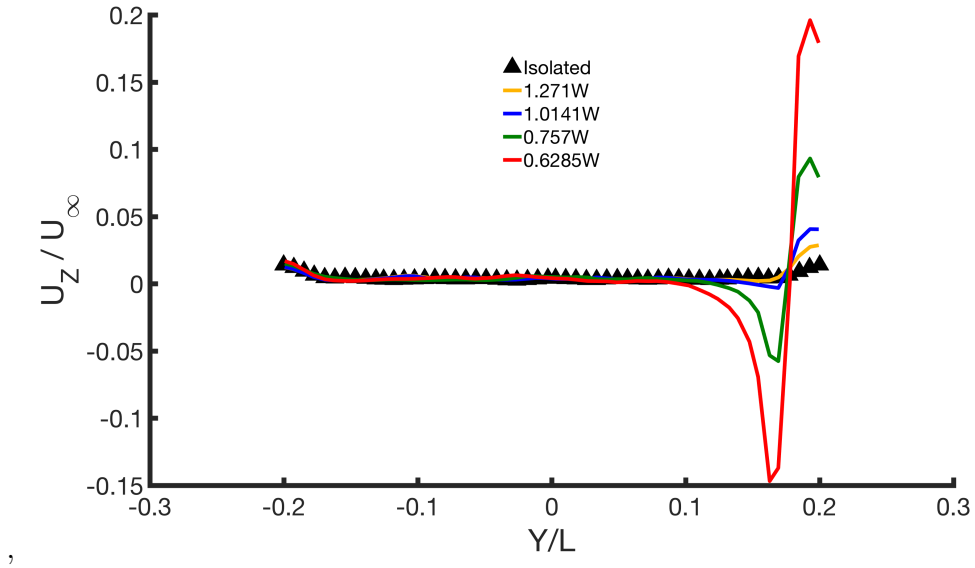

(b)

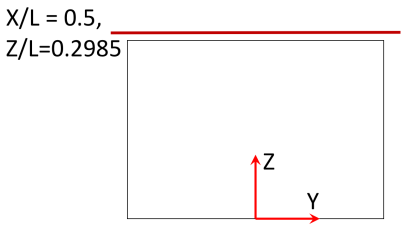

(c)

Figure 4.33: Normalized Velocity Profiles from all Wall Separation Cases, $X/L = 0.5, Z/L = 0.2985$ probe location, are compared with Isolated Case a) Normalized Streamwise Velocity $(U(x)/U_\infty)$ profile b) Normalized Vertical Velocity $(U(z)/U_\infty)$ profile c) Schematic of Line Probe

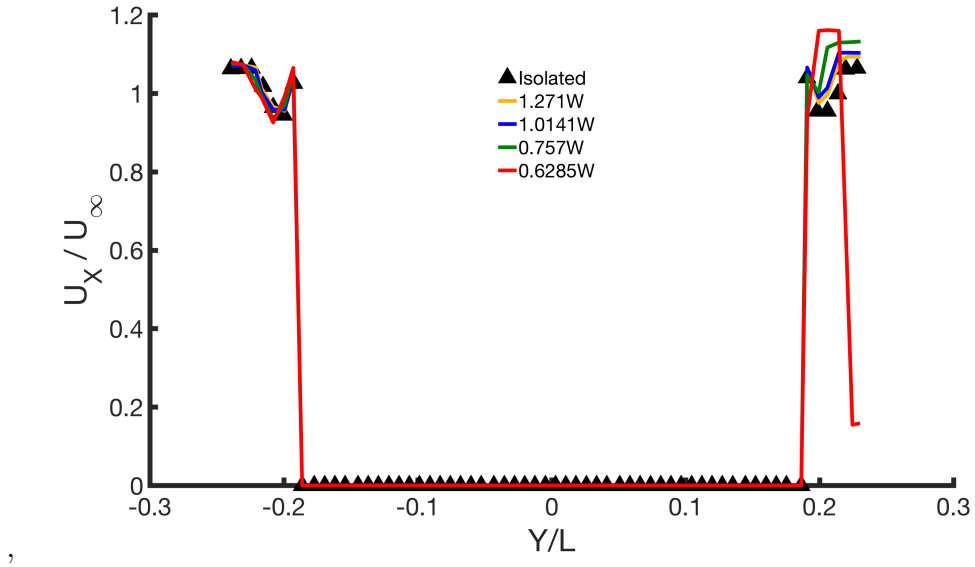

,

(a)

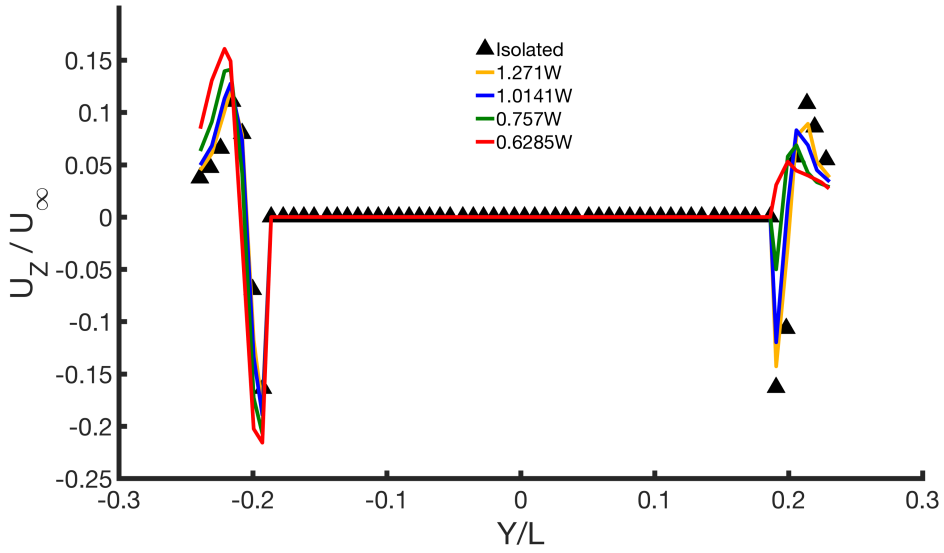

,

(b)

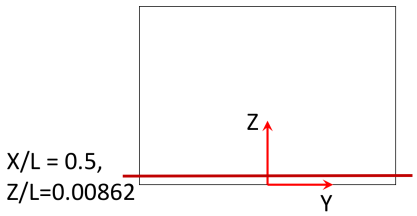

(c)

Figure 4.34: Normalized Velocity Profiles from all Wall Separation Cases, $X/L = 0.5, Z/L = 0.00862$ probe location, are compared with Isolated Case a) Normalized Streamwise Velocity $(U(x)/U_\infty)$ profile b) Normalized Vertical Velocity $(U(z)/U_\infty)$ profile c) Schematic of Line Probe

of the vortex on the upper edge near to wall is lower than the strength of the lower vortex which is on the off side. This shows that the rolling moment caused by the upper vortex is slightly opposed by the lower vortex which is rotating in alternate direction with respective to the direction of rotation of the top edge vortex. This moment is included with the yaw moment caused by suction. One more interesting observation is that the streamwise velocity of the vortex is higher than the vertical velocity causing an elongation of the vortex longitudinally towards the rear slant. In comparison with these plots, the vertical velocity profiles are added to supplement the foundation for the argument. Figure 4.34 shows the exact process of the vortex shifting and this is the substantial effect of the suction process that is experienced by the frontal part of the body. However, the impact of this vortex development on the wake and the trailing edge vortex is not known which is to be considered for further research.

CHAPTER 5: CONCLUSIONS

The simulations that were conducted over the isolated Ahmed body case tested the abilities and the capabilities of the two turbulence models in predicting the appropriate results. The Original SST turbulence model was inaccurate in predicting the flow field over the rear slant of the Ahmed body during the course of CFD testing. However, this problem was resolved by replacing the Schmidt number constants in the formulation of the original SST model while considering the study done by Bredberg[25]. This modified SST model yielded a C_{D} value of 0.307 and C_{L} value of 0.276 which are consistent with the results of previous experiments. The severity of the 25° slant angle model is that the flow pattern over the rear slant is separated at the top edge and reattached down the surface. Both the turbulence models couldn't predict the exact flow pattern, but the modified SST model was able to predict the flow without the flow separation at the mentioned position. The flow field in front and underneath the Ahmed body was predicted by both the turbulence models with the same level of accuracy. The flow over the body was accurately predicted by the SST model, but the AKN model over predicted the recirculation bubble causing a discrepancy in the magnitude of the velocity of the flow. Considering the significant flow field in the wake of the body, the SST model was able to predict the wake and the downwash of the trailing edge vortices accurately than the AKN model. However, the AKN model was more successful in accurately predicting the magnitudes of the velocities in the vortex regions over the body. The flow over the rear slant predicted by the SST model was consistent with the experimental result than the flow prediction of the AKN model. Although the prediction of the vortex development over the slant angle was slightly inaccurate by both the turbulence models, the strength of the

trailing edge vortices and the stretching of vortices along the transverse direction were accurately predicted by the SST model over the AKN and Strachan's CFD model. The extent of pressure distribution over the rear slant area was well predicted by the SST model than the AKN, but the SST model showed an extremely low pressure on the top edge of the rear slant which is not seen in the experimental results. Furthermore, the modification of original SST model suppressed the turbulent kinetic energy and turbulent mixing of the fluid in the flow field which limited the capability of the model in predicting weaker recirculating zones and under predicting the magnitudes of the velocities in strong recirculation zones. In comprehending the above results, this thesis concluded that the modified SST model is suitable for this Ahmed body in predicting the required results with very few discrepancies. However, the mesh errors between the Overset interface and the background region in StarCCM+ hinders the solver to attain accuracy in the solution. These discrepancies must be evaded in the future to have a better solution.

The Near wall study revealed the fact that the flow which enters the gap between the body and the side wall is subjected to have a rise in velocity leading to a pressure drop and in turn creates a suction effect. This argument is supported by the comparisons made between each wall separation case to the isolated case in the velocity profiles. The flow over the wake represented by the contour plots shows the delayed development of the vortex over the rear slant near to the side wall of each wall separation case. The contour plots of the trailing edge vortices show a decrease in strength of the near wall side vortex in every wall separation case showing the effect of the wall on the flow over the body. The recirculating vortices in the wake of the body were displaced from the initial position moving closer to the body and the size of the wake was reduced for the $0.6285W$ wall separation case. The aerodynamic forces and moments were significantly changed and worsened with the decreasing wall separation distance. The effect of the offset of the values in the force and moment

results predicted by CFD when compared with the experimental values is attributed to the difference in the process of emulating the flow in CFD and the experimental studies. However, the drag force is subjected to increase through out the process, but the lift reduces at first and later increases with wall separation. Furthermore, the body experiences an asymptotic rise in the lift as it moves closer to the wall. This phenomenon is explained by the finding of a vortex development on the upper edge of the body near to the side wall that was shifted from the lower edge due to the flow velocity between the surfaces and the pressure difference between the near wall side surface of the body and the top surface of the body. This aspect should be considered for further investigation to recognize the true impact of it on the body and on the wake.

Optimization of the model constants in the turbulence model formulation to predict the weaker the recirculation zones will enhance these simulations and refinement of mesh over the rear slant with a structured grid shall reduce the inaccuracy of velocity magnitudes in recirculation zones. This investigation is to be considered as a decent approach yielding results which are in good agreement with the experimental results. Based on the setup and the technique used in this thesis, a further research on wall proximity studies including various realistic motions should be performed to analyze the eccentricity projected in the force and moment results beyond a specific wall separation distance.

5.1 Future Research

While there is an enormous availability of latest complex geometries and generic car models, this thesis can be utilized to investigate a real life situation using CFD simulation. This thesis opens a door to reckon about conducting an experimental procedure with moving ground and moving side wall which are in close proximity to the vehicle body for more realistic approach. The CFD results in this thesis can be validated based on those experimental results. Furthermore, research in investigating

the model moving at a yaw angle along a curved wall will be more advantageous in racing point of view. Using a DrivAer or a NASCAR model and performing a full car simulation around a race track will yield extraordinary findings which will be of great interest to the racing industry. Some research on the modified SST model, that was used in this thesis can be tested with various slant angle models of Ahmed body inorder to understand the capabilities and limitations of the turbulence model. The flow over an Ahmed body in proximity to a side wall is analyzed in this thesis, but it is to be understood that the flow beyond the vehicle affects the tandem vehicles. This phenomenon is an interesting area where researchers can have deep insight into the problem and investigate the after effects of a fully disturbed turbulent flow over a tandem vehicle. Nevertheless, reckoning to simulate most complex issue on CFD is the ultimate aim of this thesis.

REFERENCES

[1] S. Ahmed, G. Ramm, and G. Faltin, "Some salient features of the time-averaged ground vehicle wake," in *SAE Technical Paper*, SAE International, 02 1984.

[2] B. F. Zhang, S. To, and Y. Zhou, *Strouhal Numbers of Unsteady Flow Structures Around a Simplified Car Model*, pp. 179–184. Berlin, Heidelberg: Springer Berlin Heidelberg, 2014.

[3] J. Graysmith, A. Baxendale, J. Howell, and T. Haynes, "Comparisons between cfd and experimental results for the ahmed reference model," 1994.

[4] H. Lienhart and S. Becker, "Lda measurements of the flow and turbulence structures in the wake of a simplified car model," *Institute of Fluid Mechanics (LSTM) University Erlangen-Nuremberg*, 2000.

[5] H. Lienhart, C. Stoots, and S. Becker, *Flow and Turbulence Structures in the Wake of a Simplified Car Model (Ahmed Modell)*, pp. 323–330. Berlin, Heidelberg: Springer Berlin Heidelberg, 2002.

[6] H. Lienhart and S. Becker, "Flow and turbulence structure in the wake of a simplified car model," in *SAE Technical Paper*, SAE International, 03 2003.

[7] I. Bayraktar, D. Landman, and O. Baysal, "Experimental and computational investigation of ahmed body for ground vehicle aerodynamics," 11 2001.

[8] R. Strachan, K. Knowles, and N. Lawson, "The vortex structure behind an ahmed reference model in the presence of a moving ground plane," *Experiments in fluids*, vol. 42, no. 5, pp. 659–669, 2007.

[9] S. Krajnovic and L. Davidson, *Flow Around a Simplified Car, Part 1: Large Eddy Simulation*, pp. 127(5):907–918. Berlin, Heidelberg: ASME. J. Fluids Eng, 2005.

[10] M. Minguez, R. Pasquetti, and E. Serre, "High-order large-eddy simulation of flow over the "ahmed body" car model," *Physics of fluids*, vol. 20, no. 9, p. 095101, 2008.

[11] S. Kapadia, S. Roy, M. Vallero, K. Wurtzler, and J. Forsythe, "Detached-eddy simulation over a reference ahmed car model," *ERCOFTAC SERIES*, vol. 9, pp. 481–488, 2004.

[12] E. Serre, M. Minguez, R. Pasquetti, E. Guilmineau, G. B. Deng, M. Kornhaas, M. Schafer, J.Frohlich, C. Hinterberger, and W. Rodi, "On simulating the turbulent flow around the ahmed body: A french-german collaborative evaluation of les and des," *Computers & Fluids*, vol. 78, pp. 10 – 23, 2013. LES of turbulence aeroacoustics and combustion.

[13] E. Guilmineau, "Computational study of flow around a simplified car body," *Journal of Wind Engineering and Industrial Aerodynamics*, vol. 96, no. 6, pp. 1207 – 1217, 2008. 5th International Colloquium on Bluff Body Aerodynamics and Applications.

[14] S. Wallis and W. Quinlan, "A discussion of aerodynamic interference effects between a race car and a race track retaining wall (a wind tunnel nascar case study)," tech. rep., SAE Technical Paper, 1988.

[15] J. Brown, *Racecar Aerodynamics In Close Proximity To A Retaining Wall*. MSc Aerospace Dynamics Individual Thesis, Cranfield University, Cranfield, Bedfordshire, UK, 2005.

[16] Advantage CFD, "A CFD NASCAR case study into the effects of wall proximity," June 2001.

[17] R. Strachan, R. Knowles, and N. Lawson, "Comparisons between cfd and experimental results for a simplified car model in wall proximity," in *2nd international symposium on integrating CFD and experiments in aerodynamics*, 2005.

[18] R. K. Strachan, *The Aerodynamic Interference Effects of Side Wall Proximity on a Generic Car Model*. PhD Defense College of Management, Technology Department of Aerospace, Power and Sensors Individual Thesis, Cranfield University, Cranfield, Bedfordshire, UK, 2005.

[19] H. Hadzic *et al.*, *Development and application of finite volume method for the computation of flows around moving bodies on unstructured, overlapping grids*. PhD thesis, Technische Universität Hamburg, 2006.

[20] StarCCM+ User Manual.

[21] H. Tennekes and J. L. Lumley, *A first course in turbulence*. MIT press, 1972.

[22] C. Argyropoulos and N. Markatos, "Recent advances on the numerical modelling of turbulent flows," *Applied Mathematical Modelling*, vol. 39, no. 2, pp. 693–732, 2015.

[23] F. R. Menter *et al.*, "Two-equation eddy-viscosity turbulence models for engineering applications," *AIAA journal*, vol. 32, no. 8, pp. 1598–1605, 1994.

[24] A. Hellsten, "Jim aa," 1998.

[25] J. Bredberg, S.-H. Peng, and L. Davidson, "An improved $k-\omega$ turbulence model applied to recirculating flows," *International Journal of Heat and Fluid Flow*, vol. 23, no. 6, pp. 731 – 743, 2002.

[26] D. C. Wilcox *et al.*, *Turbulence modeling for CFD*, vol. 2. DCW industries La Canada, CA, 1998.

[27] B. E. Launder and D. B. Spalding, "The numerical computation of turbulent flows," *Computer methods in applied mechanics and engineering*, vol. 3, no. 2, pp. 269–289, 1974.

[28] F. R. Menter, R. B. Langtry, S. Likki, Y. Suzen, P. Huang, and S. Völker, "A correlation-based transition model using local variables - part i: model formulation," *Journal of turbomachinery*, vol. 128, no. 3, pp. 413–422, 2006.

[29] K. Suluksna, P. Dechaumphai, and E. Juntasaro, "Correlations for modeling transitional boundary layers under influences of freestream turbulence and pressure gradient," *International Journal of Heat and Fluid Flow*, vol. 30, no. 1, pp. 66–75, 2009.

[30] P. Malan, K. Suluksna, and E. Juntasaro, "Calibrating the γ-reθ transition model for commercial cfd," in *47th AIAA aerospace sciences meeting*, pp. 5–8, 2009.

[31] K. Abe, T. Kondoh, and Y. Nagano, "A new turbulence model for predicting fluid flow and heat transfer in separating and reattaching flows-i. flow field calculations," *International journal of heat and mass transfer*, vol. 37, no. 1, pp. 139–151, 1994.

[32] Y. Nagano, M. Tagawa, and M. Niimi, "An improvement of the k-e turbulence model (the limiting behavior of wall and free turbulence, and the effect of adverse pressure gradient)," *Trans. Jpn. Soc. Mech. Eng. B*, vol. 55, no. 512, pp. 1008–1015, 1989.

[33] M. Tagawa, "An improved k-e model for boundary layer flows," *Journal of fluids engineering*, vol. 112, p. 33, 1990.

[34] A. Singh, S. Kumar, and K. Nikam, "High performance cfd computations for ground vehicle aerodynamics," in *SAE Technical Paper*, The Automotive Research Association of India, 01 2011.

[35] N. Ashton and A. Revell, "Key factors in the use of ddes for the flow around a simplified car," *International Journal of Heat and Fluid Flow*, vol. 54, pp. 236–249, 8 2015.

[36] E. Guilmineau, G. Deng, A. Leroyer, P. Queutey, M. Visonneau, and J. Wackers, "Assessment of hybrid rans-les formulations for flow simulation around the ahmed body," 01 2017.